The generation of upstream-propagating waves in astrophysically-relevant laboratory plasmas

Robert Harvey Crowston

Doctor of Philosophy

University of York

Physics

September 2015

Abstract

The primary focus in this thesis is on the production and detection of upstream-propagating waves in laser-laboratory plasmas. Upstream waves are a feature of shocks in plasmas; launched at or just ahead of the shock, they travel against the flow into the unshocked medium. Despite the importance of upstream waves in understanding the properties of the Earth's bow shock, and the foreshock region just ahead of the shock, upstream waves have not previously been investigated in the laboratory. The laboratory shock waves are produced by laser-matter interaction, and allowed to propagate into a nitrogen atmosphere, immersed in a magnetic field. One-dimensional numerical simulations of the fluid enable the construction of the whistler dispersion function; a mode unstable to growth is identified. The mode is compared with observations taken by a magnetic field probe, understood by a wavelet analysis. Agreement between observation and prediction is found.

TABLE OF CONTENTS

List of figures

List of tables

Acknowledgements

I am indebted to many people for their support, advice and in some cases, labour, during this project. I thank Yasu Kuramitsu, Youichi Sakawa, and Taichi Morita for making me feel most welcome during the time I spent in Japan, for giving me the time to try my ideas during their facility time, and for repeatedly inviting me back. I thank Rob Clarke, Rob Heathcote, and Margaret Notley at the Rutherford Appleton Laboratory, who have all offered invaluable technical advice and made doing experiments at the Vulcan facility (often) quite enjoyable. I am grateful to João Jorge Santos and Mathieu Bailly-Grandvaux for discussions on interpreting and filtering bdot data, as well as the invitation to join them on their experiment at the LULI facility in 2014. I also thank Richard Armitage and Neil Johnson for their assistance in building our experiments in the laboratory in York, and for their invaluable advice in the mechanical design of some of my experiments (and for sneaking me to the front of the engineering work queue).

At the University of Oxford I thank Gianluca Gregori and Jena Meinecke, who made their bdot probes and their experience in using them available to me; and I also wish to acknowledge Tony Bell for valuable insight and discussion.

In particular I must express my gratitude to Chris Murphy, Alex Pelka and Hugo Doyle, who have all taught me much and more about the practicalities of conducting laser plasma experiments, and to whom I each owe many a drink. I thank Joseph Cross for assisting me in obtaining essential articles from the many journals to which the University of York does not deign to subscribe, and for providing me with distraction precisely when it was most required.

Finally, and most importantly, I thank Nigel Woolsey, who has guided and supported me through this work; he has allowed me to explore my ideas and has always been available with useful and insightful counsel.

Declaration of the Author

I, Robert Harvey Crowston, declare that this thesis is a presentation of original work and that I am the sole author. This work has not previously been presented for an award at this, or any other, University. All sources are acknowledged as references.

The experiments discussed in this thesis were necessarily conducted by many people at laser laboratories. The author's contribution to these has been as an experimentalist, assisting in the running of the experiments and collecting the data therefrom. The experiment discussed in Part 5.2 (the 2014 GEKKO experiment) was conceived and designed by the author.

All data analysis presented herein has been undertaken by the author, as have the computer simulations and the numerical calculations of the whistler dispersion function.

1. INTRODUCTION

1.1. MOTIVATION

'Plasma' is a Greek word (*πλάσμα*) originally meaning "something which is easily moulded or shaped" (Liddell & Scott, 1890), the same root that gives us 'plastic' and (less directly) 'plaster'. Therefore the choice of this word *plasma* to describe the fourth state of matter seems immediately an etymological irony. Not only do all but the tamest of manmade plasmas often resist being moulded, but moreover their ripe complexity makes their behaviour hard to predict and understand.

Laboratory astrophysics can be divided into studies of 'input parameters', such as equations of states and nuclear cross sections, and scaled experiments of astrophysical systems (Remington *et al.*, 2000). I am looking at the latter case in this thesis. Much of the physics underpinning the behaviour of astrophysical systems is scale-invariant: it is possible to design laboratory studies of astrophysical phenomena that access the same physics, or pieces thereof, even though the systems are starkly different in scale (Cross *et al.*, 2014; Ryutov *et al.*, 2000).

Space plasmas (those occurring in our solar system) have not enjoyed the attention of laboratory experiments that high-energy astrophysical plasmas have. Yet understanding the interaction between the solar wind and the bow shock is an open problem that may be particularly fertile for the kind of interchange offered by a combined observational, numerical and experimental approach. Moreover, kinetic processes in the foreshock region, lying directly ahead of the bow shock, mediate the effects of space weather on the Earth's magnetic field. As it has become apparent that our satellite infrastructure could be vulnerable to extreme space weather events, understanding these kinetic

processes in the foreshock is a priority (Collier *et al.*, 2010; Kangas *et al.*, 2001; Posner *et al.*, 2004).

1.2. THE CONTEXT OF LASER LABORATORY ASTROPHYSICS

Modern, high energy density facilities now enable matter to be studied in high-energy states believed to be relevant to many astrophysical environments. Laboratory experiments do not replace observations or computer simulations, but rather complement them. An approach incorporating experiments offers some advantages over an investigation made with only computers or telescopes. Unlike observations, experiments are repeatable, reproducible, and with clearly defined start and end states. Experimental configurations can be easily quantified and varied. Multiple diagnostics, including active diagnostics, can probe the properties of the experiment from many angles. The wider array of diagnostic capabilities means that some information can be directly obtained, and not merely inferred from other measurements. However, there are always physics components that cannot be scaled; equations of state and viscosity terms, for instance.

Numerical simulations need to be validated against work in the laboratory: in particular, the range of spatial and temporal scales that can be accessed is often limited; for instance, codes might be able to simulate either a small part of a system accurately, or the full system without full regard for the microphysics processes, but not the fully detailed physics at all levels in the three dimensions. For a more detailed review of laboratory astrophysics, see for instance Remington *et al.* (2000).

1.3. UPSTREAM WAVES IN THE EARTH'S BOW SHOCK

The Earth has a surface geomagnetic field of approximately 4×10^5 nT, which is much larger than the typical magnetic field embedded in the solar wind at the Earth's orbital radius (about 10 nT). Bearing in mind Alfvén's theorem, the Earth's magnetosphere therefore presents a substantial blunt obstacle to the solar wind flow; and the interaction

of the supersonic flow and the obstacle produces a standing shock wave in front of the Earth known as the *bow shock*.

Upstream waves are waves that are travelling upstream from a shock. Such a wave cannot occur except in plasmas, because in most systems a shock is by definition the fastest wave that propagates: the situation in plasmas is different because of the plethora of wave modes supported. Moreover, when shocks are mediated by long-range collective effects instead of short-range collisions, the interplay between waves and particles becomes still more complex. Such is the plurality of wave modes possible in front of the Earth's bow shock that some authors have called the region a 'zoo' of different wave species (Burgess, 1997).

Understanding this region is difficult because, with *in situ* probes, the spatial scales of the shock and the waves are much larger than the measuring instruments aboard the probe. Numerical simulations have difficulty working over the large scale and with the multiplicity of kinetic and fluid effects.

Recently a number of experiments particularly in the laser laboratory have enabled the scaling of systems to approach in well-defined ways the physical parameters present in astrophysical systems, for instance by Gregori *et al.* (2012) and Meinecke *et al.* (2014) who studied the creation of proto-galactic magnetic fields under the Biermann battery effect, and the subsequent amplification of those fields through turbulence. Some very recent work has demonstrated the possibility of exciting whistler waves in the laboratory through injection of an electron beam into a prepared plasma environment (Van Compernolle *et al.*, 2015). However to the present author's knowledge no one has previously measured shock-excited upstream waves in the laboratory.

1.4. CHAPTER OUTLINE

In Chapter 2 I review the theoretical topics necessary for the basis of the experiment. First I look at the underpinnings of rigorous scaling from laboratory to space, including in non-ideal systems (where dissipative effects are present). Then I look at the generation of shock waves; and indeed at the standing bow shock about the Earth. Finally I discuss a process by which a drifting, warm electron population may excite upstream waves.

Chapter 3 deals with instruments relevant to my experimental work. Whenever a physical quantity is measured by an instrument it is important to have a grasp of the capabilities of the measuring device: essentially one desires to know how far the data that the instrument provides may be accorded belief. More formally, it is necessary to have some understanding of the response function of the instrument. In Chapter 3 therefore I discuss the design and capabilities of three instruments; the bdot probe, the Nomarski interferometer, and the electron spectrometer. Further, I look at how far what might be termed the 'raw data' they supply may be interpreted to give physical measurements—and what assumptions that interpretation entails.

I introduce some important signal analysis techniques in the fourth Chapter. The data collected in my experiments is, to some degree at least, contaminated by noise and therefore some relatively robust signal analysis techniques are used to isolate features of interest. To put the analysis of experimental data on a surer footing I review those methods in Chapter 4.

In Chapter 0, I discuss four experiments. Two are studies intended to create and detect upstream waves in the laser laboratory through the creation of a shock front in a prepared environment. Another experiment concerns the production of pulsed magnetic fields; I use it to gain a measure of understanding of the response function of the bdot probe. Finally I look at the characterization of hot electrons arising from a laser-matter interaction.

In Chapter 1, I draw together the results obtained through the experiments to test my hypothesis that upstream waves are created in the laboratory. I find that the experimental bdot data that I obtain are in agreement, in terms of frequency and time-of-flight arrival at the bdot probe, with the numerical estimation.

2. THEORY

In this Chapter I give a review of some topics relevant to the experimental work I later present, with a focus on the theoretical underpinnings that enable experiments in laser laboratories to be meaningfully compared to situations in astrophysics and in space physics. I also discuss how whistler waves can be spontaneously excited in plasmas under certain conditions, by adapting a mechanism proposed by Gary (1985).

2.1. ASTROPHYSICS IN THE LABORATORY

2.1.1. The Euler–Alfvén scaling relation.

Cross *et al.* (2014) went so far as to describe the scaling of the magnetohydrodynamic ('MHD') equations in the presence the quantum, resistive and radiative effects. However, I shall look first at MHD scaling in the ideal (that is, non-dissipative) case. This was first described by Connor and Taylor (1977), and first applied to astrophysical systems by Ryutov (2000).

The ideal MHD equations may be expressed (Boyd & Sanderson, 2003)

$$\frac{\partial \rho}{\partial t} + \boldsymbol{\nabla} \cdot \rho \mathbf{v} = 0, \tag{2.1}$$

$$\rho \left(\frac{\partial \mathbf{v}}{\partial t} + \mathbf{v} \cdot \boldsymbol{\nabla} \mathbf{v} \right) = -\boldsymbol{\nabla} p - \frac{1}{4\pi} \mathbf{B} \wedge \boldsymbol{\nabla} \wedge \mathbf{B}, \text{ and} \tag{2.2}$$

$$\frac{\partial \mathbf{B}}{\partial t} = \boldsymbol{\nabla} \wedge (\mathbf{v} \wedge \mathbf{B}), \tag{2.3}$$

in the centimetre-gram-second system of units. The symbols have their usual meanings. Further we close the system with

$$\frac{\partial p}{\partial t} + \mathbf{v} \cdot \boldsymbol{\nabla} p = -\gamma p \boldsymbol{\nabla} \cdot \mathbf{v}, \tag{2.4}$$

for adiabatic index γ (the ratio of specific heats). For this description to be accurate, it is assumed that the plasma be—

$$\begin{aligned} \text{collisional:} \quad & \tau_{ii} \ll \sqrt{\frac{m_e}{m_i}}\tau_H,\ \lambda_{ii} \ll \lambda_H, \\ \text{non-relativistic:} \quad & \frac{\omega}{k} \sim \frac{L_H}{\tau_H} \sim u \ll c, \\ \text{quasi-neutral:} \quad & \frac{\omega|\omega_{ce}|}{\omega_{pe}^2} \ll 1, \\ \text{with small Larmor radii:} \quad & \frac{r_{L_e}}{\lambda_H} \ll \sqrt{\beta}. \end{aligned} \tag{2.5}$$

In the above and elsewhere in this chapter, τ_{ii} is the ion collision time and λ_{ii} is the ion collisional scale length; m_e and m_i are the masses of electrons and ions respectively; τ_H is the characteristic hydrodynamic time and λ_H is the hydrodynamic scale length; ω and k are the angular frequency and wave number of waves in the system; ω_{ce} is the electron gyrofrequency and ω_{pe} is the electron plasma frequency; and r_{L_e} is the electron Larmor radius.

By a variable change it is straightforward to re-write the system of equations (2.1)–(2.4) in a non-dimensional form; that is,

$$\rho = \rho^*\rho_0,\ \ t = t^*t_0,\ \ \mathbf{v} = \mathbf{v}^*v_0,\ \ \mathbf{B} = \mathbf{B}^*B_0,\ \ p = p^*p_0,\ \ \boldsymbol{\nabla} = \frac{1}{x_0}\boldsymbol{\nabla}^*, \tag{2.6}$$

where in each case the symbols with asterisks are dimensionless parameters and the zero-subscripted quantities hold the physical dimensions. For instance one obtains, for (2.1),

$$\frac{\partial(\rho^*\rho_0)}{\partial(t^*t_0)} + \frac{1}{x_0}\boldsymbol{\nabla}^* \cdot \{(\rho^*\rho_0)(\mathbf{v}^*v_0)\} = 0. \tag{2.7}$$

Now, by judicious choice of the dimensional quantities we may eliminate the presence of dimensions from (2.1)–(2.4) altogether, while retaining the form of the equations. For instance on making the substitutions

$$t_0 \to \sqrt{\frac{\rho_0}{p_0}}x_0,\ \ v_0 \to \sqrt{\frac{p_0}{\rho_0}},\ \ \text{and}\ \ B_0 \to \sqrt{p_0}, \tag{2.8}$$

one obtains, for (2.1),

$$\frac{\rho_0}{x_0\sqrt{\frac{\rho_0}{p_0}}} \times \frac{\partial\rho^*}{\partial t^*} + \frac{\rho_0\sqrt{\frac{p_0}{\rho_0}}}{x_0}\boldsymbol{\nabla}^* \cdot \rho^*\mathbf{v}^* = 0, \tag{2.9}$$

which immediately may be reduced to

$$\frac{\partial \rho^*}{\partial t^*} + \boldsymbol{\nabla}^* \cdot \rho^* \mathbf{v}^* = 0. \tag{2.10}$$

But for the asterisks (which merely indicate the quantity lacks physical dimensions), (2.10) is essentially (2.1). A similar transformation, preserving the form of the equations but stripping their dimensions, occurs in (2.2)–(2.4).

It will be observed that although t_0, v_0, and B_0 are fixed by relation to ρ_0, p_0, and x_0, the latter three quantities are free, except we impose the restriction that they must each hold the proper physical dimension to which each appertains: for instance, ρ_0 must be a density. However, the fixed 'number multiplier' or scale component of the quantity is inconsequential in the evolution of the system.

More explicitly, suppose at some particular instant of time, the distribution and motion of plasma in two physically independent systems are geometrically related under the transformations

$$\mathbf{x}_1 = a\mathbf{x}_2,\ p_1 = bp_2,\ \rho_1 = c\rho_2,\ \mathbf{B}_1 = \sqrt{b}\,\mathbf{B}_2,\ \text{and}\ \mathbf{v}_1 = \sqrt{b/c}\,\mathbf{v}_2. \tag{2.11}$$

(2.11) effectively defines a 'shape function' or set of initial conditions between the two distributions. Here, a, b, and c are scalar constants. We further suppose that both systems satisfy the assumptions in (2.5) and therefore each evolve separately according to equations (2.1)–(2.4). The first system (subscripted '1') may be reduced to a non-dimensional form as outlined above: $\mathbf{x}_1 = x_0\mathbf{x}^*$ for some fixed dimensional x_0, and likewise for p_1, ρ_1, $\mathbf{B}_1$, $\mathbf{v}_1$, and t_1. It follows that $\mathbf{x}_2 = (x_0/a)\mathbf{x}^*$, and similarly for the other quantities of the second system: system 2 evolves with a fixed scaling to the first system, with a temporal synchronization satisfying $t_1 = \sqrt{c/b}\ a\ t_2$.

In other words, if at any time the transformation (2.11) exists, then it is valid for all time, provided only that the assumptions (2.5) hold without interruption.

2.1.2. Scaling relations in non-ideal systems.

Plasmas produced both in laboratories and in astrophysical systems often deviate from ideal. To understand how this affects the validity of scaling, I introduce finite viscosity and finite resistance into the MHD equations.

With a term for viscosity the momentum equation (2.2) reads

$$\rho\left(\frac{\partial \mathbf{v}}{\partial t}+\mathbf{v}\cdot\boldsymbol{\nabla}\mathbf{v}\right)=-\boldsymbol{\nabla}p-\frac{1}{4\pi}\mathbf{B}\wedge\boldsymbol{\nabla}\wedge\mathbf{B}+\rho\nu\boldsymbol{\nabla}^2\mathbf{v}. \tag{2.12}$$

ν is the kinematic viscosity. Applying the transformations (2.6) and (2.8) gives

$$\rho^*\left(\frac{\partial \mathbf{v}^*}{\partial t^*}+\mathbf{v}^*\cdot\boldsymbol{\nabla}^*\mathbf{v}^*\right)=-\boldsymbol{\nabla}^*p^*-\frac{1}{4\pi}\mathbf{B}^*\wedge\boldsymbol{\nabla}^*\wedge\mathbf{B}^*+\left(\frac{\nu\sqrt{\rho_0}}{x_0\sqrt{p_0}}\right)\rho^*\boldsymbol{\nabla}^{*2}\mathbf{v}^*$$

$$\rho^*\left(\frac{\partial \mathbf{v}^*}{\partial t^*}+\mathbf{v}^*\cdot\boldsymbol{\nabla}^*\mathbf{v}^*\right)=-\boldsymbol{\nabla}^*p^*-\frac{1}{4\pi}\mathbf{B}^*\wedge\boldsymbol{\nabla}^*\wedge\mathbf{B}^*+\frac{1}{\mathrm{Re}}\rho^*\boldsymbol{\nabla}^{*2}\mathbf{v}^*. \tag{2.13}$$

The quantity $\left(\frac{\nu\sqrt{\rho_0}}{x_0\sqrt{p_0}}\right)$ is better expressed as $\frac{1}{\mathrm{Re}}$ where

$$\mathrm{Re}=\frac{x_0v_0}{\nu}=\left(\frac{x_0\sqrt{p_0}}{\nu\sqrt{\rho_0}}\right) \tag{2.14}$$

is the Reynolds number, a dimensionless measure of the importance of inertial forces to viscous forces (Huba, 2009). Therefore in comparing the evolution of two systems of disparate scales, it is needed that the reciprocals of their Reynolds numbers are in agreement for the scaling to be valid; and moreover, unless the physics underlying the viscosity also scale, it is required that the Reynolds number is large enough in both systems for the viscous forces to be negligible.

Similarly, the induction equation (2.3) may be written with a term for finite resistance. Expressing Ohm's law with a term η for resistivity, we have

$$\mathbf{E}+\frac{1}{c}\mathbf{v}\wedge\mathbf{B}=\eta\mathbf{j}. \tag{2.15}$$

Then the Maxwell–Faraday law is

$$\frac{\partial \mathbf{B}}{\partial t}=\boldsymbol{\nabla}\wedge(\mathbf{v}\wedge\mathbf{B})-\frac{c^2}{4\pi}\boldsymbol{\nabla}\wedge(\eta\boldsymbol{\nabla}\wedge\mathbf{B}). \tag{2.16}$$

Provided η is constant in space,

$$\frac{\partial \mathbf{B}}{\partial t}=\boldsymbol{\nabla}\wedge(\mathbf{v}\wedge\mathbf{B})-D_\eta\boldsymbol{\nabla}^2\mathbf{B} \tag{2.17}$$

for the magnetic diffusivity, $D_\eta=c^2\eta/4\pi$. After the substitutions (2.6) and (2.8),

$$\frac{\partial \mathbf{B}^*}{\partial t^*}=\boldsymbol{\nabla}^*\wedge(\mathbf{v}^*\wedge\mathbf{B}^*)-\left(\frac{D_\eta}{x_0\sqrt{p_0/\rho_0}}\right)\boldsymbol{\nabla}^{*2}\mathbf{B}^*$$

and therefore

$$\frac{\partial \mathbf{B}^*}{\partial t^*}=\boldsymbol{\nabla}^*\wedge(\mathbf{v}^*\wedge\mathbf{B}^*)-\frac{1}{\mathrm{Re_m}}\boldsymbol{\nabla}^{*2}\mathbf{B}^*. \tag{2.18}$$

In this case the quantity remaining is the reciprocal of the magnetic Reynolds number, a quantification of the importance of magnetic advection to magnetic diffusion.

Depending on which non-ideal terms are included in the evolution equations, there are many dimensionless scaling numbers that can be identified to characterize the relationship between two systems.

2.1.3. The Sedov–Taylor law.

In 1941 Sir Geoffrey Taylor was asked by the Civil Defence Research Committee to consider the mechanical effects of releasing a large quantity of energy into a small volume; the energy being released by nuclear fission. The reason the distinction in energy source is important is that, as Taylor found, without the generation of high-pressure gas that accompanies the detonation of chemical explosives, a nuclear detonation is only half as efficient as a blast producer as a chemical device releasing the same energy. Taylor's paper was declassified and released in 1950 (Taylor, 1950), by which time Leonid Sedov of the Soviet Union had independently discovered and published the same derivation, in the Russian language journal Applied Mathematics and Mechanics (1946).

The solution may also be found from dimensional analysis of the system, under the assumptions that the blast wave is spherical; that the pressure in the blast wave is much larger than the surrounding atmospheric pressure; and that the total energy behind the shock remains constant. In this case,

$$r = C\, t^{2/5} E^{1/5} \rho_0^{-1/5}\,, \tag{2.19}$$

where r is the outer radius of the shock wave, C is a function whose value depends on the adiabatic index, t is the time since the energy was released into a small volume, E is the input kinetic energy, and ρ_0 is the density behind the shock. The Sedov–Taylor law is also scale invariant.

The Sedov–Taylor speed is the speed of a shock at position r as given by the differentiation with respect to time of (2.19),

$$v_{\text{S–T}} = \frac{dr}{dt} = \frac{2}{5}\, C\, t^{-3/5} E^{1/5} \rho_0^{-1/5}\,. \tag{2.20}$$

The quantity $\frac{2}{5}CE^{1/5}\rho_0^{-1/5}$ is not known in a typical experiment but, in this model, it is a constant of proportionality between v_{S-T} and $t^{-3/5}$. Therefore I call $\frac{2}{5}CE^{1/5}\rho_0^{-1/5}$ the *Sedov–Taylor quantity*. If the quantity, as measured by the graph of observed shock speed against $t^{-3/5}$, remains fixed, it is indicative of a Sedov–Taylor model being satisfactory in describing the shock evolution.

2.1.4. The Rankine–Hugoniot conditions, as applied at a shock in a magnetized medium.

The Rankine–Hugoniot equations describe the relationship between the physical variables of mass density, flow speed, gas pressure and specific internal energies, on either side of a one-dimensional shock (Landau & Lifshitz, 1987). For this reason the Rankine–Hugoniot equations are often known as the *shock jump conditions*. In the present case it is useful to extended them to include the effect of a background magnetic field, which may also be affected in magnitude and direction by the passage of the shock. (Fitzpatrick, 2011.)

Under the conditions of MHD, the jump conditions may be expressed as (Landau & Lifshitz, 1987)

$$\{\rho v_n\} = 0, \tag{2.21}$$

$$\left\{v_n\left(\frac{\rho v^2}{2} + \frac{\gamma p}{\gamma - 1}\right) + \frac{1}{4\pi}\left(v_n(B^2 - B_n \mathbf{v}\cdot\mathbf{B})\right)\right\} = 0, \tag{2.22}$$

$$\left\{p + \rho v_n^2 + \frac{1}{8\pi}\mathbf{B}_t^2\right\} = 0, \tag{2.23}$$

$$\left\{\rho v_n \mathbf{v}_t - \frac{1}{4\pi}B_n \mathbf{B}_t\right\} = 0, \text{ and,} \tag{2.24}$$

$$\{B_n \mathbf{v}_t - \mathbf{B}_t v_n\} = 0, \tag{2.25}$$

where the curly braces indicate taking the difference in the value of the enclosed quantity as evaluated on one side of the shock compared to the other, the subscript 'n' means the quantity in question as projected parallel along the shock normal (that is, the shock propagation direction), and the subscript 't' means the quantity in question as projected into the plane perpendicular to the shock normal.

2.1.5. Ionization of the neighbouring medium.

Ionization of the ambient medium well ahead of the outgoing plume material has been previously reported (Harilal *et al.*, 2006), including under similar conditions to my experiment (albeit at lower laser energy and with a metallic target) (Issac *et al.*, 1998). In that experiment, which like my experiments had a nitrogen atmosphere and a long pulse laser, the authors suggest that the atmosphere becomes ionized up to a few centimetres through electron collisions after prompt emission of electrons from the solid target within a few nanoseconds of the laser pulse. The production of these 'prompt' electrons emerges probably through the process of inverse bremsstrahlung at the laser-solid or laser-plasma interaction.

2.2. UPSTREAM WAVES AT PLANETARY BOW SHOCKS

2.2.1. Collisionless shocks.

Shocks in conventional fluids are transmitted principally by means of two-body collisions between the constituent particles of the fluid. The width of the shock transition is therefore no greater than a few collisional mean free paths, $\lambda_{\mathrm{mfp}} = (n\sigma)^{-1}$, where n is the gas number density and the collisional cross section is $\sigma \sim 10^{-23}$ cm. However in the interstellar medium the particle densities are rarely sufficiently high for the mean free path to be smaller than the system in question, and yet observations suggest that in the universe, shocks are replete: shocks that propagate in, for instance, supernovae remnants or in the interplanetary medium must be facilitated by an alternative mechanism (Balogh & Treumann, 2013).

In plasmas, the multiplicity of non-neutral particles enables the presence of collective particle effects through long-range electromagnetic interactions. The particles forming the plasma are not free to act independently interrupted only by occasional and discrete collisions with individual neighbours, but instead each particle is governed by the local electromagnetic fields. In place of elastic two-body collisions, an incident particle tends to suffer a large number of small, slight scatterings directly from close encounters with charges within its Debye sphere. However, if the density of charges is too low for this

process, then instead particles can scatter off small fluctuations in the local electromagnetic field; these fluctuations arise spontaneously from instabilities occurring at the flow interpenetration (Spitkovsky, 2008). In early literature the collisions occurring this way were called 'anomalous collisions'. This allows a transition region of much less than the classic mean free path to form (Treumann, 2009).

2.2.2. The Earth's bow shock.

The shock is hyperbolic in geometry, with a flat nose sitting about 14 Earth radii (R_E) from the Earth, extending around the planet with an extended tail persisting out to about 30 R_E. These distances vary slightly depending on the solar wind conditions. The shape of the shock means that no matter the solar wind magnetic field direction, there is always regions on the front where the shock normal lies perpendicular to the solar wind field, and regions where it lies parallel to the solar wind field (Balogh & Treumann, 2013). The bow shock itself, in terms of the electron heating scale, is about 20 km thick at its thinnest point (Schwartz *et al.*, 2011) and up to 1000 km thick if the foreshock regions are included.

These spatial scales make it difficult for space probes of only a few metres in size to investigate the macroscopic features of the shock, because local fluctuations often occlude the global properties. For instance even determining the macroscopic magnetic field direction is not trivial (Smith *et al.*, 1998). One answer to this problem is *Cluster II*[1], a constellation of four identical spacecraft that can be separated by several thousand kilometres to provide measurements from four positions simultaneously, enabling some inference of properties on that scale. However, the 'average' value of the properties over the probe separation cannot be measured, only the values local to the probe positions (Escoubet *et al.*, 2012). Nonetheless even this limited capability has yielded much unexpected information about the bow shock (Hobara *et al.*, 2007). Investigations of other collisionless shocks, such as the termination shock where the solar wind is decelerated by the interstellar medium, or around other magnetized bodies in the solar

[1] Cluster II replaced the original Cluster spacecraft, which unfortunately were destroyed during their launch because of an unhandled integer overflow in the flight control software.

system, will receive necessarily less investigation by *in situ* probing, but the surprising information such missions yield suggest the structure of these shocks is still poorly understood. (Stone *et al.*, 2008.)

Magnetohydrodynamic and particle-in-cell ('PIC') simulations of the bow shock have also been informative in understanding the interplay of the numerous physical processes occurring within the shock, but the sheer breadth of spatial and temporal scales makes accessing simultaneously both the macro- and micro-physics computationally challenging (Burgess & Scholer, 2013).

2.2.3. The parallel shock and upstream waves.

Where the angle between the shock normal and the local magnetic field is shallow, that is, the shock normal and magnetic field vectors are co-aligned or nearly co-aligned, the shock is called a *parallel shock*. (Some authors distinguish between a 'parallel' shock, where the angle is at or very close to the parallel vector, and call shocks close to 45° of the parallel *quasiparallel shocks*.) In a perpendicular collisionless shock, where the shock propagates perpendicular to the field lines, gyrating particles are fixed to within one gyroradius of the shock front, neglecting drift and scattering. With a parallel shock, however, particles are free to stream up and down the field lines leading away from the shock: when a mechanism exists for reflecting or scattering upstream particles close to the front, the result is an extended, turbulent foreshock preceding the shock transition, instead, as in the case of perpendicular or unmagnetized shocks, of the sharp shock foot a small number of gyroradii or collisional mean-free-paths wide. In the case of the Earth's bow shock, observations show that the parallel foreshock is populated by a reflected ion and electron component, counterstreaming against the incoming flow. This is a condition unstable to the production of electromagnetic waves (Balogh & Treumann, 2013), and consequently, the upstream region is populated by a great number of distinct wave species (Burgess, 1997).

In the Earth's bow shock, the foreshock may be further divided into the electron and ion foreshocks. Electrons have a greater thermal speed than ions of the same temperature: as the bow shock curves away from the field lines, electrons have a slight advantage in outpacing the counterstreaming bulk plasma and consequently a region of reflected

electrons in absence of the ionic component is present. This part is called the electron foreshock.

Burgess (1997) wrote a short review of observations of the varied wave species in the foreshock. Together with data from other sources (Balogh & Treumann, 2013; Dubinin *et al.*, 2007; Hobara *et al.*, 2007; Selzer *et al.*, 2014) I have adapted the low frequency waves discussed in his paper into Table 1.

Of particular interest are the whistler bursts or 'lion roars' whose origins are not fully understood except that they appear to be related to an electron beam instability (Tokar *et al.*, 1984). It is known that a relatively hot beam of electrons propagating along a magnetic field through a cooler, Maxwellized plasma is unstable to the production of whistler waves (Gary, 1985), particularly if the hot beam has a temperature anisotropy in respect of the thermal distribution in the plane parallel to the field and that along it. A monochromatic beam of electrons may also produce chirping whistlers; this effect recently found experimental verification (Van Compernolle *et al.*, 2015). Whistler bursts in the foreshock are more typically 'hiss' like, that is, displaying a broad spectrum without clear chirping.

Table 1. Observed low frequency waves in the Earth's foreshock. All values are approximate.

Name(s)	**Mode**	**Typical frequency**	**Typical wave-length**	**Amplitude** ($\Delta B/B$)	**Source**
ULF waves[a]	Fast, Alfvén-ion cyclotron, and whistler	5–200 mHz; 0.01 ω_{ci}	10–100 km	0.2–1.0	Field-aligned ion beams
SLAMS, Large Amplitude Pulsations	As above	30 mHz	1000 km	5	Possibly steepening of ULF waves
3 Second Waves	Right-handed	0.3 Hz	500–3500 km	0.5	Unknown
1 Hz whistlers[b]	Mostly right-handed	0.5–4 Hz; 10–100 ω_{ci}	10–100 km	0.2	Possibly field-aligned ion beam
Whistler bursts, 'lion roars'	Mostly right-handed	40–100 Hz	10 km	0.5	Possibly field-aligned electron beams

[a] Some authors call all waves below 10 Hz 'ULF waves'. [b] '1 Hz' waves have frequencies of 1 Hz in spacecraft frame, but higher in the plasma frame.

2.3. UPSTREAM WAVES IN THE LABORATORY

2.3.1. Whistler waves.

Whistler waves, or electron cyclotron waves, are one species of mode that can propagate in a plasma with an imposed magnetic field. This derivation is adapted from Fitzpatrick (2011). Consider homogenous, quasi-neutral plasma, in which both plasma species are at rest. For small perturbations, that is waves of small amplitude, we may apply a linear approximation: each wave supported by the system may be expressed as the sum of plane waves, each of the form

$$\mathbf{E} = \mathbf{E}_{\mathbf{k}} \exp\{i(\boldsymbol{k} \cdot \boldsymbol{x} - \omega t)\}. \tag{2.26}$$

The plasma current is specified by

$$\mathbf{j} = \boldsymbol{\sigma} \cdot \mathbf{E}. \tag{2.27}$$

where $\boldsymbol{\sigma}$ is the plasma conductivity tensor.

In the context of the plane wave functions, the differential operators may be replaced by

$$\frac{\partial}{\partial t} \rightarrow -i\omega, \text{ and } \boldsymbol{\nabla} \rightarrow i\mathbf{k}. \tag{2.28}$$

Insertion into the Maxwell equations gives

$$i\mathbf{k} \wedge \mathbf{E} = -\frac{1}{c} \cdot -i\omega \cdot \mathbf{B}, \text{ and} \tag{2.29}$$

$$i\mathbf{k} \wedge \mathbf{B} = \frac{4\pi}{c} \boldsymbol{\sigma} \cdot \mathbf{E} + \frac{1}{c} \cdot -i\omega \mathbf{E}. \tag{2.30}$$

These equations must be satisfied for a wave (or wave component) of frequency ω to exist in the plasma. With some re-arrangement an explicit condition can be extracted.

$$\left(\mathbf{kk} - \mathbf{1}k^2 + \frac{\omega^2}{c^2} \left\{ \mathbf{1} + \frac{i4\pi}{\omega} \boldsymbol{\sigma} \right\} \right) \cdot \mathbf{E} = 0. \tag{2.31}$$

Turning now to the case where a background magnetic field is imposed on the z-axis, with the wave vector $\mathbf{k}$ propagating parallel to the field, a solution to (2.4) is supplied under the condition that

$$\begin{pmatrix} S - N^2 & -iD & 0 \\ iD & S - N^2 & 0 \\ 0 & 0 & P \end{pmatrix} \begin{pmatrix} E_x \\ E_y \\ E_z \end{pmatrix} = \mathbf{0}. \tag{2.32}$$

Here, N is the unknown refractive index of the plasma and the electric field vector is expressed in component form, $\mathbf{E} = (E_x, E_y, E_z)$. Further, cold plasma theory gives $S = (R + L)/2$, $D = (R - L)/2$,

$$R = 1 - \frac{\omega_{pe}^2}{(\omega + \omega_{ce})(\omega + \omega_{ci})} \text{ , and} \tag{2.33}$$

$$L = 1 - \frac{\omega_{pe}^2}{(\omega - \omega_{ce})(\omega - \omega_{ci})} \text{ .} \tag{2.34}$$

The right-handed wave solution is $N^2 = R$ with eigenvector $(E_x, iE_x, 0)$ and the left-handed solution is $N^2 = L$ with eigenvector $(E_x, -iE_x, 0)$. The term P in (2.32) is a longitudinal mode I do not discuss further. The refractive index N ties the frequency and wavenumbers together under the relation $N = |\mathbf{N}|$, $\mathbf{N} = c\mathbf{k}/\omega$.

2.3.2. The dispersion equation for transmission through a collisional medium.

The atmosphere through which our whistler modes are expected to propagate in the laboratory is quite different to that encountered in many experiments and indeed in space in general. For one, there are collisions; whistler waves are usually observed in collisionless media. However, the lower ionosphere of Venus is understood to support whistler waves despite the presence of collisions that act to damp the wave through Joule dissipation (Daniels *et al.*, 2012; Strangeway, 1997, 2000).

The presence of electron collisions affects the dispersion equation. One way to model this is to add a collision term to the dispersion equation modelling the transport of waves through the medium. For the purposes of modelling this transport, I assume that the plasma is now at a single temperature, that is, without the presence of the warm electrons from behind the shock front. In this case the wave dispersion curve becomes

$$\frac{c^2k^2}{\omega^2} = 1 + \frac{\omega_{pe}^2}{\sqrt{2}\omega k v_{Te}} \cdot Z\left\{\frac{\omega + i\nu_{ee} - \omega_{ce}}{\sqrt{2}kv_{Te}}\right\}, \tag{2.35}$$

where $Z(\zeta)$ is the plasma dispersion function,

$$Z(\zeta) = \frac{1}{\sqrt{\pi}} \int_{-\infty}^{+\infty} \frac{e^{-t^2}}{t - \zeta}\, dt; \tag{2.36}$$

k is the wave number, ω is the frequency of the radiation, ν_{ee} is the electron collision rate within the transmission medium, and the other symbols have their usual meanings. For the purposes of computing $Z(\zeta)$ it is more convenient to use an alternative form,

$$Z(\zeta) = 2i \exp(-\zeta^2) \int_{-\infty}^{i\zeta} -t^2 \, dt = i\pi e^{-\zeta^2} \mathrm{erfc}\,(-iz), \tag{2.37}$$

where $\mathrm{erfc}(z)$ is the complementary error function. This avoids the difficulty of branch cuts during the integration.

2.3.3. The collisional dispersion equation cast into a non-dimensional form.

Solving this equation numerically is quite intractable, due to the presence of large numbers such as $\omega_{pe}^2 \sim 10^{24}$, even with a modern computer package such as `Mathematica`—which claims to be comfortable manipulating numbers in excess of $10^{10^{15}}$. (I believe the difficulty arises in the estimation of the integral in (2.37).) Therefore, it is helpful to recast equation (2.35) in a dimensionless form. I take each physical parameter and express it a scalar multiplier of a fixed physical value, *viz.*—

$$k = k^* k_0, \;\; \omega = \omega^* \omega_0, \;\; \omega_{ce} = \omega_{ce}^* \omega_{ce0}, \;\; \omega_{pe} = \omega_{pe}^* \omega_{pe0}, \;\; \nu_{ee} = \nu_{ee}^* \nu_{ee0}. \tag{2.38}$$

The symbols appended with asterisks are dimensionless numbers, intended to be of order unity (or thereabouts); the symbols appended with a zero subscript are those holding the dimensions of the system. Careful choice in the latter will eliminate the presence of these large numbers from (2.35) entirely. As it will transpire that ω_{pe} is the problem, let us set $\omega_0 \sim 10^9$ Hz.

The reason for requiring the other frequencies to be referenced against the same standard follows from a wish to retain the basic form of (2.35) under the transformation into a non-dimensional system. To illustrate that, consider the argument of the dispersion function Z in (2.35), expressed in the new dimensionless parameters.

$$\frac{\omega + i\nu_{ee} - \omega_{ce}}{\sqrt{2} k v_{Te}} \rightarrow \frac{\omega^* \omega_0 + i\nu_{ee}^* \nu_{ee0} - \omega_{ce}^* \omega_{ce0}}{\sqrt{2} k^* k_0 v_{Te}^* v_{Te}}$$

With a careful choice of the 0-suffixed parameters in both the numerator and the denominator, it will be possible to eliminate all such parameters leaving only the asterisked, non-dimensional variables.

The equation finally is

$$\frac{k^{*2}}{\omega^{*2}} = 1 + \frac{1}{\omega^* k^* v_{Te}^*} \cdot Z\left\{\frac{\omega^* + i\nu_{ee}^* - \omega_{ce}^*}{k^* v_{Te}^*}\right\}. \tag{2.39}$$

This can be solved numerically to find the damping rate due to collisions for a whistler wave travelling through a collisional medium.

2.3.4. Mechanisms for exciting waves in the laboratory.

Consider the shock propagating through our laboratory system as depicted in Figure 2.1. Matter flows from bottom to top, slowing at the shock front boundary, where it is heated. The system is immersed in a magnetic field, which is arranged parallel to the direction of shock travel. Because the shock is mediated by ions, if the mean free path of the electrons exceeds that of the ion population, shock-heated electrons may disperse a few mean free path lengths forward of the front, whereupon there is now a two-temperature fluid in the electron population. The hot electron fluid also has a drift velocity with respect to the unshocked fluid. It will be demonstrated that this configuration is unstable to the emission of whistler waves in the forward direction, along the field lines. In the absence of a magnetic field, this effect does not occur.

We assume the system is partially ionized, is homogeneous away from the shock front and is immersed in a uniform, straight magnetic field. The shock propagates in a direction parallel to the field lines. The electrons are magnetized; that is to say that they are able to complete partial Larmor orbits before being scattered by collisions, but in the laboratory the ions are not magnetized.

The electron-electron mean free path will be found in our experiments to be of order the shock thickness. Therefore a minority component of hot electrons are able to diffuse ahead of the shock front and permeate the unshocked plasma ahead of the front.

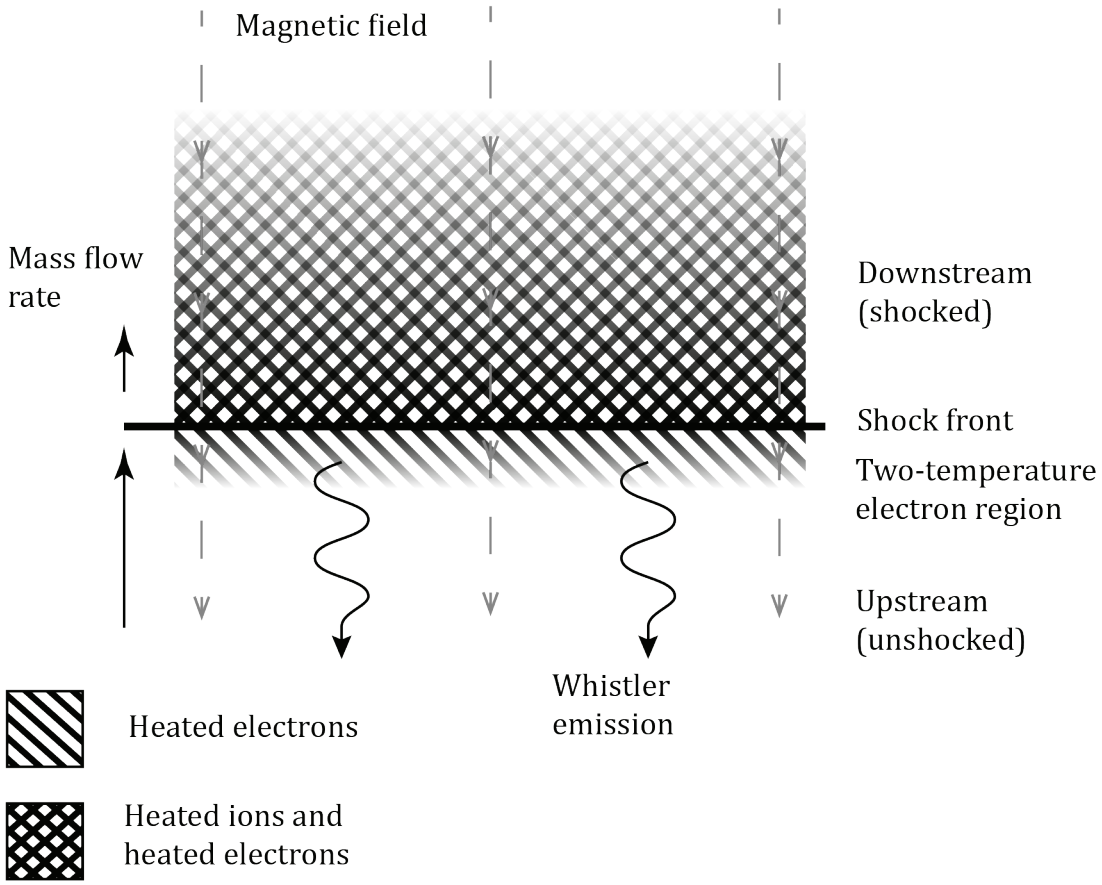

Figure 2.1. A model for the shock system, in the frame where the shock is stationary.

This two-component electron distribution gives rise to an MHD instability in the plasma, which acts to produce whistler waves directed upstream. To see this I turn to the analysis of S. Peter Gary (1985). Gary considers a beam of heated electrons drifting into a homogeneous cooler, collisionless, background plasma. The beam travels parallel to a straight magnetic field. The dispersion relation of the combined system is computed from linear theory, to find that the system is unstable in some conditions to a whistler growth mode.

Therefore the system consists of three components: an ionic background, an electron background, and a hot, drifting electron component. In adapting the model to my system, the hot components are drifting because they originated from the downstream, shocked plasma. Once the distribution function of this three-component plasma is determined, its dispersion equation may be deduced, and the various allowed modes

evaluated for their stability. I shall show that, under certain parameter ranges, an upstream-propagating whistler mode arises and is unstable to a growth condition.

For the j^{th} species, the distribution function is (Gary, 1985)

$$f_j^{(0)}(\mathbf{v}) = \frac{n_j T_{\parallel j}}{\left(2\pi v_j^2\right)^{\frac{3}{2}} T_{\perp j}} \exp\left\{-\frac{\left(v_z - v_{0j}\right)^2}{2v_j^2} - \frac{v_x^2 + v_y^2}{2v_j^2}\frac{T_{\parallel j}}{T_{\perp j}}\right\}, \tag{2.40}$$

where, for species j, n_j is the number density, $T_{\parallel j}$ is the parallel temperature, $T_{\perp j}$ is the perpendicular temperature, v_j is the thermal speed, v_{0j} is the species drift velocity, and v_x, v_y, and v_z are the velocity components.

Now, if we look only at the transverse modes (*i.e.,* modes propagating parallel with disturbances perpendicular to the field lines), consideration of the linearized Vlasov equation shows that the dispersion curves will satisfy

$$\omega^2 - k^2c^2 + k^2c^2 \sum_j S_j^{\pm}(\mathbf{k}, \omega) = 0, \tag{2.41}$$

where $S_j^{\pm}$ are the dimensionless conductivities of the individual components: explicitly

$$S_j^{\pm}(\mathbf{k}, \omega) = \frac{\omega_j^2}{k^2c^2}\left(\zeta_j Z\left(\zeta_j^{\pm}\right) + \frac{1}{2}\left(1 - \frac{T_{\perp j}}{T_{\parallel j}}\right) Z'\left(\zeta_j^{\pm}\right)\right); \tag{2.42}$$

Z has the meaning given in (2.36) and

$$Z'(\zeta) = \frac{1}{\sqrt{\pi}}\int_{-\infty}^{+\infty} \frac{e^{-t^2}}{(t-\zeta)^2}\, dt = -2\{1 + \zeta Z(\zeta)\}; \tag{2.43}$$

with also the useful quantities

$$\zeta_j = \frac{1}{\sqrt{2}kv_j}\left(\omega - \mathbf{k}\cdot\mathbf{v}_{0j}\right),$$

$$\zeta_j^{\pm} = \frac{1}{\sqrt{2}kv_j}\left(\omega - \mathbf{k}\cdot\mathbf{v}_{0j} \pm \Omega_j\right), \text{ and,}$$

$$k = |k_z|.$$

The $\pm$ sign refers to waves of right-handed $(+)$ and left-handed $(-)$ polarizations respectively, viewed along the field lines.

Gary was concerned with beams where the parallel and perpendicular temperatures may be unequal, but in my experiments, the relatively weak magnetic field strength and the relatively high collisionality makes it unlikely that the quantity $T_\perp/T_\parallel$ deviates much

from unity. Therefore the conductivity of each plasma component satisfies

$$S_j^{\pm}(\mathbf{k},\omega) = \frac{\omega_j^2}{k^2c^2}\{\zeta_j Z(\zeta_j^{\pm})\}. \tag{2.44}$$

For numerical stability I have found it is useful to normalize the dimensional quantities, under the scheme $\omega \to \omega^*\omega_0$ for all frequencies; $k \to k^*\omega_0/c$; and for all speeds, $v \to v^*c$, with c the vacuum speed of light, where the asterisk denotes the dimensionless quantity. I set $\omega_0 = 10^9$ Hz. The form of (2.41) is not affected by the re-scaling of variables; a longer discussion of this process is presented in section 2.3.3.

In the case of the experiments I describe, the conductivity is dominated by the electronic contributions to the fluid with the ionic fraction becoming negligible. This essentially follows from the fact that $\omega_{pi} \ll \omega_{pe}$, and therefore contributions arising in the ionic component may be neglected.

Nonetheless the practical evaluation of (2.41) is not entirely straightforward; the complementary error function in particular is sensitive to large values on the imaginary axis and can produce numbers not representable on 64 bit arithmetic hardware.

I create a list of values of k^*, and use the commercially available `Mathematica` software to find numerically the global minimum of the dispersion function given on the left hand side of (2.41) for each k^*, with 100 kHz $< \Re(\omega) <$ 10 GHz and $|\Im(\omega)| <$ 10 GHz. I find that the dispersion function reaches within 10^{-8} of zero quickly, in which case I accept the value of ω as the solution for that value of k; or else it diverges. I discard the divergent quantities as not satisfying the equation; and in this manner construct a graph of ω against k. With the assistance of a modern sixteen-core machine, `Mathematica` takes about five minutes to create a graph of the function with approximately twelve hundred values of k spread logarithmically over the expected range. An example of such a graph is given in Figure 2.2.

Figure 2.2 shows a solid curve representing the real part of the dispersion function; plotting the wave frequency ω against the wave number k. There are also two dashed curves showing the imaginary part of the dispersion curve; the curve with the shorter dashing shows regions of growth, whereas the longer curve shows damping regions. In the graph in this case, there is a region where strong growth would be expected, corresponding to a frequency of about 60 MHz.

I repeat this analysis over several mean free path lengths, dropping the averaged hot electron fraction with each penetration length. After five 'layers' the instability has dropped below an excitation threshold of approximately 100 e-folding times per second.

Whether this process can cause waves to be pushed upstream is a separate matter; for the waves to propagate away from the shock their phase velocity must exceed the shock speed and therefore the Alfvénic speed by some distance.

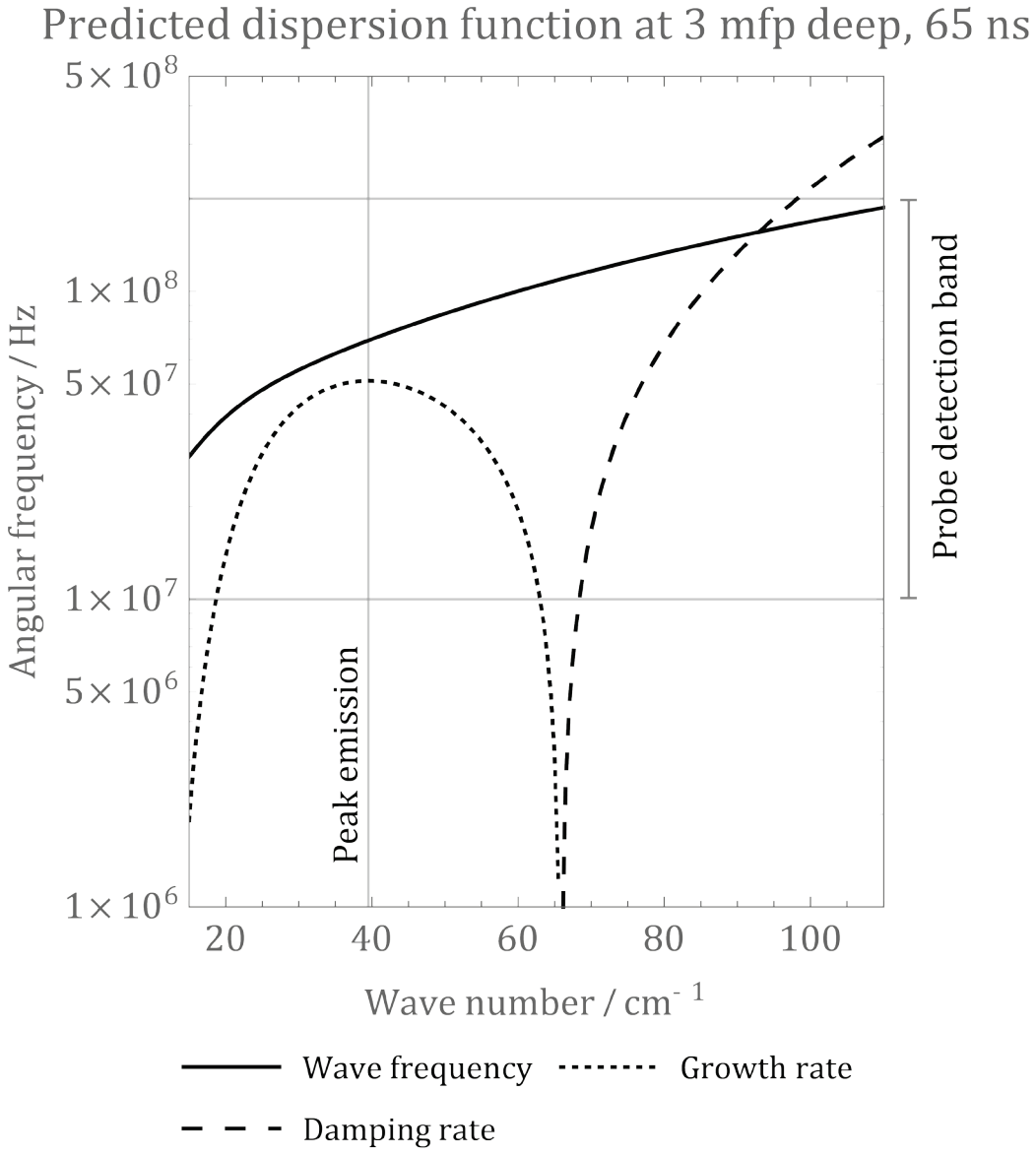

Figure 2.2. The dispersion curve, in a thin slice ahead of a shock, as estimated from a laboratory experiment. A mode unstable to rapid growth is visible.

2.4. CHAPTER SUMMARY

The experiment is modelled as an expanding shock front propagating through the atmosphere. The region in front of the shock is considered to include a 'beam' of shock-heated electrons diffusing from the downstream, hot side of the shock. The region is proposed to exist for several mean free paths, with decreasing beam density as calculated from the mean free path estimates. The presence of a hot beam of electrons propagating along a field line is unstable to whistler wave emission; the dispersion curve and the instability growth rate are calculated. Beyond this region the damping characteristic of the plasma can be considered; that is, the atmosphere between the excitation region and the probe is considered to be a transmission region. The plasma is collisional; and this damps the propagation of these waves. The physical parameters of these regions are tuned by measurements taken during the experiment (but bdot probe measurements are not used in this tuning).

3. INSTRUMENTATION

The results of this thesis are largely contingent on the quality of the experimental data collected supporting them; and that quality flows from an understanding of the measuring instruments. In particular my results are dependent on the limitations of 'bdot' probes, which are a kind of magnetic field probe. Therefore, in this chapter I discuss in some detail the nature and design of bdot probes, including their limitations and shortcomings. I also review optical interferometry of the Nomarski type, from which inference of electron densities can be made; and I look at electron spectrometry techniques, for estimating the energy profile of free electrons. My aim is to understand how estimates of physical quantities can be extracted from the data they yield, and how reliable those estimates can be.

The interferometry data will be used to infer the electron number densities, with both spatial and temporal resolution (subject to the constraints that I discuss). The profile and evolution of the electron densities is used to constrain the computational models that I later use to understand my experiments. The bdot probes collect magnetic field data, resolved with time, and under appropriate signal processing, they detect whistler-like waves in one class of experiment. The electron spectrometer gives me some idea of the 'background' electron spectrum present in the experiments.

3.1. BDOT PROBES AND MAGNETIC FIELDS

A good deal of this thesis concerns magnetic field measurements collected by means of a 'bdot probe' (the pronunciation of 'bdot' is /ˈbiː.dɒt/). For that reason it is expedient to give a description of the design of the probe, to review how physical values are deduced from its measurements, and to discuss the limits of the probe's measuring capabilities.

The information in this part is sourced in particular from Huddlestone and Leonard (1965, pp. 72–79), Phillips and Turner (1965), and Hutchinson (2002, pp. 11–13); and for the specific design of probe used here, Everson *et al.* (2009).

3.1.1. The basic design of a bdot probe.

In Figure 3.1, I provide a photograph of the external chassis of a bdot probe, and in Figure 3.2 a schematic diagram of the entire bdot probe is presented (kindly supplied by E. Everson). The probe tip, on the left in the photograph and in the diagram, houses the element that detects changes in the magnetic field. The black mark circling the tip in the photograph marks the position of the sensitive element. The thicker end, on the right, contains connections for external cabling; and the long shaft between the tip and the external connection enables the probe to be placed some distance from the thick, external wiring—which would be inconvenient in the tight confines of a laser-plasma experiment. The shaft also protects the fragile internal wiring. The black markings on the case in the photograph assist with orientation and proper positioning of the probe.

Inside the tip, the three-axis bdot probe contains a set of three conducting coils, with each coil oriented such that its axis is orthogonal to the axes of the other two coils Actually, because the coils are counter-wound in the real probe, there are six coils (and a

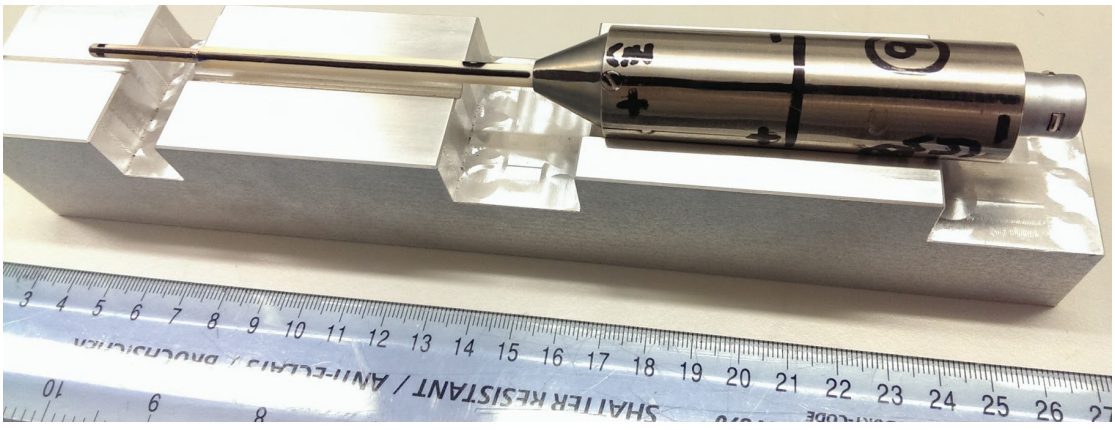

Figure 3.1. A photograph of a bdot probe, with a centimetre scale.
The probe is shown placed atop a metallic packaging block. The tip containing the core is on the left. This photograph was taken by J. Cross.

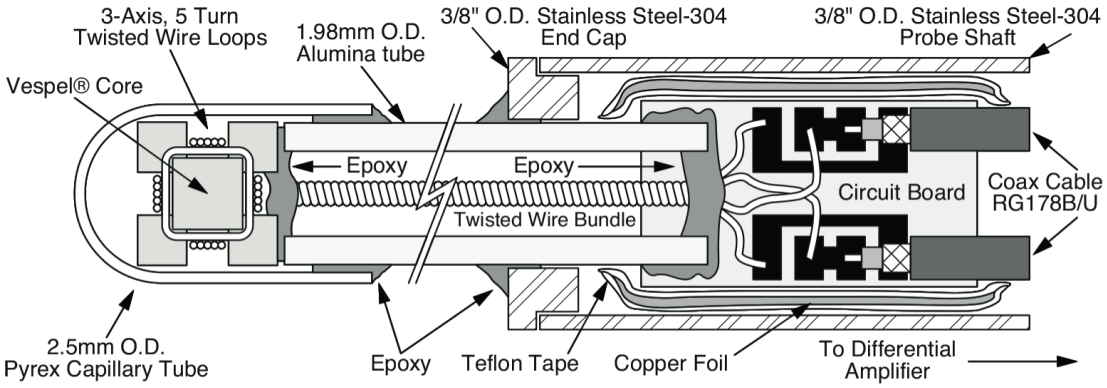

Figure 3.2. A schematic of the entire bdot probe package.
Taken from Everson *et al.* (2009), with the leading author's gracious permission.

dummy coil), but it is convenient for the moment to consider a slightly simpler design with only three sensitive coils. Therefore together the three axes, one through the face of each coil, form the axes of a three-dimensional Cartesian coordinate system. The coils are electrically independent, and are co-located by being wrapped around a single cube of known magnetic permeability. (Everson *et al.*, 2009.) This is depicted in Figure 3.3. The probe tip consists of a central cube; a coil is wound around each of the three axes, to give three coils in total. Two of those three coils are shown in this projection; in our experiments the cube has a face side of approximate area of 1 mm^2, or in the case of an alternative probe design, 3 mm^2.

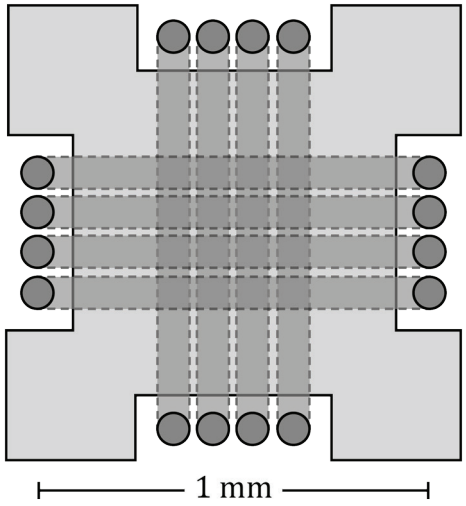

Figure 3.3. A schematic of the bdot probe tip.

The conducting coils are attached to appropriate electronics where the voltage induced by the magnetic field may be measured with the motion of time. From knowledge of the geometry of the coils, in particular the areas they each enclose and their electrical reactances, the change in the magnetic field (hereafter '**B** field') passing through each coil may be deduced. The voltage measured may be integrated over time to give the **B** field as a function of time; at least up to an integration constant which represents the initial field—in practice this is usually zero. The use of three orthogonal coils enables the spatial orientation of the **B** field to be recovered.

3.1.2. Magnetic coils and their basic properties.

The probe relies on the principle of magnetic induction; that is, a change in the local magnetic field produces an electromotive force ('e.m.f.') in the conducting coils. This is a manifestation of the Maxwell–Faraday law, $\partial\mathbf{B}/\partial t = -\nabla \wedge \mathbf{E}$ (whence the simple etymology 'bdot probe' arises). To apply this to a simple wire loop, I follow the derivation in Hutchinson (2002, pp. 11–13) by invoking the Kelvin–Stokes theorem to rewrite Faraday's law in the integral formulation, *i.e.*,

$$\oint_{\partial\Sigma} \mathbf{E} \cdot \mathbf{dl} = -\iint_{\Sigma} \frac{\partial}{\partial t}\mathbf{B} \cdot \mathbf{dS}, \tag{3.1}$$

where the integral on the right-hand side is performed over the contiguous two-dimensional region $\Sigma \subset \mathbb{R}^2$ (here that region is assumed constant with time) and the left-hand side integral is performed on the closed curve $\partial\Sigma$ forming the boundary of the said region. **dS** is an infinitesimal element of area projected normal to Σ at every point at which it is evaluated.

Suppose now that $\partial\Sigma$ is embedded in the conducting coil, so that Σ is the area enclosed by the coil: see Figure 3.4. The coil is shown as a simple loop, surrounding a region Σ, in which a non-constant magnetic field lies. In a real design, the area between the connecting wires is kept as small as possible, perhaps by twisting the connecting wires together. However, that region still counts, so it is shown in the figure. For now I assume for simplicity that the coil acts as an open circuit, neglecting is reactance. Then, $\partial\Sigma$ consists of two parts, the part within the coil (including the connecting wires) and an arbitrarily short section linking the ends of the open coil. In practise, this 'linking'

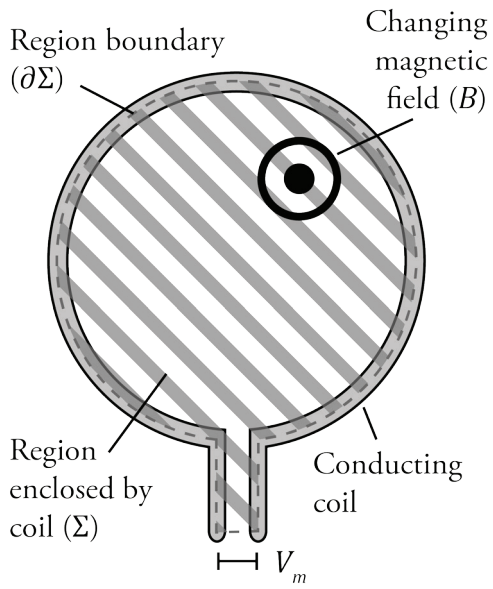

Figure 3.4. Deriving the voltage induced across a coil in a changing magnetic field.

section occurs inside the voltage measuring electronics. Using the principle of linearity to express the total integral as the sum of those geometrical components, the left-hand side of (3.1) becomes

$$\oint_{\partial\Sigma} \mathbf{E}\cdot\mathbf{dl} = \int_{\text{coil}} \mathbf{E}\cdot\mathbf{dl} + \int_{\text{ends}} \mathbf{E}\cdot\mathbf{dl} = 0 + V_m = V_m. \tag{3.2}$$

The coil itself is a conductor, so the electric field in it may, to first order, be regarded to vanish. The electric field between the ends of the coil is the voltage induced across it by the **B** field—and this (V_m in Figure 3.4) is the potential we measure.

Reviewing the right-hand side of (3.1), Σ is the area enclosed by the total coil-wire structure. Let us suppose the connecting-wire area is negligible. If the coil consists of N identical loops each of area A, this is a total area of $N \cdot A$; and, taking B to be the mean magnetic field through Σ, projected normal to Σ, the result $V_m = N \cdot A \cdot dB/dt$ follows. With re-arrangement and under temporal integration we obtain

$$B(t) = \frac{1}{AN}\int_{-\infty}^{t} V_m(t)dt. \tag{3.3}$$

In many applications it will be found to be impractical to perform the measurement over the entirety of the preceding time, and therefore I will assume the initial value $B(0)$ is known (usually it is zero), and we rewrite this equation as

$$B(t) = \frac{1}{AN}\int_0^t V_m(t)dt + B(0). \tag{3.4}$$

It should be underscored that this derivation relied on the principle that there was no electric field within the coil conductor itself. This is true for a slowly varying **B** field, but in the circumstances I describe later in this thesis it is necessary to take the reactance of the coil into consideration.

3.1.3. The elimination of electric effects.

The design presented in section 3.1.2 is the simplest bdot probe; and upon it several improvements can be made. A principle problem with implementing such a design in laser-plasma experiments as I later describe is the presence of large electrical fields, arising both directly from the laser-plasma interaction and possibly later in the ensuing plasma dynamics. These electric fields also act to drive currents in the bdot coils, and the distinction between electric and magnetic effects cannot be made in the previous-given design. (See in particular Everson *et al.*, 2009.)

To remedy this shortcoming, we use twin-twisted, counter-wound wire. That is to say, the single wire of each coil is replaced with two electrically independent wires, twisted together: such that there are now two coils per axis. In this case the presence of an external electric field acts equally on charges present in the coil, and, because of the counter-directed winding, a voltage of the same polarity arises on each coil on the axis coil-pair. However, the magnetic field induces a voltage of opposite polarity. Therefore subtracting one from the other gives twice the magnetic field and eliminates contributions arising from an external electric field.

3.1.4. The full circuit equation for a single coil.

In the derivation given for a simple coil in section 3.1.2 above, the effect of electric fields arising within the coil was neglected. In fact, the coil has some degree of reactance and it is expedient to consider this particularly when looking at measurements of high frequency fields (meaning, in the present case, $\omega \gtrsim 30$ MHz). Following Everson *et al.* (2009) and Huddlestone and Leonard (1965), the bdot probe coil may be modelled as a circuit as in Figure 3.5. The **B** field is understood to induce a voltage V_{in}, and the

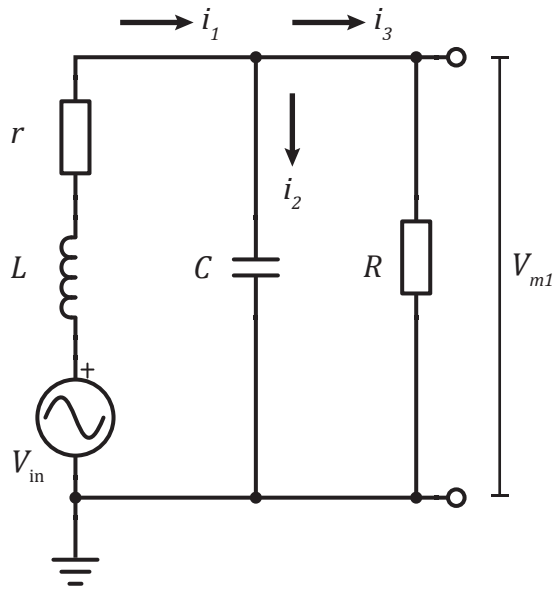

Figure 3.5. The electrical model of a single bdot coil.

measured voltage across the coil is V_{m1}. The loop has internal resistance r, self-inductance L, capacitance C, and suffers a load resistance R. The flow of three currents i_1, i_2, and i_3 are shown.

We suppose the magnetic field induces a voltage V_{in}, sufficient to drive a current i_1 through the inductor L (against its internal resistance r). Applying Kirchhoff's voltage law (the sum of all e.m.f.s in a closed loop is zero) around the outer loop and understanding that the supplied voltage $V_{\text{in}} = AN\, dB/dt$, we find that

$$AN\frac{dB}{dt} = i_1 r + L\frac{di_1}{dt} + i_3 R. \tag{3.5}$$

Now, by applying Kirchhoff's current law to the central node on the top rail, above the capacitor, we are constrained by $i_1 = i_2 + i_3$. Inspection of the circuit components reveals that

$$i_2 = C\frac{dV_{m1}}{dt} \quad \text{and} \quad i_3 = V_{m1}R. \tag{3.6}$$

Since the coil is one of a counter-wound pair, the finite mutual inductance M between the two must be included, and we replace the inductance L in (3.5) with the total inductance $L + M$, where L is now the self-inductance of the individual coil. After some rearrangement, we have the circuit equation for an individual bdot probe coil.

$$AN\frac{d}{dt}B(t) = \left(1+\frac{r}{R}\right)V_{m1}(t) + \left(\frac{L+M}{R}+rC\right)\frac{d}{dt}V_{m1}(t) + (L+M)C\frac{d^2}{dt^2}V_{m1}(t) \tag{3.7}$$

We expect $r/R \sim 0$ in a practical design. Further, we define the coil's time constant $\tau = (L+M)/R$, which is a measure of how quickly an induced current will decay and therefore τ governs the temporal response of the coil. Applying these considerations and integrating over the measurement time gives a correction to (3.4);

$$B(t) = \frac{1}{AN}\left\{\left(\int V_{m1}(t)dt\right) + (\tau + rC)V_{m1}(t) + RC\tau\frac{d}{dt}V_{m1}(t)\right\}. \tag{3.8}$$

Here I have suppressed the field at zero time, and the integral is understood to be over the measurement time preceding the time point t. The differences between (3.8) and (3.4) are associated with the fact that, as the coil has a non-zero inductance, it opposes changes to the e.m.f.s arising within it. As such, the instantaneous voltage represents a contribution to the **B** field, at least for high frequency fields. The final term arises because in the limit of very high frequency fields, the capacitor in Figure 3.5 will act as a short.

During the calibration of the probe, it becomes clear that the self-capacitance is negligible over the frequency range of interest ($\omega \ll 1/RC \ll 1/rC$). In this limit, we approximate $C \to 0$ and the expression for finding the relevant **B** field projection from the measured voltage is

$$B(t) = \frac{1}{AN}\left\{\left(\int V_{m1}(t)dt\right) + \tau V_{m1}(t)\right\}. \tag{3.9}$$

To see the effect of the **B** field frequency on the voltage response more explicitly, it is helpful to recast (3.7) in Fourier space with $V_{m1}(\omega)$ as a function of $B(\omega)$.

$$V_{m1}(\omega) = AN\frac{\omega^2(\tau+rC) + i(\omega - RC\tau\omega^3)}{(1-RC\tau\omega^2)^2 + \omega^2(\tau+rC)^2}B(\omega), \tag{3.10}$$

or, with $C \to 0$,

$$V_{m1}(\omega) = AN\frac{\omega(\omega\tau + i)}{1+\omega^2\tau^2}B(\omega). \tag{3.11}$$

At low frequencies ($\omega\tau \ll 1$), the response amplitude is proportional to frequency, but at high frequencies ($\omega\tau \gg 1$) the frequency dependence is suppressed. In the design of a practical probe, including the ones I used in the experiments discussed later, $\tau \sim 30$ ns and so this transition occurs at around $\omega \sim 30$ MHz.

3.1.5. The full circuit equation for a counter-wound coil.

Each of the three real coils consists of two loops wound together, and differentially amplified, as discussed in section 3.1.3. The winding process ensures that the two coils in each pair have the same geometry and therefore the same electrical properties, and they do not otherwise differ but by the position of the electrical ground and their polarity. So, under these assumptions, the potential across the second loop is $V_{m2} = -V_{m1}$, and therefore the expression for $B(t)$ in terms of the differentially amplified voltage $V_m = g(V_{m1} - V_{m2})$ is

$$B(t) = \frac{1}{2gAN}\left\{\left(\int V_m(t)dt\right) + \tau V_m(t)\right\}, \tag{3.12}$$

where g is the amplification factor. There are alternative integration schemes to that of (3.12) (see Everson *et al.*, 2009), but in practise I have found that the results they give do not differ in any material way from the straightforward integration. Therefore, this is the scheme that I use in this thesis.

3.1.6. Calibrating the probe.

Bdot probes are handmade devices, and the variable geometry arising from the manual winding of each coil gives rise to errors to the design values of A, τ, and C for each of the three coils on an individual probe, as well as between different probes. In particular it will be seen immediately that a small error in the area enclosed A will render measurements of the magnitude of the **B** field quite inaccurate, but, because of (3.11), at high frequencies the dependence on τ also becomes increasingly pertinent; such a misestimation would lead to errors in comparing the relative amplitudes of different frequency components.

The small size of the probe means that it is not practical to measure the geometry directly, so instead the probe is placed in an oscillating **B** field of known orientation, magnitude and frequency, and its response measured. The field is generated by a Helmholtz coil powered by a network analyser; at higher frequencies (above 500 kHz) the inductance of the Helmholtz coil means that it is necessary to use a straight wire to generate the field instead.

With a known **B** field applied along the axis to be measured, the probe's response in Fourier space may be characterized as

$$V_m(\omega) = 2gAN\frac{\omega(\omega\tau + i)}{1+\omega^2\tau^2}B_{app}(\omega)\mathrm{e}^{i\omega\tau_d}, \tag{3.13}$$

where $V_m(\omega)$ is the measured voltage arising across the coil pair, $B_{app}(\omega)$ is the applied magnetic field in which the coil is immersed, and $\mathrm{e}^{i\omega\tau_d}$ represents the signal delay τ_d between the applied field B_{app} and the measuring electronics. In the limits of $\omega\tau \ll 1$ and $\omega\tau_d \ll 1$, the first derivative of imaginary component of (3.13) is

$$\frac{\partial}{\partial\omega}\,\Im\, V_m(\omega) = 2gAN, \tag{3.14}$$

i.e., A may be determined from the slope of the imaginary component of (3.13). τ may be then found by fitting measurements of $V_m(\omega)$ against $B_{app}(\omega)$ in (3.13).

3.1.7. The shortcomings and the limitations of the probe; the sources for error.

The calibration procedure gives rise to one particular set of errors: suppose the absolute error in the measured value of A (the area of a coil) is δA (*i.e.*, $A \to A + \delta A$). From (3.12), the relative error in the inferred value $B_m(t)$ compared to the true value of the applied magnetic field $B_0(t)$ would then be

$$\frac{B_m(t)}{B_0(t)} = 1 + \frac{\delta A}{A}; \tag{3.15}$$

so the error is merely multiplicative on the final result. If the relative error varies by coil, then three-dimensional resolution of a signal's directionality could be affected.

Errors in the value of τ will bias the relative magnitudes of frequency components across the spectrum. Suppose the error on τ is $\delta\tau$ so that $\tau \to \tau + \delta\tau$. Rearranging (3.11), which is already in frequency space,

$$B(\omega) = \frac{V_{m1}(\omega)}{AN} \times \frac{\omega(\tau+\delta\tau) - i}{\omega}; \tag{3.16}$$

and so, adopting the notation of inferred field and true applied field from above, the relative error in frequency space is

$$\frac{B_m(\omega)}{B_0(\omega)} = \frac{\omega(\tau+\delta\tau) - i}{\tau\omega - i}. \tag{3.17}$$

The real part of (3.17) is plotted in Figure 3.6. The central, flat line is the zero-error curve, for reference. Below 10 MHz, even an order-of-magnitude error on τ (dash-dot line) has an effect smaller than ten per cent on the inferred B field. However, between 10 MHz and 100 MHz, the effect of the error rises gradually over the frequency spectrum to about fifty per cent at 100 MHz. The phase is not affected (not shown). If we expect the error in our value of τ to be less than five per cent, then it does not seem to be a big problem.

The probe's physical body perturbs the flow of the plasma. Therefore, if the source of magnetic field signals is embedded in a shock front or flow of matter, the interaction of the probe with the plasma flow can contaminate the results. Care should be taken when interpreting data that possibly include sources very close to the probe.

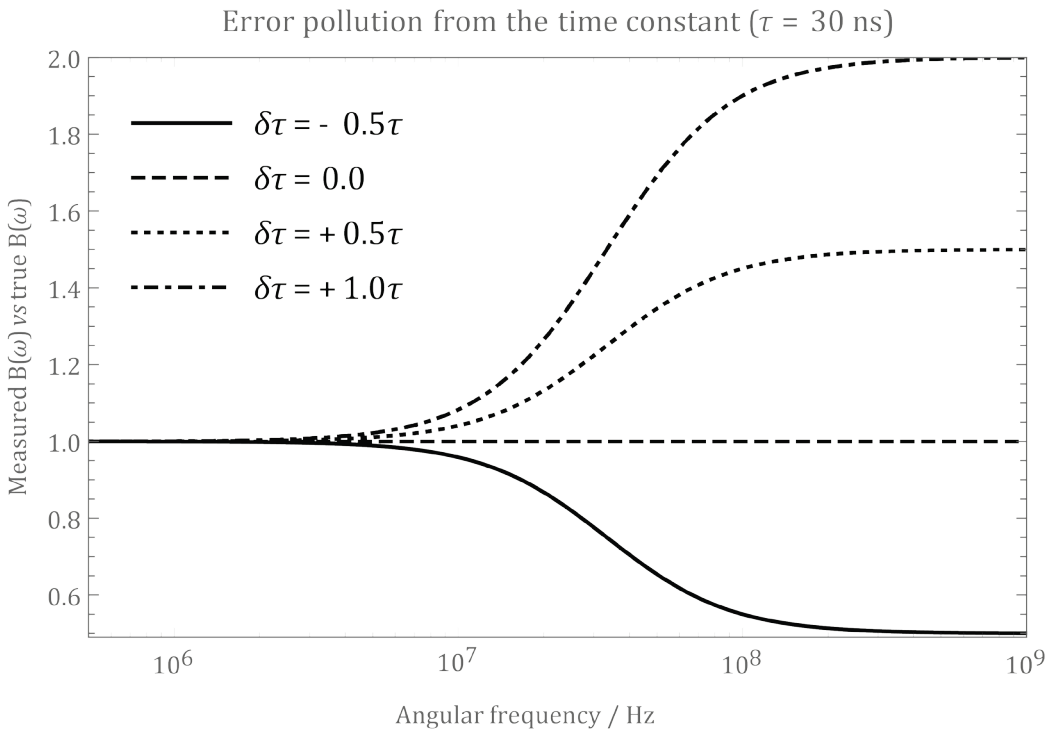

Figure 3.6. The effect of a small error in the probe time constant on the probe's frequency response.

3.1.8. The probe bandwidth, and filtering of the data.

Other reports have suggested that the bandwidth of bdot probes of the design used here is below 100 MHz, with the probe unable to distinguish events occurring faster than about 40 ns (Gregori *et al.*, 2012). During the calibration of the probe, the raw frequency response of the probe is revealed. A graph showing the frequency response in the calibration of this probe by J. Meinecke is given in Figure 3.7; it shows the response function of the probe to a sinusoidal magnetic field produced around the probe by a Helmholtz coil. In the graph, the frequency response is smooth between about 200 kHz and 10 MHz—and the response curve is rising (on the log scale) suggesting a peak sensitivity at about 20 MHz. The curve is no longer smooth but suffers only slight variations until 100 MHz, whereupon it behaves erratically for the remainder of the frequency scale. Although at first blush it might be thought possible to deduce the response function given sufficient resolution on this curve, and so unwind this effect, in all likelihood this behaviour is due to the dominance of nonlinearities, and therefore I treat data above 100 MHz as unreliable.

When computing the total **B** field as function of time, I exclude frequency contributions lower than 300 kHz by applying a high-pass first order Butterworth filter on the data of cut-off frequency 300 kHz.

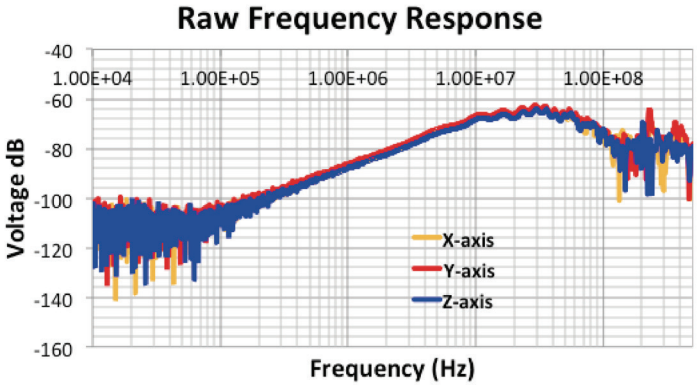

Figure 3.7. The frequency response of the bdot probe to sinusoidal signals (J Meinecke, private communication, 2012).

In the experiments described later, all the bdot probes used were constructed and calibrated by C. Murphy now at the University of York and by J. Meinecke at the University of Oxford. I wish to record my gratitude to those and to G. Gregori for the supply of these probes.

3.2. INTERFEROMETRY AND ELECTRON DENSITY

I use a Nomarski interferometer to make estimates of the electron density profile ahead and behind the laser-produced shocks. Electron density is a key parameter in our experiments; it indicates the existence and the progression of a shock, if any; and it constrains simulations. Interferometry exploits the fact that changes in the plasma permittivity, which principally arise from changes in the local electron density, retard or accelerate the phase velocity of electromagnetic waves passing through it. Comparison with vacuum-propagating reference waves enable the degree of retardation to be measured, and, under certain symmetry assumptions, the electron density to be inferred.

This measurement has a number of advantages, such as the fact that the probe is non-perturbative—it does not affect the plasma through which it propagates—and it may be temporally resolved to accuracy constrained only by the coherency of the probe beam light source, the quality of the intervening optics, and the integration period of the image recording systems. In the present case the measurements achieve a time resolution better than 1 ns. Further, we are able to produce a two-dimensional image rather than a single spatial point measurement. However there are limitations—in particular, that the measurement is not a true 2D slice but an integrated projection of the density along the line of sight of the probe. The mathematics of the inversion also entails assumptions about the symmetry of the plasma, and an assumption that the probe light is not angularly refracted as it passes through the system.

In this section, I show how the interferometer works, I explain how the data can be analysed, and I elucidate some of these limitations. I rely on Huddlestone and Leonard (1965, pp. 431–436), Benattar *et al.* (1979), Ovsyannikov (2000, pp. 59–87, 165–177), Hutchinson (2002, pp. 104–141) and Gregory (2007).

3.2.1. Light waves in plasmas: density and refraction.

The passage of electromagnetic waves propagating through the plasma is affected by the local plasma permittivity; indeed I have already discussed this in part 2.3, in the context of (relatively) low frequency electromagnetic waves, but here I turn my attention to radiation in the optical régime.

In principle, because we have magnetic fields present, a meticulous analysis of this problem requires us to begin from the Appleton–Hartree for the refractive index,

$$N^2 = 1 - \frac{X(1-X)}{1 - X - \frac{1}{2}Y^2 \sin^2\theta \pm \left[\left(\frac{1}{2}Y^2 \sin^2\theta\right)^2 + Y^2(1-X)^2\cos^2\theta\right]^{\frac{1}{2}}}, \tag{3.18}$$

with $N = kc/\omega$ the refractive index, k the wave vector of the radiation, ω the frequency of the radiation, $X = \omega_{pe}^2/\omega^2$, $Y = \omega_{ce}/\omega$, and θ the angle of propagation between the applied **B** field and the wave vector. Indeed, because the plasma deliberated here is non-uniform, were the **B** fields of relevance, it might seem necessary to use a full-wave approach. However, in the cases under immediate consideration, the radiation is in the visible part of the electromagnetic spectrum, and the **B** field is typically of order 100 G. Therefore $Y_{\max} \sim 10^9/\,10^{14} \ll 1$ and I discard quantities arising in the square of Y. In this condition, (3.18) may be simplified a little;

$$N^2 = 1 - \frac{\omega_{pe}^2}{\omega^2} = 1 - \frac{n_e}{n_c}, \tag{3.19}$$

where the *critical density* for light of frequency ω is $n_c = \omega^2 m_e \epsilon_0/e^2$.

From knowledge of the refractive index we may compute the total phase lag between two initially in phase, coherent beams; one passing through the plasma and one through vacuum (or, in the actual experiments, near vacuum), both traversing paths of equal length. The principle is that any change in phase ($\Delta\varphi$) between the two arises because of the plasma, and it may be seen that

$$\begin{aligned}\Delta\varphi &= \int_{\text{path}} (k_{plasma} - k_0)\, dl = \int_{\text{path}} (N-1)\frac{\omega}{c}\, dl \\ &= \frac{\omega}{c}\int_{\text{path}} \left(\sqrt{1 - \frac{n_e}{n_c}} - 1\right) dl,\end{aligned} \tag{3.20}$$

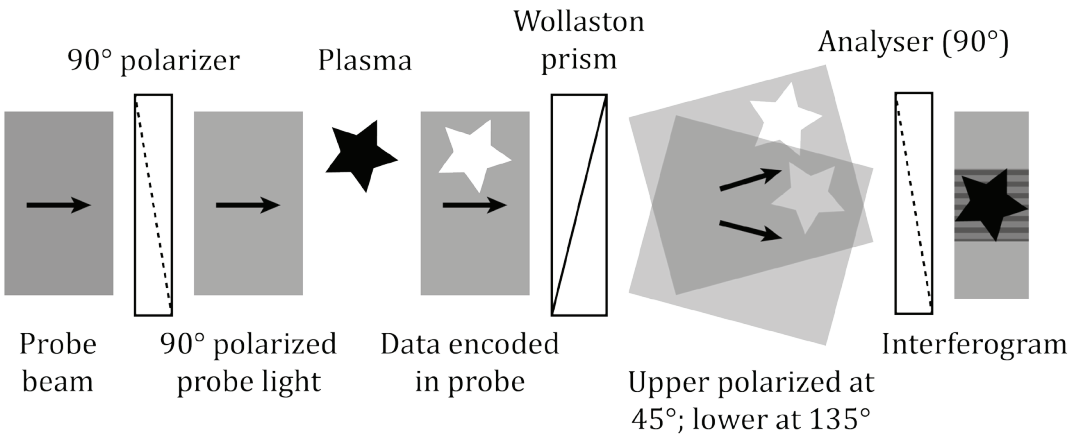

Figure 3.8. The passage of light through a simplified Nomarski-style interferometer.

where in each case the integral is taken over the line of sight from the detector; that is the beam optical path. The goal of the interferometry system is to measure $\Delta\varphi$ so that n_e may be inferred.

3.2.2. The Nomarski interferometer.

A schematic of the Nomarski-style interferometer is given in Figure 3.8. The probe light enters at the left, expanded to the desired sampling cross section and collimated. It passes through a linear polarizer, set here at a nominal orientation of 90°. The beam continues, with the upper half passing through the plasma; the design is such that the lower half evades any plasma. The beam then passes through a Wollaston prism, which splits the beam into two orthogonally polarized components, each propagating at a slight angle to the other (in the diagram this separation is exaggerated). A final polarizer (or 'analyser') interferes the referencing and sampling components together, producing an interferogram, and this may be passed to an imaging system. The key distinction of a Nomarski interferometer is that an undisturbed portion of the beam acts as a phase reference for the sampling component of the beam. This simplifies the design somewhat as it is not necessary to have two sets of optics for two different beam paths.

In order to interfere the reference and the sampling portions of the beam, the Wollaston prism is inserted into the beam path. The prism comprises two birefringent elements cut and glued at an angle, contrived such that two images of mutually orthogonal

polarization are emitted, propagating almost parallel to each other, but for a slightly diverging angle. In this case that separation angle is 1° or 2°. In some Wollaston prisms designed for high-intensity laser light, the elements are not glued.

After further propagation of the two beams at this divergence, not so far that the images have drifted completely apart but rather far enough that the 'top' part of one beam overlaps with the 'bottom' of part of the other, the reference and sampling components are together; and their relatively orthogonal polarizations means that their place of interference can be set by the position of the analyser.

The result is an interference pattern consisting of 'fringes', alternating light and dark regions where construction and destructive interference occurs. If there is no plasma, the optics are arranged such that the phase difference $\Delta\varphi$ is swept from top to bottom, *i.e.*, for image coordinates (x, y), $\Delta\varphi_{\mathrm{ref}}(x, y) \propto y$. Such an image forms a reference; the data image (the one with the plasma) is taken without disturbing the optics. Then the reference fringe pattern is subtracted from the data fringe pattern to find $\Delta\varphi(x, y)$.

3.2.3. The inference of the electron density by Abel's method.

The measurement we make is integrated over the plasma in the line-of-sight of each detector pixel. In this approximation, each line-of-sight is a straight chord passing through the plasma (*i.e.*, the effect of refraction is neglected). The simplest analysis would presuppose the density were constant on this chord; with knowledge of the chord length the density could be found; this seems quite unreasonable a supposition to hold. Instead we proceed with the assumption that the plasma exhibits cylindrical symmetry (a condition fulfilled in approximation), so that we may apply the method of Niels Henrik Abel[2] to transform from the integrated measurement of phase to the local electron density, as a function of the plasma radius.

The Abel 'forward' transform is shown in Figure 3.9. The figure shows a slice through the y-axis of a cylindrically symmetric density function f. Darker grey corresponds to

[2] A common hazard of being a brilliant mathematician is the propensity to die young: Abel died at the age of twenty-six. One of his final submissions was entitled 'a general solution for the integration of all differential formulas'; unfortunately it was lost by a reviewer and has never been found.

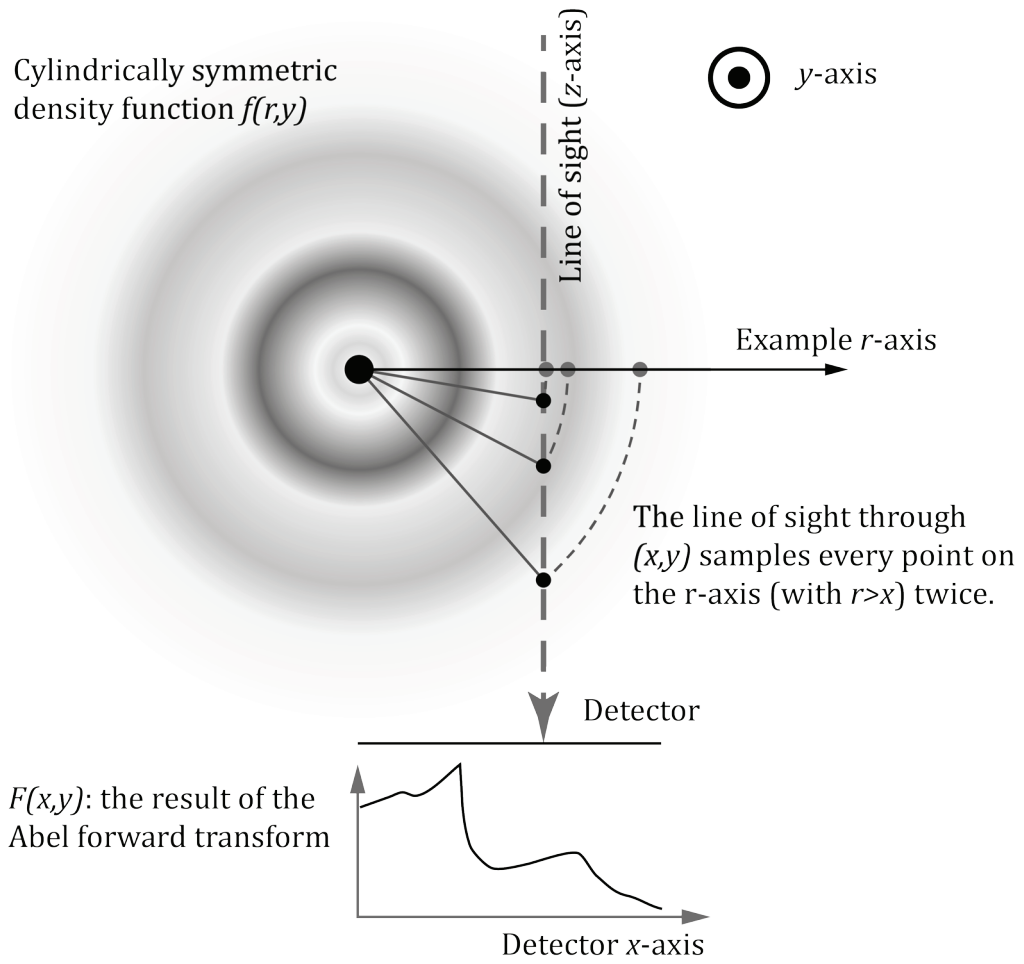

Figure 3.9. The Abel forward transform of a cylindrically symmetric function onto a plane.

greater density. A line of sight is shown as a straight, dotted grey line through the distribution, landing on the detector. The detector and the line of sight are orthogonal. Note that, if the line has its closest-approach to the centre of the distribution at radius x, then the line samples every point $f(r > x, y)$ twice.

From Figure 3.9, we see that the detector will measure $f(r, y)$ by integrating over the line z. Let us label the measurement of f at the detector as $F(x, y)$. The forward Abel transform is therefore

$$F(x,y) = \int_{-\infty}^{\infty} f\left\{\sqrt{x^2 + z^2}, y\right\} dz. \tag{3.21}$$

where x and z are measured from the cylinder origin and y is the cylinder height out of the page. The derivation is independent of y in the sense that each slice through the

cylinder is, in principle, independent of the other slices. (3.21) may be re-cast so that it is not an explicit function of z (after all, z is not known to the observer at the detector):

$$F(x,y) = 2\int_x^\infty \frac{r\,dr}{\sqrt{r^2-x^2}} f(r,y). \tag{3.22}$$

This is the explicit form of the path integral required in (3.20), and it agrees with our reasoning that $F(x,y)$ should sample every $f(x>r,y)$ twice. What we actually require though is the reverse transform—the forward transform is performed automatically when we observe the cylinder side-on, and we wish to unwind that effect. The Abel reverse transform is obtained less straightforwardly but it may be verified by substitution into the forward transform (3.22):

$$f(r,y) = -\frac{1}{\pi}\int_r^\infty dx\,\frac{dF(x,y)}{dx}\frac{1}{\sqrt{x^2-r^2}}. \tag{3.23}$$

With choices of f and F appropriate for electron density measurements with light rays,

$$f = \sqrt{1-\frac{n_e}{n_c}} - 1 \quad \text{and} \quad F = \left(\frac{c}{\omega}\right)\Delta\varphi,$$

we obtain

$$\sqrt{1-\frac{n_e}{n_c}} - 1 = -\frac{1}{\pi}\int_r^{r_0} \frac{dx}{\sqrt{x^2-r^2}}\frac{d}{dx}\left\{\frac{c}{\omega}\Delta\varphi(x,y)\right\}. \tag{3.24}$$

r_0 is the maximum radius of the plasma; it being understood that $F(x>r_0)=0$, and consequently the contribution to the integral outside r_0 vanishes. Usually we will find that $n_e \ll n_c$, in which case the expression may be simplified a little,

$$n_e(r,y) = -\frac{2cn_c}{\pi\omega}\int_r^{r_0} \frac{dx}{\sqrt{x^2-r^2}}\frac{d}{dx}\{\Delta\varphi(x,y)\}. \tag{3.25}$$

The integration is undertaken numerically by converting the integral to a sum over discrete coordinates in x: the coordinates coinciding with pixel grid of the detector.

3.2.4. Limitations of interferometry.

As we have seen, the interferometric system in effect performs an integration over the line of sight from each detector pixel to the probe source. Therefore, the image we obtain at the detector is not a true cross section of the plasma. Lacking depth information, in analysing the dataset it is necessary to make an assumption about the plasma configuration along that axis. The Abel inversion presumes that the dataset is

axially symmetric; if the data are not symmetric then the inversion acts as a kind of averaging to produce an axisymmetric plot.

Density gradients in the plasma will cause refractive effects, bending the rays of light passing through the plasma. Refraction is a difficult problem for which to compensate, because it often results in 'split' fringes—where a fringe abruptly begins or ends.

That the picture consists of spatially oscillating light and dark fringes limits the spatial resolution of the diagnostic. To avoid ambiguity, it is not sufficient to allocate merely one row of pixels to a dark fringe and the subsequent row to a light fringe, at least three or four rows will be required. This constrains the spatial resolution of the image to the corresponding fraction of the detector's spatial resolution.

The imaging system and probe laser together set a limit on the temporal width of successive diagnostic images. That is to say, even with multiple cameras or a multiple-frame camera, it is not possible to obtain images spaced apart further than the temporal width of the probe, which is often of only a few nanoseconds. For a microsecond-long experiment, this is a serious constraint, and requires multiple laser shots to create a (pseudo) time history of the electron density profile. (This is not quite a time history, because there is no guarantee that each shot is identical to the previous one.) A potential solution to this is to use an array of mirrors, lenses and beam splitters to build a 'pulse stacker' (Börner *et al.*, 2012), but for a microsecond beam this kind of set up is not very practical.

These caveats aside, interferometry is a simple and largely reliable way to obtain estimates of electron density.

3.3. TIME-INTEGRATED ELECTRON SPECTROSCOPY

As the drive laser comes to focus, the action of collisional damping on the light wave within the plasma, as well as the presence of extreme electric fields in the light wave cause the acceleration of electrons to high velocity. These electrons rapidly escape the focal region, but their effects may become important: as discussed in section 2.3.4, streaming hot electrons can excite waves in the plasma medium through which they

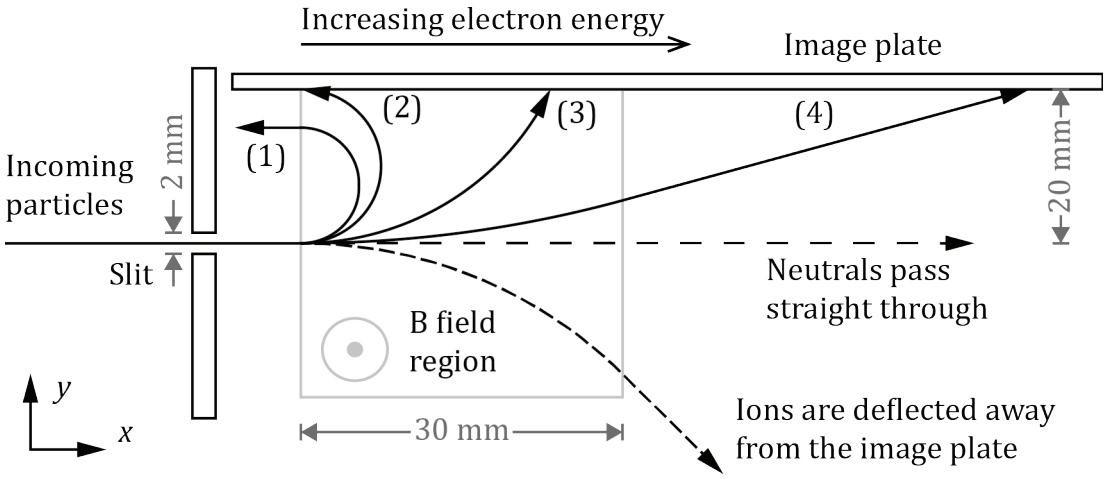

Figure 3.10. A schematic showing the design and principle of the electron spectrometer.

propagate. In order to understand this phenomenon in relation to that of the hot, shock-produced electrons, I characterized the typical energy values of laser-accelerated electrons with the use of an electron spectrometer.

3.3.1. The principle and the design of the electron spectrometer.

Magnetic fields curve the trajectories of charged particles, without doing work upon the particles: this straightforward principle is the essence of the diagnostic. The design is shown in Figure 3.10. The spectrometer is positioned approximately 300 mm from the target, so incoming particles may be assumed to be collinear. Care is taken to ensure the image plate is parallel with the initial trajectory of the particles on their passage from the target. Electrons (and other particles) are admitted through a thin slit, in this case of 2 mm height. These particles encounter a magnetic field, whose lines are arranged to be parallel with the slit and perpendicular to the particles' trajectories. The magnetic field acts to deflect negatively charged particles—and I assume that only electrons are present in that configuration—upwards, into an imaging plate, which records the terminal position of the impacting electrons. The permanent magnet, whose active part is the neodymium-iron-boron alloy, is placed in a yoke. The yoke restricts the spatial leakage of the field; and I model the field as uniform between the poles, vanishing outside this

region. (That this is not really the case is an important contributor to the error on my modelling of the diagnostic.)

For an electron, of fixed rest mass and charge, the degree of deflection is a consequence of its momentum alone; slower electrons [following trajectories (1), (2), or (3)] are deflected more readily than very fast electrons [trajectory (4)], which pass straight through the **B** field, experiencing little influence on their paths. Meanwhile, positively charged particles such as ions will be deflected in the opposite direction, and neutrals such as photons will not be affected at all. Under the presumption that electrons are the only negatively charged bodies present, we may in this manner separate the electron component for examination, and from the degree of deflection infer the initial speed. Trajectory (1) indicates that there is a minimum energy threshold before the diagnostic will detect the electron.

The slit and the system geometry constrain particles to enter the electron spectrometer with momentum directed only parallel to the plate, at velocity v. The Lorentz force acting on a generic charged particle is $\mathbf{F} = q(\mathbf{E} + \mathbf{v} \wedge \mathbf{B})$, from which (in the absence of **E**) the electron equation of motion is

$$m_e \ddot{x} = -e\dot{y}B \quad \text{and} \quad m_e \ddot{y} = -e\dot{x}B, \tag{3.26}$$

where the diacritical dots signify differentiation with time. We also have the constraint imposed by the terminal impact on the plate, *i.e.*,

$$\int_0^\tau \dot{y}\, dt = y \quad \text{and} \quad \int_0^\tau \dot{x}\, dt = x, \tag{3.27}$$

where x is the terminal distance of the particle along the plate at the terminal time τ, and y is the height of the plate above the slit. The final restriction is that, because the magnetic force is always directed perpendicular to the electron's motion, no work is done upon the electron by the force and so, at all times prior to impact, $\dot{x}^2 + \dot{y}^2 = v^2$. Together these qualifications specify the kinetic energy $\mathcal{E}$ of the electron, which is

$$\mathcal{E}(x) = \frac{e^2 B^2}{8y^2 m_e}(x^2 + y^2)^2. \tag{3.28}$$

It is seen that $\mathcal{E} \sim x^4$, making the diagnostic sensitive over a wide range of energies (in this design 36 keV to about 150 keV), but also liable to error because of the high exponent.

This derivation follows from the principle that the electrons travel within the magnetic field region, which is at uniform strength. If they pass out the other side [*e.g.*, following trajectory (4)], or if there is 'leakage' outside the uniform, ideal region, then the calculation must be modified; in the latter case probably to the point of becoming non-analytic. With knowledge of the field geometry, it would be possible to model this by sending a series of test particles of varying energy through the magnetic field of varying magnitude, terminating on the plate, to build a look up table, but I have not undertaken this.

3.3.2. The sensitivity and the dynamic range of the imaging plates.

The imaging plates are commercial products supplied by Fujifilm. I used the BAS-SR type, which consists of a 112 μm active layer protected by an 8 μm coating of Mylar plastic ($C_{10}H_8O_4$). The structure is completed by adherence to a supporting back and finally a convenient weakly magnetized strip on the rear surface. The active layer consists of photo-stimulable phosphor crystals ($BaFBr:Eu^{2+}$) in an organic binder. The introduction of ionizing radiation frees an electron from the Eu^{2+} ion, whereupon it is free to migrate to a nearby 'F centre' or *farbe* centre[3] (an anomalous missing anion in the crystalline structure), which acts as a metastable trap for the electron. Irradiance with visible light is sufficient to liberate the trapped electron where it may recombine with the now Eu^{3+} ion; it does so with a characteristic photoluminescence of 390 nm. It is this photoluminescence that is detected during the imaging plate reading process (Chen *et al.*, 2008; Fiksel *et al.*, 2012; Zhong *et al.*, 2005).

While it is unnecessary to obtain an absolute calibration of the image plates for the purpose of spectrum extraction, the sensitivity of the active layer does vary slightly with the deposition kinetic energy of the recorded electron. It must be admitted immediately that there is not an abundance of material examining the sensitivity of imaging plates to electrons in the 35–150 keV range, but two papers between each other cover either end of the range adequately and their estimates are mutually consistent across the middle,

[3] From the German word for 'colour'. Crystals furnished with this particular lattice defect often have a vibrant colour about them, for the energy associated with an electron escaping a *farbe* centre and recombining with a hole corresponds to that of a visible photon.

unexplored ground (50–100 keV) (Busold *et al.*, 2014; Zhong *et al.*, 2005). I use

$$\Sigma\mathcal{E}(x) = \left(5.2 \times 10^{-6}\ \frac{\text{PSL}}{\text{eV}} \times \mathcal{E}(x) - 0.0024\ \text{PSL}\right)^{-1} \times S(x) \tag{3.29}$$

(adapted from both papers), where $S(x)$ is the measured photostimulated luminescence at position x and $\Sigma\mathcal{E}(x)$ is the total electron energy there delivered in eV, and the characteristic energy $\mathcal{E}(x)$ of an individual electron at position x on the plate as given in (3.28). From this the number of electrons c at that position and therefore with that energy is

$$c(x) = \frac{\Sigma\mathcal{E}(x)}{\mathcal{E}(x)}. \tag{3.30}$$

(3.29) did not include the effect of the protective Mylar coating for electrons below 50 keV. However, at eight microns the coating is sufficiently thin that it is far thinner than the penetration depth of 50 keV elections (approximately 30 microns, according to the NIST database). Therefore, I disregard this effect.

3.3.3. The resistance of the interposed gas to the travelling electrons.

In the experiment, the electrons do not pass through a vacuum on their path to the detector, but rather a gas is present to facilitate the shock. Therefore the electron energy might be altered by its the passage through the argon gas, principally through scattering.

I used the NIST database to obtain estimates of the stopping power of argon for each electron energy value within an appropriate range, and then used a simple model to calculate the original energy given a final energy, passage distance and pressure. The correction was in no case greater than a few per cent. The assumption is that the gas is not ionized in bulk at the very early time during which the laser is active.

3.3.4. Sources of error, and limitations.

The principle causes for error are imprecision in the 'zero' position of the magnetic field, and leakage of the field beyond the yoke-constrained region. By the zero position, I really mean the position at which the lowest energy electrons can be detected, which is, according to this theory, 36 keV. Estimates of the zero position are made by the clear dark shadow presented by the magnets on the imaging plate. The fringe field is probably

the more serious concern, because it has not been quantified here at all. The best solution I can see would be to calibrate directly the spectrometer with a controllable electron source.

The measurement is also a time-integrated one, which means that it is impossible to separate the hot, laser-produced spectrum from other processes occurring at later time. This is a significant shortcoming of our spectrometer. The device must also be carefully aligned such that the image plate is parallel to the incident electron trajectory, but the initial electrons may well be deflected by strong magnetic fields near the laser-matter interaction point.

The spectrum only goes down to 36 keV, which is not sufficiently low for the data I am interested in. This could be easily resolved with a weaker bending magnet, but the concerns about the Mylar coating's stopping power might become relevant.

3.4. SUMMARY OF THE INSTRUMENTATION CHAPTER

I have discussed three instruments of particular relevance to this thesis; the bdot probe, the Nomarski interferometer and the electron spectrometer. Each has its uses and in particular the bdot probe provides important data for the results discussed later, and the electron interferometry will constrain important computer simulations; but all have some shortcomings. These limitations must be borne in mind when interpreting the data produced by each instrument, for each can supply misleading data.

4. SIGNAL ANALYSIS TECHNIQUES

The data extracted bdot probes are in the most part noisy and transient. To maximize the usefulness of the dataset and to improve the foundation of the principle results herein presented, I have found it useful to invoke certain techniques from signal analysis.

The typical or default representation of a signal—for instance the plot of the detected magnetic field magnitude against time—does not always show clearly all of the information embedded within the signal; and moreover the representation may not even show the most important information in a way that is readily digestible. Therefore an alternative representation of the same information may be more useful to the experimenter.

The most familiar signal analysis technique is the Fourier analysis, and this Chapter will include a brief summary of its results; but it will be seen that for transient signals the Fourier transform is a poor representation to choose. I look at the windowed Fourier transform and the wavelet transform, each being more suited to the analysis of signals displaying transient character; and I examine the use of coherency analysis in demonstrating the correlation of two signals that cannot *a priori* be determined to be related.

4.1. MATHEMATICAL PRELIMINARIES

It not my intention to introduce more mathematical machinery than is necessary for obtaining a physical intuition of the techniques under review in this Chapter. Consequently, I eschew a great part of the usual mathematical baggage that attends an introduction to wavelet theory. Nonetheless, it is easier to introduce those required

definitions, notations and results first, rather than repeatedly interrupt the discussion of the Chapter to draw them out. (Less optimistically, at least these preliminaries are at least in one place for ease of later reference.)

Definition 1. Absolutely integrable functions ($\mathbf{L^1}(\mathbb{R})$ functions).

Suppose we have a function $f : \mathbb{R} \to \mathbb{C}$ (that is, f is defined over the real numbers and the result it returns are complex [or, possibly real, since a real number is also a complex one]). Then f is said to be *absolutely integrable* if

$$\int_{-\infty}^{+\infty} |f(t)|\, dt < +\infty \tag{4.1}$$

(in the sense that the integral exists and has a finite value). The set of all absolutely integrable functions, where they are defined on the real line, is $\mathbf{L^1}(\mathbb{R})$; therefore, for shorthand, where f satisfies this definition, we may write $f \in \mathbf{L^1}(\mathbb{R})$.

Definition 2. Square-integrable functions ($\mathbf{L^2}(\mathbb{R})$ functions).

A function $f : \mathbb{R} \to \mathbb{C}$ is *square-integrable* if

$$\int_{-\infty}^{+\infty} |f(t)|^2\, dt < +\infty. \tag{4.2}$$

Some authors would say that f has *finite energy*. The set of all square-integrable functions on $\mathbb{R}$ is called $\mathbf{L^2}(\mathbb{R})$.

Definition 3. The inner product $\langle \cdot, \cdot \rangle$.

For two functions $f, g \in \mathbf{L^2}(\mathbb{R})$, the *inner product* of f and g is denoted $\langle f, g \rangle$ and is defined

$$\langle f, g \rangle = \int_{-\infty}^{+\infty} f(t)\, g^*(t)\, dt, \tag{4.3}$$

where g^* is the complex conjugate of g. Unfortunately, this bracket notation for two functions $\langle f, g \rangle$ could easily be confused with the taking of an expectation value $\langle x \rangle$ for a single variable, but I have still found it clearer than using other notations.

Definition 4. The norm in $\mathbf{L^2}(\mathbb{R})$.

A norm is a measure of the "size" of an object; for instance the absolute value or modulus function $|x|$ is an example of a norm for $x \in \mathbb{R}$. The *norm* I shall use for functions in $\mathbf{L^2}(\mathbb{R})$, written for $f \in \mathbf{L^2}(\mathbb{R})$ as $\|f\|$, is

$$\|f\| = \sqrt{\langle f, f \rangle} = \sqrt{\int_{-\infty}^{+\infty} |f(t)|^2 \, dt}. \tag{4.4}$$

Definition 5. The support of a function and the meaning of compact support.

The *support* of a function $f : \mathbb{R} \to \mathbb{C}$ is the set of all the points x where $f(x) \neq 0$. f is said to have *compact support* if $f(x)$ is zero everywhere except for x within some finite range.

The Cauchy–Schwarz theorem on $\mathbf{L^2}$.

For all $f, g \in \mathbf{L}^2$,

$$|\langle f, g \rangle|^2 \leq \|f\| \, \|g\|. \tag{4.5}$$

The Parseval theorem.

Suppose $f \in \mathbf{L^2}$ and the Fourier transform of f exists and is denoted $\tilde{f}$. (The Fourier transform is defined later in (4.7).) Then

$$\|f\| = \left\|\tilde{f}\right\| \tag{4.6}$$

(Baher, 1990). Loosely speaking, this is a statement saying that the Fourier transform preserves the 'total size' or the 'total energy' of the function on which it operates.

4.2. FOURIER ANALYSIS

The most straightforward technique in signal analysis is the continuous Fourier transform, first introduced by Jean-Baptiste Joseph Fourier in his work *Théorie analytique de la chaleur* (1822)[4]. Fourier argued that any periodic function, even those possessing discontinuities, could be represented as the limit of the infinite sum of trigonometric functions: a position that Pierre-Simon Laplace felt to be 'contrary to the rules of calculus' (Herivel, 1975). The transformation was first used in solving differential equations, such as the Heat Equation discussed in Fourier's *Théorie*; but its property of reorganizing time-series measurements by frequency formed the basis of early signal analysis.

As I have alluded, among the more salient objections raised against *Théorie* was Fourier's claim that even discontinuous functions could be represented by the sum of continuous trigonometric functions. Indeed, it would require another century of mathematical development before the limits and conditions of Fourier's claim could be understood. Even with the mathematical details now tidy, in the practical use it requires both the assumption of periodicity and components of arbitrarily high frequencies. Therefore Laplace's early objection concerns us as well; but because Fourier transforms are a simplified case of the other transforms we will discuss, I begin by reviewing in synopsis the mathematical technique of the Fourier transform, in its application to signal processing.

4.2.1. The Fourier transform.

Both the computation and the analysis of the signals made were done on discrete datasets with discrete transforms. However, the mathematical analysis of the continuous Fourier transform is more straightforward, so I begin there before looking at how it is adapted for discrete purposes.

---

[4] In fact, Fourier had first attempted to publish his work on the eponymous series in 1807, but his manuscripts were repeatedly rejected by referees, allegedly for lacking both generality and rigour. See Herivel (1975) for an interesting history.

The Fourier transform.

Let us suppose that we have an instrument that provides a measurement of some physical quantity as a function of time. We label these measurements $f(t)$. Suppose further that f is absolutely integrable [in the sense given in (4.1)]. Then the continuous Fourier transform of $f(t)$ is

$$\tilde{f}(\omega) = \int_{-\infty}^{+\infty} f(t) e^{-i\omega t}\, dt, \tag{4.7}$$

where ω is the angular frequency. (Mallat, 1998.)

In effect, the Fourier transform of $f(t)$ at ω filters $f(t)$ through the function $\mathrm{e}^{-i\omega t}$. If f has a component of frequency ω, then the sum at ω will become large. This property—that the transform decomposes $f(t)$ into a sum of frequencies—becomes clearer in the inverse transform.

The representation of a noisy composite signal in Fourier space often enables the straightforward identification and characterization of the periodic features. See Figure 4.1 for a synthetic example: the application of the Fourier transform enables one to see distinctly the frequency elements composing this dataset. The dataset on the left is impossible to interpret, not least because of the presence of Gaussian white noise; on the right hand side the graph's power spectral density (the square of its Fourier transform) shows immediately it comprises only three distinct frequency components at 47, 67 and 80, overlaid with noise.

The inverse Fourier transform.

The inverse Fourier transform of $\tilde{f}(\omega)$ is given by

$$f(t) = \frac{1}{2\pi} \int_{-\infty}^{+\infty} \tilde{f}(\omega) e^{i\omega t}\, dt. \tag{4.8}$$

The original signal $f(t)$ may therefore be expressed as the sum of the frequency amplitudes $\tilde{f}(\omega)$, each multiplied by the exponential function. $\tilde{f}(\omega)$ is complex; the imaginary part represents the phase offset, that is, the initial phase.

The circular functions, as expressed in the exponential, have a number of properties that make them useful for time-invariant analysis. In particular they are linear operators; complex exponentials are eigenvectors of linear time-independent systems, therefore the

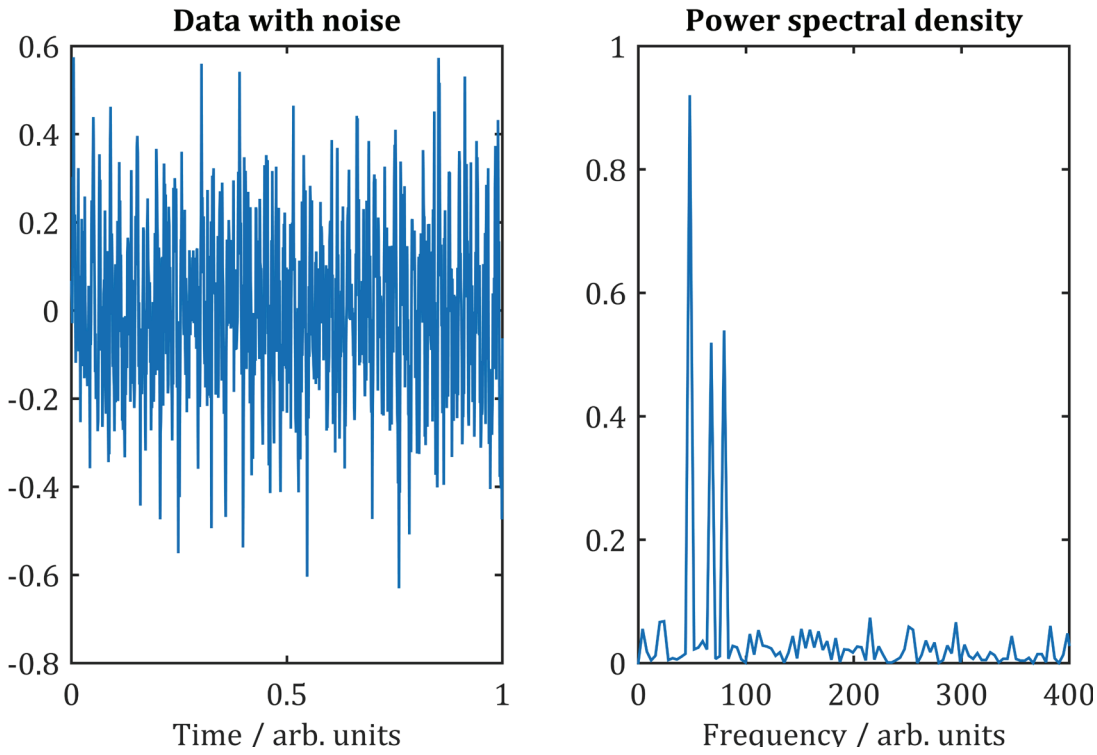

Figure 4.1. Synthetic noisy data in the time and in the frequency domains.

Fourier transform is merely a decomposition of the system into a sum of eigenvectors. However, when a system is not time-independent, it is clear that other functions could be a better choice, in place of the $\{e^{-i\omega t}\}$. (Mallat, 1998.)

4.2.2. The energy and power of a signal; and its energy and power spectral densities.

Although the Fourier transform of f gives us a Fourier spectrum $\tilde{f}$, it is more common in practical application to interpret $\tilde{f}^2$ instead of $\tilde{f}$. For a signal f, the *signal energy* is defined as

$$W = \int_{-\infty}^{+\infty} |f(t)|^2 \, dt \tag{4.9}$$

(provided the integral converges), and by Parseval's theorem (4.6), this is the same energy as contained in the Fourier transform of f;

$$W = \int_{-\infty}^{+\infty} \left|\tilde{f}(\omega)\right|^2 d\omega. \tag{4.10}$$

The area under $\left|\tilde{f}(\omega)\right|^2$ is the total energy of the signal; therefore, a plot of $\left|\tilde{f}(\omega)\right|^2$ against ω gives the *energy spectral density* (ESD), that is, the energy per unit frequency. In physical applications, W normally has some simple multiplicative relation to physical energy; but it is not always the case so care must be taken with using the expression. (Stremler, 1990.)

If the signal is not of finite energy, we may turn instead to the representation of the signal power. Suppose that f is periodic with some period T. Then the *power spectral density* (PSD or power spectrum) is

$$P(f) = \frac{1}{T}\left|\widetilde{f_T}(\omega)\right|^2 \tag{4.11}$$

where the truncated Fourier transform of f over the period T is

$$\widetilde{f_T}(\omega) = \int_0^T f(t)e^{-i\omega t}\, dt. \tag{4.12}$$

Again, the signal power may not be physical power, but the relation is not usually distant.

4.2.3. The Fourier uncertainty theorem.

Regrettably it is not possible to give an arbitrarily precise measure of both the frequency components and the temporal range occupied by a signal: this is a fundamental property of signals, and not a limitation of the mathematical tools used to analyse them (Mallat, 1998). Some authors refer to this relationship as the 'uncertainty principle', because it is mathematically analogous to the Heisenberg uncertainty principle in quantum mechanics. Unlike, however, the minimum joint-uncertainty in the momentum and position measurements of a particle, the fact that a relationship arises between the reciprocal parameters of time and frequency is not altogether surprising.

The mean and standard deviation of a signal.

Let $f \in \mathbf{L^2}$ and suppose f is normalized (*i.e.*, $\|f\| = 1$). For a finite energy signal, this assumption can be done without loss of generality under a straightforward re-scaling. Then the *mean value* of t is

$$m_t = \int_{-\infty}^{+\infty} t|f(t)|^2\, dt, \tag{4.13}$$

and the *standard deviation* of t about this mean is

$$\sigma_t = \sqrt{\int_{-\infty}^{+\infty} (t - m_t)^2 |f(t)|^2\, dt}; \tag{4.14}$$

m_t and σ_t are real-valued. Similar definitions can be made for the mean frequency and standard deviation of ω when $f(t)$ is Fourier-transformed into $\tilde{f}(\omega)$:

$$m_\omega = \int_{-\infty}^{+\infty} \omega \left|\tilde{f}(\omega)\right|^2 d\omega; \tag{4.15}$$

$$\sigma_\omega = \sqrt{\int_{-\infty}^{+\infty} (\omega - m_\omega)^2 \left|\tilde{f}(\omega)\right|^2 d\omega}; \tag{4.16}$$

and these quantities are also real-valued. (Mallat, 1998.)

The Fourier uncertainty theorem.

Let $f \in \mathbf{L^2}$ and suppose f is normalized (*i.e.*, $\|f\| = 1$). For every Fourier transform pair f and $\tilde{f}$,

$$\sigma_t \sigma_\omega \geq \frac{1}{2}. \tag{4.17}$$

In other words, a function cannot be arbitrarily confined in time and be at the same time confined in frequency space. I provide a proof of this fact in the Appendix.

4.2.4. Discrete and finite Fourier transforms.

In dealing with recorded data instead of abstract mathematical functions we necessarily turn to the discrete transform. Although the real physical function underlying the measurement is (probably) continuous, the recorded data are in the one-dimensional case only a set of coordinates, of the form $\left(t_j, x_j\right)$, for $j = 0, \ldots, N-1$; and the coordinates in the finite, discrete subspace of the rational numbers $\mathbb{Q}_T \times \mathbb{Q}_X$. This rather curbs the power of our mathematical machinery, as the low density of numbers in this space means even the processes of taking limits and performing integrals are not mathematically robust.

An easy solution to the problem is to create a 'normal' continuous function $f \in \mathbf{L^2}$ which can be Fourier-transformed, but which is 'pegged' to the measurements in the sense that the values at each of the $\{t_j\}$ are $f(t_j) = x_j$. The downside is that with only a finite number of points (t_j, x_j) on which to constrain our function (or even with only a countably infinite number of points), there is an infinite number of different ways of filling in the gaps between them, even in a smooth, continuous way. When imposing a constraint on the behaviour of f—for instance to say it does not oscillate wildly between measurements—we are essentially making an assumption either about the measurement device or the physical behaviour of the system. For instance, if probing a magnetic field with a bdot probe, we might be effectively assuming that high frequency waves are not present. We can either accept aliasing (the appearance of spurious frequency components reflected from above the sampling frequency) or impose an anti-aliasing filter to eliminate them, which also attenuates tones near the sampling frequency. (Mallat, 1998.)

The second problem with 'real-world' signals is that they are of finite duration; but the Fourier transform inherently deals with periodic data (because the basis functions are periodic). Supposing the signal is N elements long, the x_0 and the x_{N-1} components can be wrapped, appearing side-by-side so that the signal is effectively repeated. This may produce high frequency artefacts, particularly if $x_0 \nsim x_{N-1}$. Further, if the signal x is of limited duration, an extension of the Fourier uncertainty theorem proves that the signal cannot also be band-limited; that is to say, $\tilde{x}$ does not have compact support. (Mallat, 1998.)

The discrete Fourier transform.

Given a collection of N data points, in the form (t_j, x_j), with $j = 0, \ldots, N-1$, the transformed points are $\tilde{x}_k$ are given by the *analysis equation*

$$\tilde{x}_k = \frac{1}{N} \sum_{j=0}^{N-1} x_j e^{-ikj/N}. \tag{4.18}$$

The reverse transform (the *synthesis equation*) may be expressed

$$x_j = \frac{1}{2\pi} \sum_{k=0}^{N-1} \tilde{x}_k e^{ikj/N}. \tag{4.19}$$

However the computation in this manner is quite inefficient; instead a variant of the fast Fourier transform is usually preferred.[5]

4.2.5. On the difficulties of representing transient events.

The basis functions ($\{e^{-i\omega t}\}$) of the Fourier transform are ill suited to detect and emphasize transient, short-lived events, principally because they are periodic across the entirety of time; the circular functions are not localized. Therefore, the representation cannot show the temporal position at which a component of the signal appears or changes: variations in the amplitude of a frequency component are effectively averaged over the sample time. For dynamic physical processes that are not time-invariant, this makes Fourier transforms quite unsuitable.

4.2.6. Examples of real data.

In Figure 4.2 I show the processed B-dot data to show the magnetic field history with time from one experiment. (See Part 5.1 for the full experiment details.) At $t = 0$ the graph is dominated by the noise from the laser pulse. In Figure 4.3 the power spectrum of the graph can be seen. It is quite difficult to interpret because the spectrum is actually dominated by this early-time noise. Therefore, a robust process to filter out this noise, by temporal windowing of the data, would be useful.

[5] The fast Fourier transform was first published by Cooley and Tukey in 1965, and essentially involves exploiting the properties of the exponential function to rewrite the equations under a scheme requiring less arithmetic. Unbeknownst to them, the key part of the algorithm had been in fact been quietly invented by Carl Frederic Gauss in 1805, but remained unpublished until his death, and then little discussed until its later re-invention. Gauss first used the method to simplify the arithmetic labour of fitting a sixth order polynomial to astronomical observations.

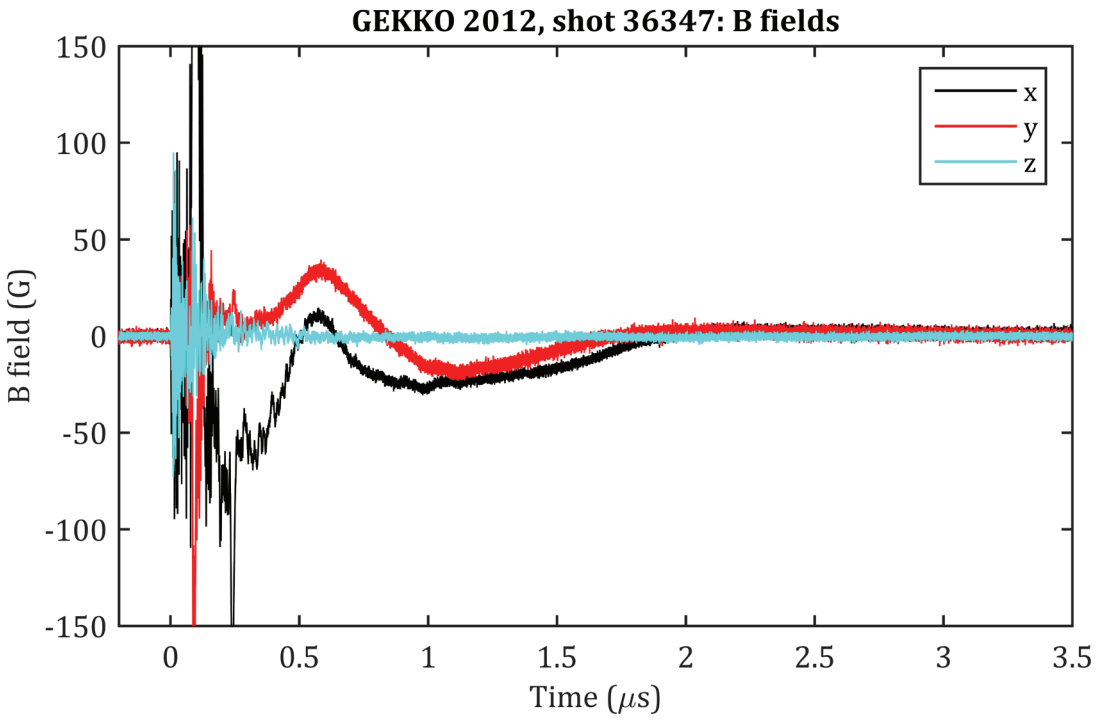

Figure 4.2. Magnet field data processed from a bdot probe.

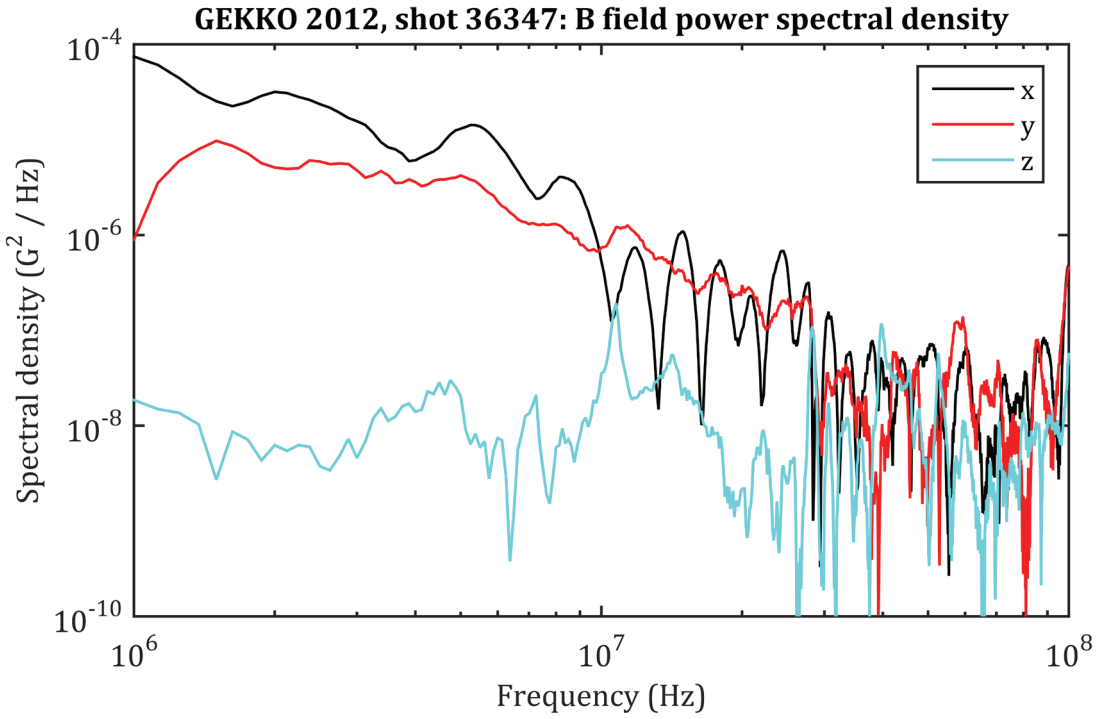

Figure 4.3. Power spectrum of the magnet field data given above.

4.3. THE WINDOWED FOURIER TRANSFORM

Perhaps the most obvious remedy for the lack of transient detection is the windowed Fourier transform, also sometimes called the short time Fourier transform ('STFT'). In this process we localize the circular functions by passing them through a simple 'window' function, which acts to attenuate the exponential functions outside the window. The attenuated function can then be slid along the time axis to show the evolution of the signal; or alternatively it can be used to window-out an undesired transient feature at the beginning or end of the measurement, for instance the presence of noise from the laser-matter interaction.

The windowed Fourier transform.

Let $g(t)$ be a symmetric, real-valued function. I shall call g the window function. Further, define $g_{u,\omega}$;

$$g_{u,\omega}(t) = Ag(t-u)e^{i\omega t}, \tag{4.20}$$

where A is a normalizing constant such that $\|g_{u,\omega}\| = 1$. Here, u represents a translation of g along the temporal axis and ω is a modulation in frequency space.

For a signal $f \in \mathbf{L^2}(\mathbb{R})$, the windowed Fourier transform of f at (u, ω) is the inner product of f with the window $g_{u,\omega}$.

$$\langle f, g_{u,\omega} \rangle = \int_{-\infty}^{+\infty} f(t)\, Ag(t-u)e^{-i\omega t}\, dt \tag{4.21}$$

In this way, the Fourier transform has been "windowed" or localized about the temporal point u. (Mallat, 1998.)

4.3.1. Windowing to exclude early phenomena.

Where a measurement contains transient phenomena only at the beginning or end of the measuring time period, or if a feature of interest is suspected *a priori* to exist in a certain region on the time axis, then a windowing function can be used to exclude or select the data of interest before a regular Fourier transform is applied to the windowed data.

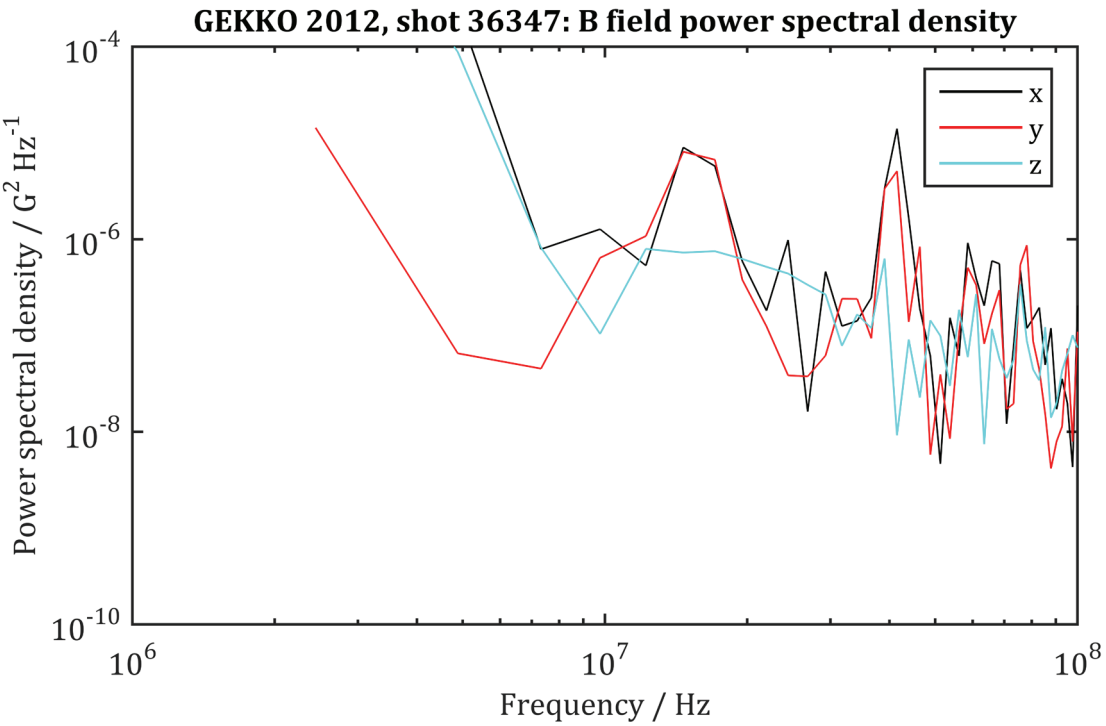

Figure 4.4. Partial power spectrum of bdot data windowed on 500–800 ns reveals more peaks.

In Figure 4.4 I include a windowed transform of the data presented in Figure 4.2. The data have been windowed to be included only between 500 ns and 800 ns; without the early time components, the graph behaves quite differently to Figure 4.3. A peak in the x- and y-axes is clearly visible at about 10–20 MHz, and again at about 40 MHz. No such behaviour is seen on the z-axis.

4.3.2. Multiple windowed transforms in one graph.

I present an artificial example: consider a 600 Hz constant tone superimposed on a 'chirp'; that is a tone of gradually increasing frequency, beginning at 200 Hz and rising in frequency uniformly over the time of 1 second to a pitch of 2 kHz.

The raw graph of this, in temporal space, is an uninterpretable mess (not shown); the Fourier transform is a little better but it does not really convey what is happening (Figure 4.5). Turning to the windowed Fourier transform in Figure 4.6, the two

components are clearly visible in both cases. The evolution of the chirp is clearer when the temporal width of the windowing function is reduced (lower figure); but the trade-off is the smearing in frequency space of the narrow-band constant tone.

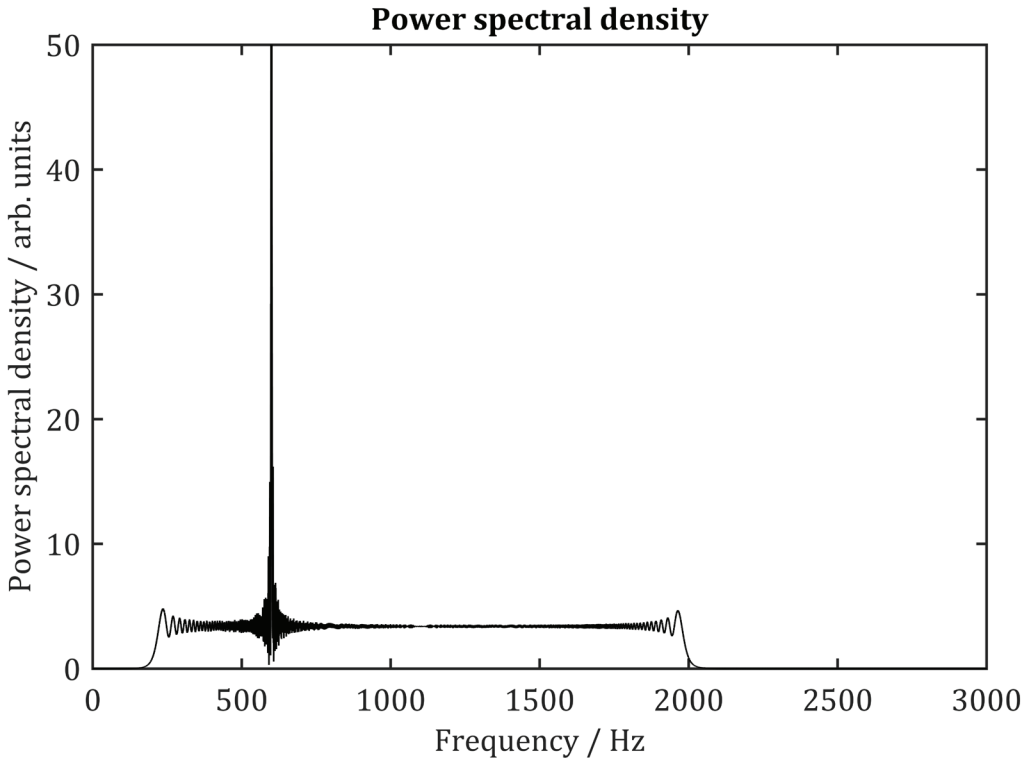

Figure 4.5. The power spectral density of a chirp superimposed on a constant tone.

A 200 Hz variable-pitch tone gradually rising to 2000 Hz (a 'chirp') is superimposed on a constant tone of 600 Hz. The chirp is twice as energetic as the tone; but this is not seen in this representation, which each frequency component over time.

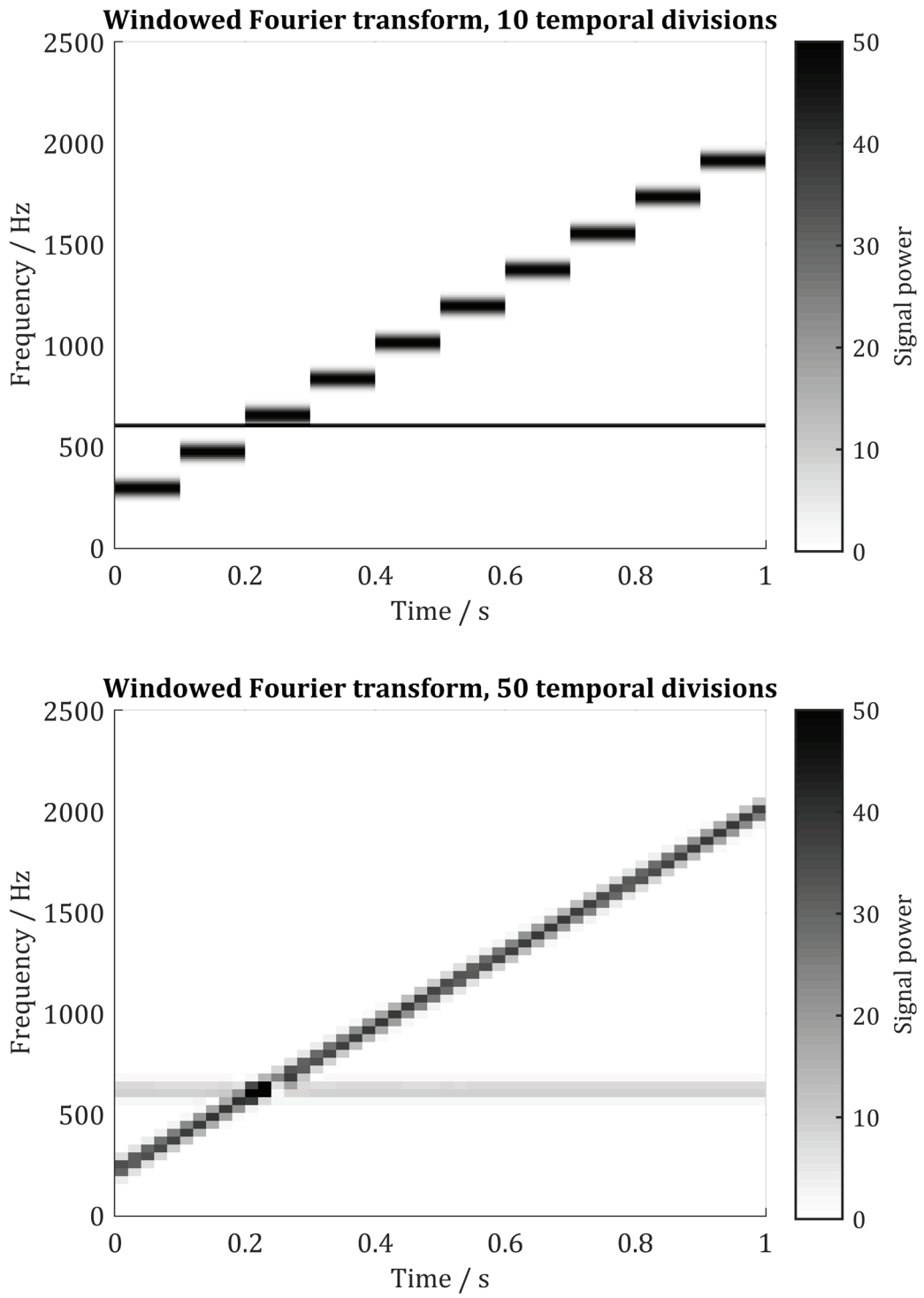

Figure 4.6. A windowed Fourier transform of the chirp superimposed on a constant tone. The data are the same as in Figure 4.10. The time axis is divided into equal width bins; in the top figure, there are ten bins, in the bottom figure, there are fifty. The Hann window function was used.

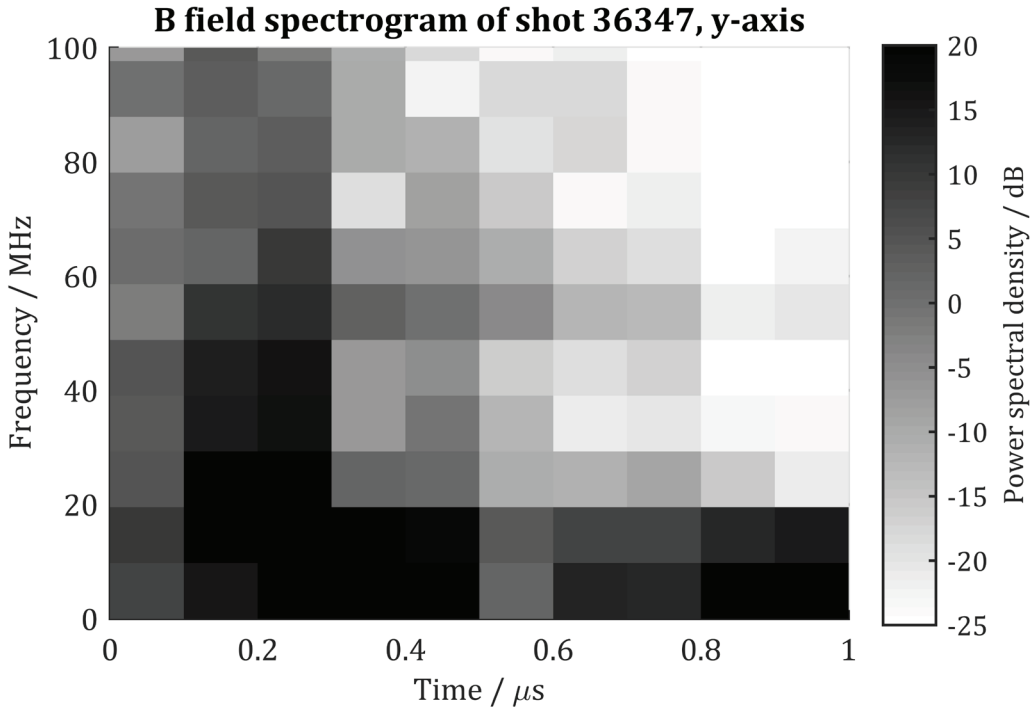

Figure 4.7. A spectrogram of the same data as given in Figure 4.2.

4.3.3. Real data example.

The data from Figure 4.2 are presented as a spectrogram in Figure 4.7. It is faintly possible to see a dark strip across the 50–60 MHz range, but it is not clear at all whether it is a real measurement or an artefact arising in the noise. A similar band of power is apparent in the x-axis as well (not shown), but it is absent in the z-axis.

4.3.4. Heisenberg boxes, or time-frequency atoms.

In one respect it might seem that by minimizing the width of g the temporal resolution and hence utility of the transform given in (4.21) could each be maximized. Unfortunately, as depicted in Figure 4.6, this is not the case; in constraining the effective width of g we merely expand the uncertainty on the frequency axis. Quantifying this relation, the minimum joint-uncertainty is ½.

Since g is symmetric, $g_{u,\xi} = e^{i\xi t} g(t-u)$ is centred about the constant u. The variance about that position is σ_t, which satisfies

$$\sigma_t^2 = \int_{-\infty}^{+\infty} (t-u)^2 |g(t-u)|^2 \left|e^{i\xi t}\right|^2 dt. \tag{4.22}$$

A change in the integration variable $t \to t-u$ does not affect the calculation, showing that the variance is not a function of u. Taking the Fourier transform, the spread in frequency space is

$$\sigma_\omega^2 = \int_{-\infty}^{+\infty} (\omega-\xi)^2 \left|\tilde{g}_{u,\xi}(\omega)\right|^2 d\omega. \tag{4.23}$$

Therefore,

$$\begin{aligned}\sigma_\omega^2 &= \int_{-\infty}^{+\infty} (\omega-\xi)^2 \left|e^{-iu(\omega-\xi)}\right|^2 |\tilde{g}(\omega-\xi)|^2 \, d\omega \\ &= \int_{-\infty}^{+\infty} (\omega-\xi)^2 |\tilde{g}(\omega-\xi)|^2 \, d\omega \\ &= \int_{-\infty}^{+\infty} \omega^2 |\tilde{g}(\omega)|^2 \, d\omega, \end{aligned} \tag{4.24}$$

which is independent of ξ. Applying the Fourier uncertainty theorem (4.17) we see that the joint uncertainty in the time-frequency resolution must be at least ½.

Although this result was discussed in the context of Fourier transforms, it actually applies to any transform operating between the time and frequency axes. Therefore a point (t_0, ω_0) on the time-frequency plane is ill defined, because the best resolution one can attain around such a 'point' is in fact an area of ½. Indeed, many transforms will occupy a larger area than this. The indivisibility of this area means that it is sometimes, in the context of a particular choice of transform, known as the *time-frequency atom*. (Mallat, 1998.)

4.3.5. On the choice of the window function.

The effect of windowing the circular functions $\{e^{i\omega t}\}$ is to introduce 'spectral leakage'; that is to say, a narrowband tone will exhibit frequency artefacts in the windowed representation, which do not correspond to tones in the true signal. The narrower the window, the greater the leakage; but the shape of the window has some effect as well. If the appearance of these artefacts is regarded as noise in the windowed Fourier transform

representation, then the choice of the window is often determined by the acceptable noise floor resulting from the transform.

The effective noise introduced by the spectral leakage may be characterized by the graph of the Fourier transform of the window function. This is not noise in a random sense, but is the result of the window function re-distributing spectral components.

The simplest window is simply a rectangular box;

$$g_{\text{box}}(t) = \begin{cases} 1 & -1/2 < t < 1/2, \\ 0 & \text{otherwise.} \end{cases} \tag{4.25}$$

However, the frequency response is not ideal for many purposes, see Figure 4.8. The central discrete Fourier transform 'bin' has leaked energy into the surrounding bins, so a sharp tone of narrow frequency response will be transformed to fill the neighbouring frequency bins.

An alternative is the Hann window;

$$g_{\text{Hann}}(t) = \begin{cases} \frac{1}{2}[1 - \cos(2\pi t)] & -1/2 < t < 1/2, \\ 0 & \text{otherwise.} \end{cases} \tag{4.26}$$

The graph of this function is given in Figure 4.9, together with the spectral leakage plot. The leakage now is much reduced, but it is no longer uniform across the neighbouring frequencies.

In my work, I was guided by minimizing noise. I preferred the Hamming window.

$$g_{\text{Hamming}}(t) = \begin{cases} \alpha - \beta\cos(2\pi t) & -1/2 < t < 1/2, \\ 0 & \text{otherwise.} \end{cases} \tag{4.27}$$

with $\alpha = \frac{25}{46}$ and $\beta = 1 - \alpha$. The choice of constants cancels the first side lobes in the Hann window, making it slightly better in that respect.

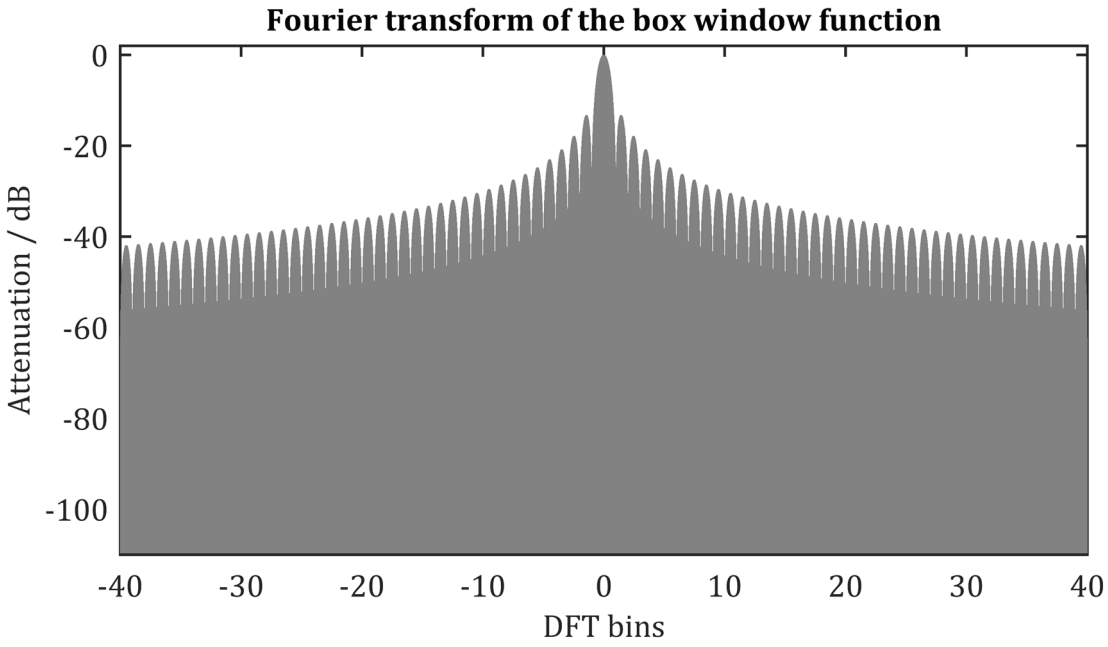

Figure 4.8. The frequency response of the rectangular box window function.

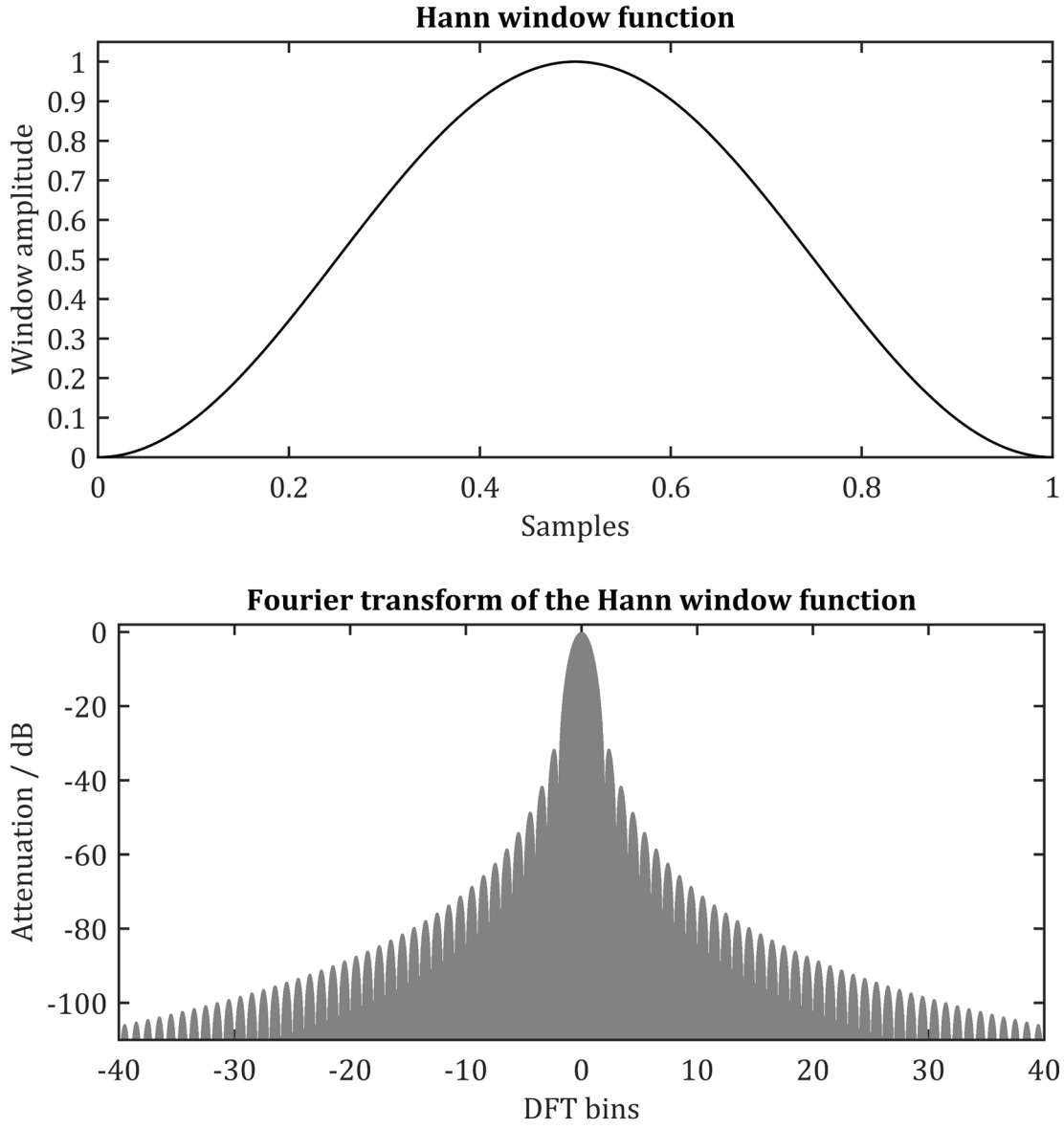

Figure 4.9. The Hann window (top) and its Fourier transform.

4.4. WAVELET ANALYSIS

A wavelet can be considered as a singular, brief oscillation, or a small packet of oscillations. In convolving these wave packets with the signal, correspondences between the signal and the particular wave packet appear where the signal has a component matching the packet—this is a similar idea to the Fourier analysis, except now the pattern against which the signal is to be matched can be almost arbitrary. Moreover, a complex wavelet enables the preservation of phase information from the signal; in particular in the joint analysis of multiple signals the relative phase can be important.

Analysis by wavelets defeats one limitation of windowed Fourier transforms whereby the resolution is uniform over the time-frequency plane. Wavelets thereby enable the simultaneous extraction of features of differing size on that plane, and it is not necessary to make a 'guess' about the appropriate window size to elucidate the features in question. However, it cannot defeat the fundamental minimum size of that atom (see section 4.3.4). Further, wavelets can also be designed to highlight transient features that are not easily detectable with Fourier methods. (Mallat, 1998.)

The wavelet.

A wavelet $\psi \in \mathbf{L^2}(\mathbb{R})$ has zero average, is normalized to unity ($\|\psi\| = 1$), and is centred about zero. In like manner of (4.2), ψ can be translated and scaled to produce a 'family' of wavelets $\{\psi_{u,s}\}$,

$$\psi_{u,s}(t) = \frac{1}{\sqrt{s}}\psi\left(\frac{t-u}{s}\right), \tag{4.28}$$

where the factor $1/\sqrt{s}$ preserves $\|\psi_{u,s}\| = 1$.

To give an idea of what a wavelet 'looks like', consider as an example the Morlet wavelet. The Morlet wavelet is a complex exponential modulated by a Gaussian envelope; the envelope localizes the exponential. The equation describing the wavelet is (in this case)

$$\psi_{\text{Morlet}}(t) = \frac{1}{\sqrt{2\pi}} e^{i\sigma t} e^{-\frac{t^2}{2}}. \tag{4.29}$$

The quantity σ determines the bandwidth of the wavelet. The Morlet wavelet does not have compact support, but actually its value quickly becomes negligible a few oscillations from the central position. The effect of scaling the wavelet and translating it

is shown in Figure 4.11. The wavelet has both non-zero real and imaginary components; the imaginary part enables it to track changes in the phase of the structure it detects. Another example is the Haar wavelet, which behaves rather differently:

$$\psi_{\text{Haar}}(t) = \begin{cases} 1 & -1/2 \leq t < 0, \\ -1 & 0 \leq t < 1/2, \\ 0 & \text{otherwise.} \end{cases} \tag{4.30}$$

ψ_{Haar} is not continuous and so not differentiable, but for analysing discontinuous or sharply rising transients in noise this is an advantage; an example might be detecting the sudden failure of machine tools (Li *et al.*, 2007). ψ_{Haar} has compact support.

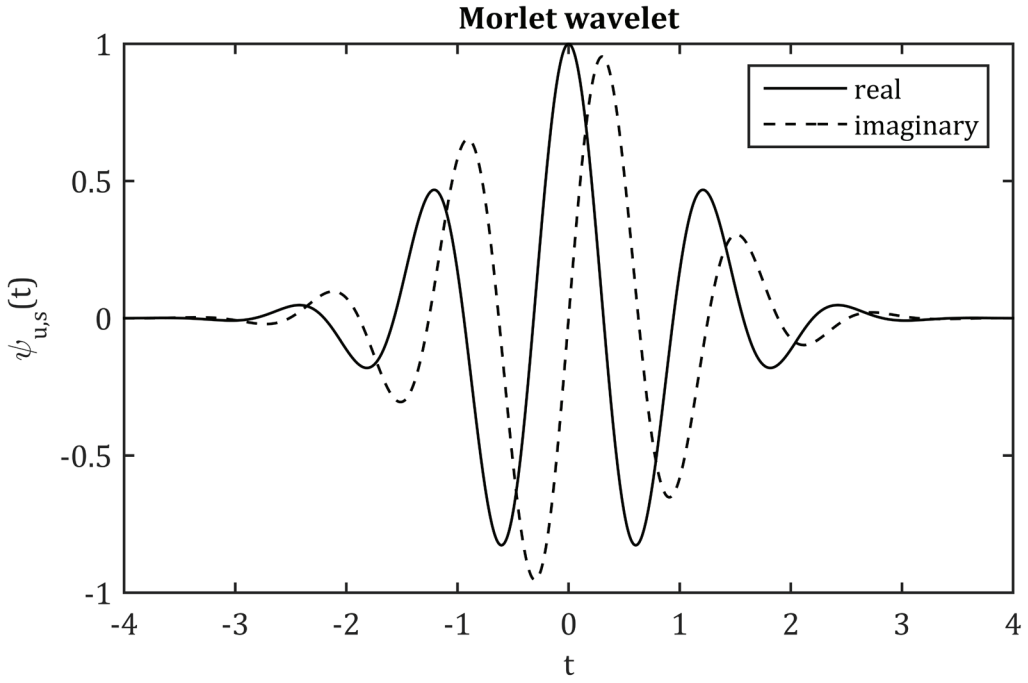

Figure 4.10. A Morlet wavelet, with the real and imaginary parts shown. The function describing the wavelet is given in (4.29).

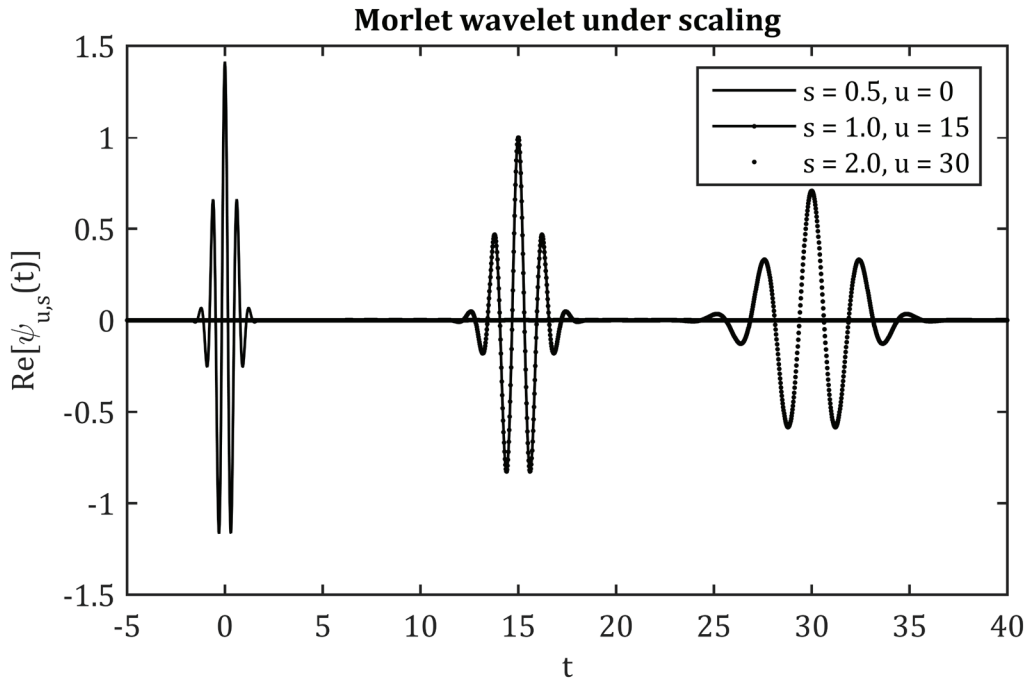

Figure 4.11. The effect of rescaling and translating a wavelet.
The Morlet wavelet previously presented in Figure 4.10 above is here shown at three different scales and positions. Translation does not adjust the shape of the wavelet; it is shown in different positions for clarity.

The continuous wavelet transform.

Let $f \in \mathbf{L^2}(\mathbb{R})$. Then the wavelet transform of f around time u and at scale s is denoted $\mathcal{W}_{u,s}(f)$ and is given by

$$\mathcal{W}_{u,s}(f) = \langle f, \psi_{u,s} \rangle = \int_{-\infty}^{+\infty} f(t)\psi_{u,s}^{*}(t)\, dt. \tag{4.31}$$

This has the appearance of the windowed Fourier transform (4.21), except that now our choice of the windowing function g has become less restricted.

There is a trade-off in loosening this restriction on the nature of the basis functions for the transform, in that the relationship between the scale factor s of the wavelet and the frequency variable ω becomes less straightforward. First, one may examine the wavelet transform of a sine wave of known period (Meyers *et al.*, 1993). For wavelets of particularly irregular nature, lacking dominating Fourier components, it is probably a meaningless exercise to draw a relation between the Fourier and wavelet scales. For wavelets that are essentially modified Fourier transforms, such as the Morlet wavelet, the

connection between the scale and frequency is more straightforward and, for an appropriate choice of parameters, the Fourier and wavelet periods can be almost equal.

With that caveat aside, the conversion between scale and frequency can in general be expressed

$$\omega(s) = \frac{\omega_c}{st_\delta}, \tag{4.32}$$

where $\omega(s)$ is the frequency (or 'pseudo-frequency') of the wavelet at scale s, ω_c is the central frequency of the wavelet in question, and t_δ is the time interval intervening between successive sampling points. I take the central frequency ω_c of a particular wavelet to be that of the maximum Fourier component composing the wavelet.

4.4.1. The relationship between transforms of the Fourier type, the windowed Fourier type, and the wavelet type.

Each of the three transforms so far described has differing advantages and disadvantages compared with the others. An advantage arising not least in the case of the Fourier transform is its computational simplicity and ubiquity.

One way of distinguishing the transforms is to review the frequency-time graph for each; for instance see Figure 4.12. I have already reviewed the concept of the time-frequency atom, and we can extend this analysis to look over the entire graph, where each division on the graph has an area of at least the time-frequency atom. In the case of the ordinary Fourier transform, the time axis is undivided (so there is no temporal resolution) but the frequency axis is divided equally as often as may be permitted by the time record length. The windowed Fourier transform has a temporal axis divided on the basis of the window function's width; these are typically equal divisions, and the frequency scale is accordingly divided. For the wavelet analysis, more temporal resolution is given for lower frequencies but at the higher end of the spectrum we are able to obtain a better understanding of the temporal evolution.

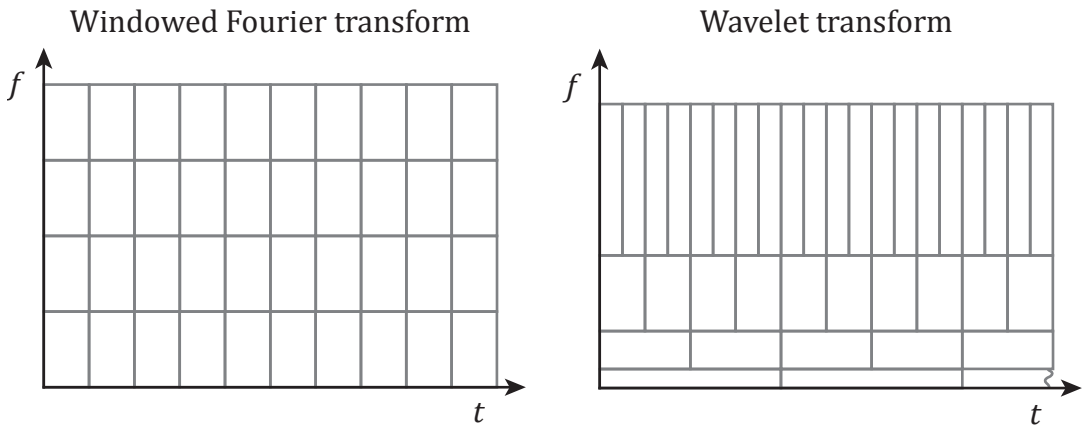

Figure 4.12. The division of the time-frequency plane under a windowed Fourier transform and under a wavelet transform, in schematic.
In the case of the windowed transform, the division is equal across the time-frequency plane. For a wavelet transform, greater frequency resolution is accorded to lower-frequency signals. In this schematic the effect has been somewhat exaggerated.

Table 2. A summary comparison of the three signal transforms so far discussed.

	Basis function	**Temporal resolution**	**Frequency resolution**	**Periodicity is assumed?**
Fourier transform	$\exp(i\omega t)$	None	Maximal	Yes, over the entire signal
Windowed Fourier transform	$g(t-u)$ $\times \exp(i\omega t)$ (For a window g)	Set by window width	Inverse of window width	Within each window
Wavelet transform	Many choices	Varies throughout the frequency-time graph		No

4.4.2. Effects arising at the edge of the measurement.

Most measurements performed are not cyclical, and there is often a sharp discontinuity at the edge of the measurement where the signal suddenly begins, or where it is abruptly truncated. The transform is not considered reliable when it is too close to this

corruption, particularly if the wavelet's support has extended into the null region. To quantify that, the points within two *e*-folding distances of the edge can be shown as greyed out (see figure in section 4.4.4). However in the real data I analyse, this effect was not important because of long record lengths, and therefore I did not apply this fade-out convention in my other graphs.

4.4.3. On the choice of wavelet.

Unlike Fourier transforms, the space of basis functions available for undertaking a wavelet transform is evidently quite broad: a choice must be made for the function ψ in (4.28) and (4.31). Torrence and Compo (1998) suggest, in their paper on the subject of applying wavelet analyses to climate data, that four considerations guide the choice of wavelet; that is to say, whether the wavelet takes on complex values or is wholly real-valued; the width, or, e-folding time of the wavelet amplitude; the shape of the wavelet graph as compared with the expected feature to examine; and finally the orthogonality of the wavelet. To this I would add the quality of the relationship between the scale and Fourier period, as discussed in section 4.4.1.

I use the continuous transform as it is reputedly better for feature extraction than its discrete equivalent (e.g., Grinsted *et al.*, 2004). That is to say, non-orthogonal wavelets are preferred. Complex-valued wavelets capture phase information, for better detection and characterization of oscillations, and I prefer them for that reason. In terms of shape, I prefer wavelets resembling sine functions, as packets of electromagnetic waves are expected to be of this basic nature. This also happily permits that the relationship between the scale and the true frequency is not too intricate.

The wavelet width is important as well; a narrow width enables the function to be better at detecting temporally transient events, but necessarily has a broader spread in frequency space. Further, the corruption occurring from edge effects means that the narrower-width transform will be more resilient to edge effects close to the start or end of the measurement.

From these considerations, I find that the Morlet wavelet is often the preferable choice.

4.4.4. A synthetic example of a wavelet analysis.

I show the linear chirp with the constant tone superimposed, from the same data as in Figure 4.6. I use a Morlet wavelet. The feature extraction is quite distinct; however, unlike the windowed Fourier transform, it suffers from the loss of frequency resolution at higher frequencies. Because the frequency resolution is reduced, a long-term narrowband signal is accordingly distributed over a larger space on the frequency-time graph; therefore the apparent energy in the signal will fall. Thus, the correspondence between the wavelet coefficient, as represented on the graph by the intensity of the colour, and the true energy of the signal, is not fixed over the frequency-time plane. Instead, signals of equal amplitude will appear in the wavelet representation to be more intense at the lower end of the spectrum and less intense at the higher end.

To show a bit more of the power of wavelet analysis, I introduce two repeating sharp tone patterns onto the same data, at 400 Hz and 2 kHz. Again these are well detected by the wavelet analysis, as seen in Figure 4.14. However, some corruption between the separate components is visible particularly as the chirp approaches the 2 kHz repeating tone; this underscores the importance of choosing the right wavelet for the task.

4.4.5. A real example.

Figure 4.15 shows the wavelet power (the square of the wavelet transform) over the time-frequency plane. In subfigure (a), data from the x-axis are presented; in subfigure (b), the data are from the y-axis. The component seen previously, but only weakly, at around 50–60 MHz now appears quite distinct and more narrowly defined on the time-frequency plane, in particular on (b). Regrettably, in (a) the region is swamped with a short-lived by wideband component. This is not present in (b), but there is a hint of a shorter-lived feature at about 80 MHz. Since the data from both axes are important in determining, for example, whether a circularly polarized wave is present, it would be useful to compare the two components with a more unified methodology. More importantly in determining the nature of these processes and whether the two axes are physically showing the same information, it would be interesting to compare the relative phases of the features.

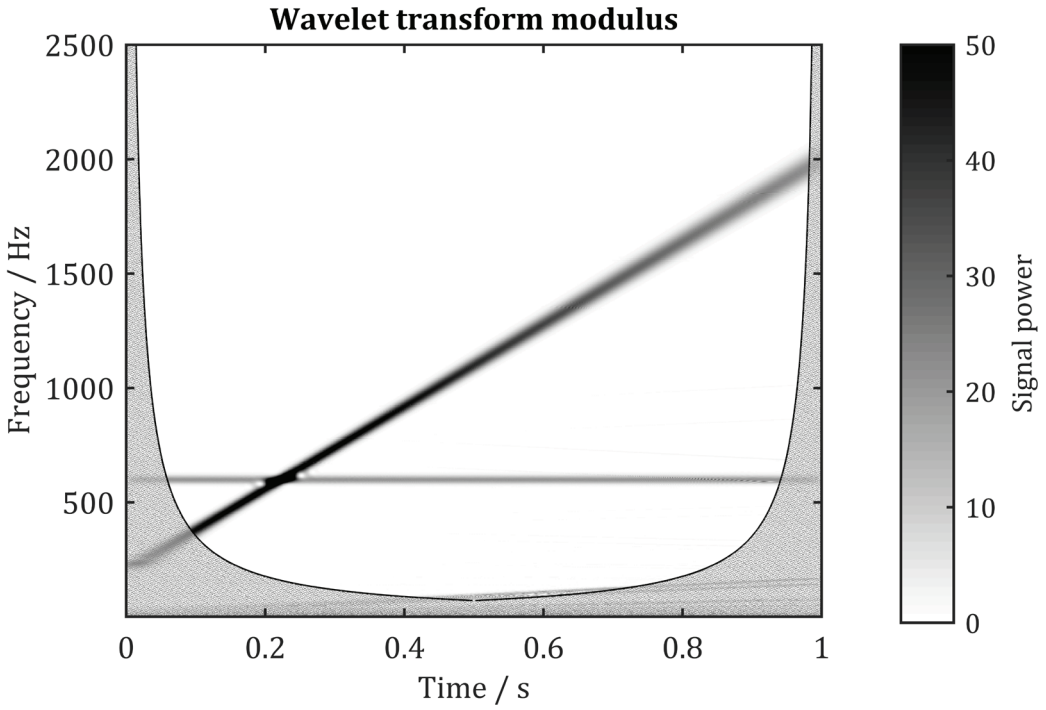

Figure 4.13. A wavelet transform of a chirp and a superposed constant tone. The data are the same as in Figure 4.6. The data that might be corrupted by edge effects, within two e-folding times of the edge, have been shadowed.

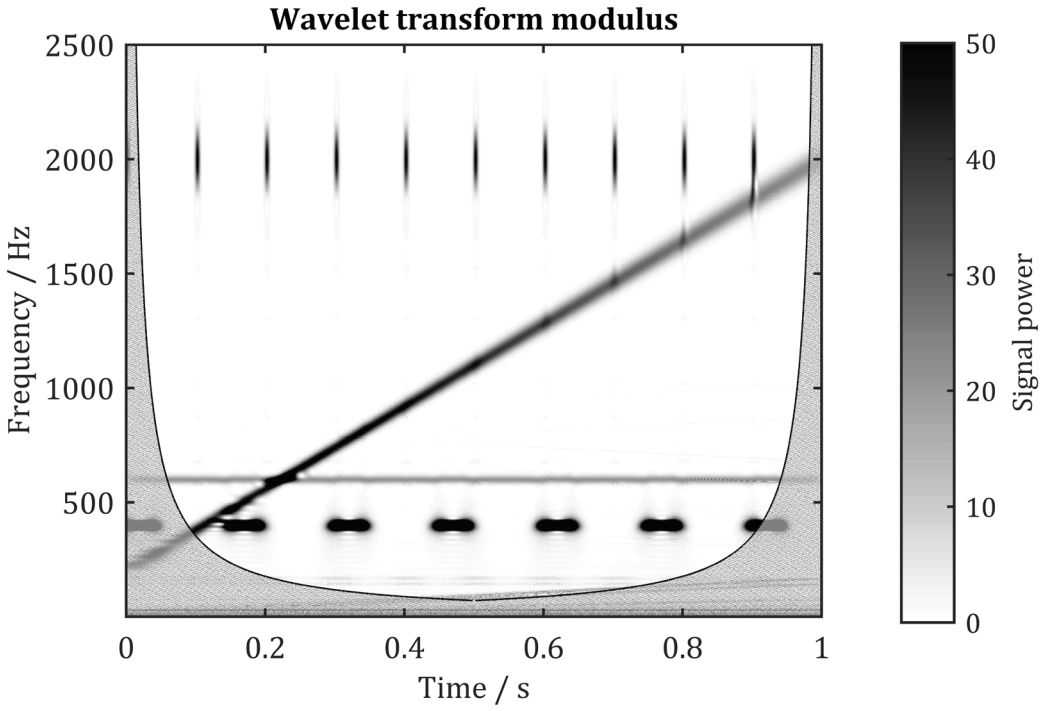

Figure 4.14. A wavelet transform showing four distinct signal components; regions susceptible to edge effects are placed in shadow.

4.4.6. Cross wavelet and phase coherency analysis

Wavelet analyses can be very sensitive, but the nuance involved in selecting the appropriate wavelet leaves them liable to a certain degree of subjectivity and thus prone to producing false positives. One remedy for this is to compare two measurements of the same system; if the same frequency component can be identified in two independent measurements it is some evidence that the detected signal is not likely an artefact arising from noise in one particular measurement. However this does not eliminate the possibility, for instance, of narrowband noise corrupting two measurements. A further check is to compare the phase coherency between the two signals. If the two have a consistent phase relationship at a given frequency component, it becomes still more improbable that this coincidence arises from Gaussian noise. Later, I shall discuss the use of this technique to compare signals collected from two orthogonal axes of the bdot probe. The intention is to show that if coherent signals are detected on two orthogonal axes with a consistent ninety-degree phase relationship in one frequency band for a sustained time period, then this is evidence of a circularly polarized magnetic wave propagating past the bdot probe.

Wavelet power spectrum (WPS).
Let $f \in \mathbf{L^2}$ be a signal. Then the wavelet power spectrum of f at scale s and time u is

$$\mathrm{WPS}_{u,s}(f)\,, = \langle \mathcal{W}_{u,s}(f)\mathcal{W}^{*}_{u,s}(f)\rangle, \tag{4.33}$$

where $\mathcal{W}$ is the wavelet transform as defined in (4.31), the asterisk denotes the taking of the complex conjugate, and here the application of the angle brackets $\langle\cdot\rangle$ is the taking of an expectation value. The calculation of the expectation value is discussed below.

The wavelet power spectrum is analogous to the power spectrum under the Fourier transform, but because the frequency-time ratio changes as a function of frequency, a narrowband signal can become distributed over a Heisenberg box of larger and larger frequency dimension. Therefore, the expected power for such a signal will fall with frequency, unless allowance is made.

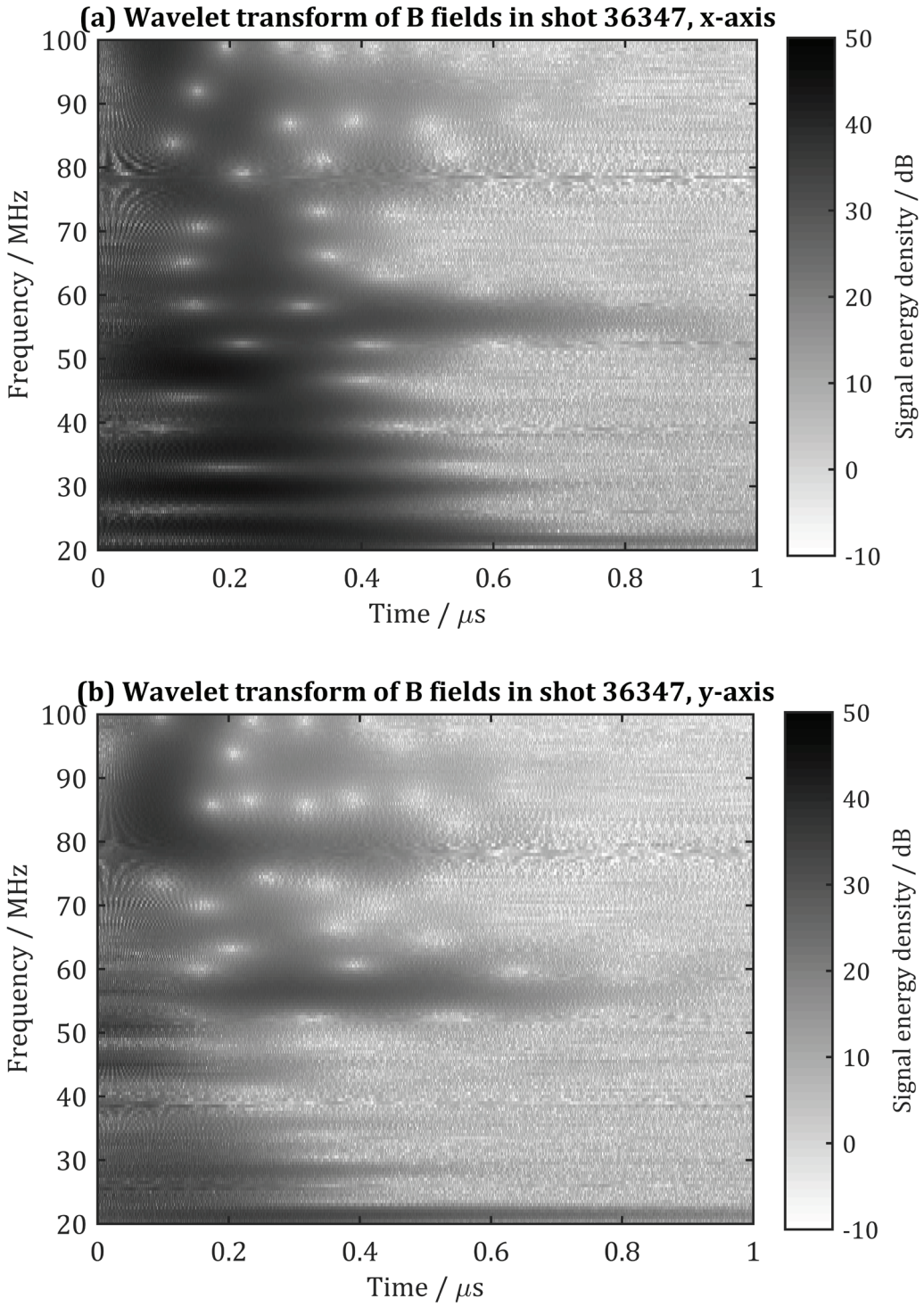

Figure 4.15. A wavelet transform of the same data as given in Figure 4.2, taken from (a) the x-axis and (b) the y-axis of the probe.

4.4.7. Cross wavelet power, and the coherency of two signals.

The wavelet cross spectrum (WCS).

For two signals $f, g \in \mathbf{L^2}$, the cross wavelet spectrum at time u and scale s is written $\mathrm{WCS}_{u,s}(f,g)$ and is given by

$$\mathrm{WCS}_{u,s}(f,g) = \langle \mathcal{W}_{u,s}(f)\, \mathcal{W}^*_{u,s}(g) \rangle, \tag{4.34}$$

where $\mathcal{W}^*_{u,s}(g)$ is the complex conjugate of the wavelet transform of g at (u,s), and $\langle \cdot \rangle$ represents the taking of an expectation value (Maraun & Kurths, 2004). The expectation value is computed by smoothing over the dataset. $\mathrm{WCS}_{u,s}(f,g)$ is a complex quantity whose imaginary component reveals the phase separation Φ between f and g under the wavelet at the specified scale and time:

$$\mathrm{WCS}_{u,s}(f,g) = \left|\mathrm{WCS}_{u,s}(f,g)\right| e^{i\Phi}. \tag{4.35}$$

One difficulty with taking the cross wavelet power of two signals is that if one of the wavelets of one of the signals individually has a particularly large magnitude, the cross wavelet product will also be large, even though the joint power (or correlation) between the two signals might be small. To limit this problem, the wavelet signals should be normalized, by computing the local expectation value of the signal in what is essentially an averaging process. This is what we do with the wavelet coherency estimation.

Cross-wavelet coherency (WCO).

The wavelet coherency index WCS represents the degree of correlation between two signals.

$$\mathrm{WCO}_{u,s}(f,g) = \frac{\left|\mathrm{WCS}_{u,s}(f,g)\right|}{\sqrt{\mathrm{WPS}_{u,s}(f)\, \mathrm{WPS}_{u,s}(g)}} \tag{4.36}$$

Both the numerator and denominator involve taking the expectation value:

$$\mathrm{WCO}_{u,s}(f,g) = \frac{\left|\langle \mathcal{W}_{u,s}(f)\, \mathcal{W}^*_{u,s}(g) \rangle\right|}{\sqrt{\langle \mathcal{W}_{u,s}(f) \mathcal{W}^*_{u,s}(f) \rangle \langle \mathcal{W}_{u,s}(g) \mathcal{W}^*_{u,s}(g) \rangle}}. \tag{4.37}$$

The expectation operator $\langle \cdot \rangle$ does not commute with transforms; if merely a simple smoothing process is carried on f and g before the transforms are taken then the WCO index will be everywhere unity. The transform is quite sensitive to the value of the expectation operator used. For the most part I apply an n-point smoothing operator.

4.4.8. A synthetic example.

Let us consider two independent Gaussian white noise processes. Only the first noise process will have super imposed onto it a short tone at 2000 Hz that repeats every 0.01 s. Both processes have imposed on them a common 1000 Hz repeating tone, but in the case of the second signal, the tone has a $\pi/2$ phase lag with respect to the tone in the first signal. The tones each have an amplitude 25% larger than the mean Gaussian noise. The wavelet transforms of these two signals are given in Figure 4.16; a Morlet wavelet is used with choice of parameters to enable a close to 1:1 mapping from scale to frequency.

The effect of taking the cross wavelet spectrum is presented in Figure 4.17. In the top panel, the joint-signal power is given, highlighting regions on the frequency-time graph (or scale-time graph) of common power. The 1000 Hz tone is clear, since it is present in both signals. The 2000 Hz tone, however, was not in the second signal so it is strongly suppressed in the joint transform. (As there will be correspondences between the noise in the second transform and the 2000 Hz tone by chance, elements of it remain just visible.) In the middle pane, the phase angle delta between the two signals is given. However, where the signals are little more than noise, this is a spurious, rapidly evolving quantity. Therefore, it is shown faded out where, in the case of either signal, the magnitude is below an *a priori* estimate of the noise. What remains, in this case, is the 1000 Hz stripe comprising the train of discrete tones. Although not necessary in this example, in the final pane only signal differences of $-\pi/2 \pm \pi/6$ have been selected; the other angles are shown as white. In this example, a clear identification of a common, albeit phase-lagged component, can be made.

4.4.9. A real example.

Figure 4.18 shows a wavelet coherency analysis of the real x and y data from the bdot probe. There is a clear strip running from 0.2 μs to about 0.8 μs at about 55 MHz, suggesting common energy on both axes here at this frequency. There are other regions on the graph with common power as well, including in the very lowest frequency of the spectrum and briefly at just below 30 MHz.

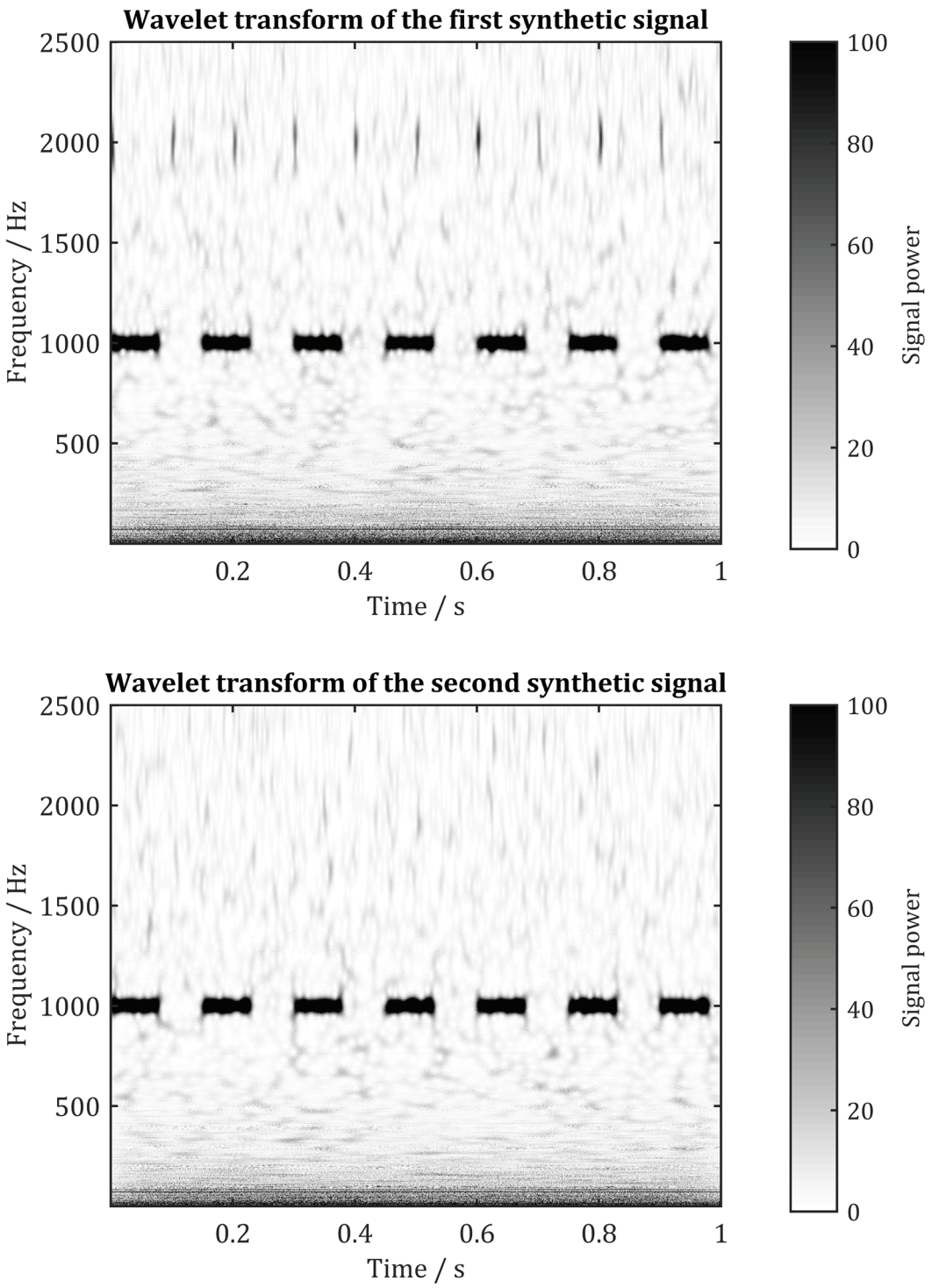

Figure 4.16. Wavelet transforms of the two signals discussed in the text.

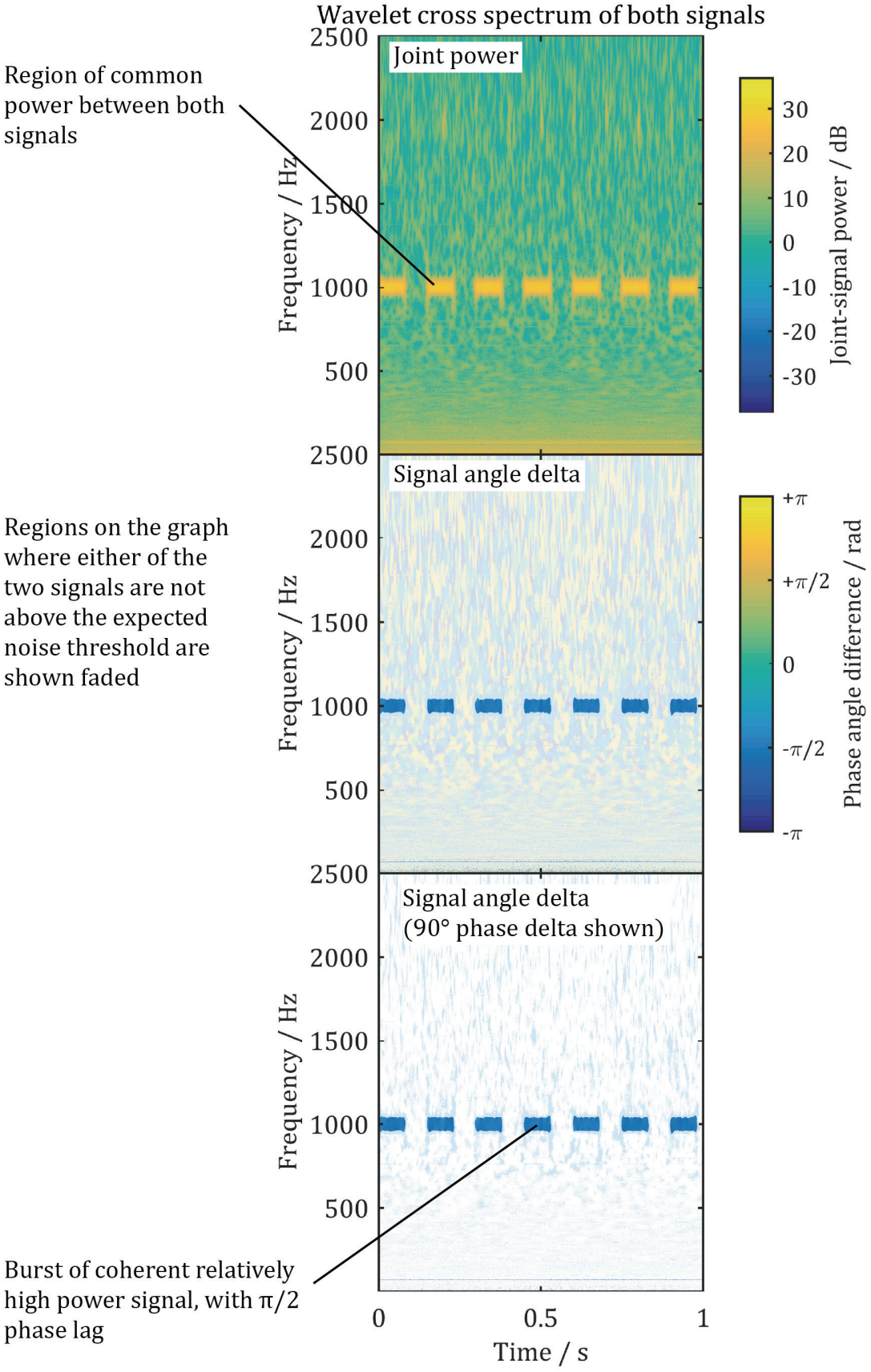

Figure 4.17. Wavelet coherency analysis: see accompanying text on page 95.

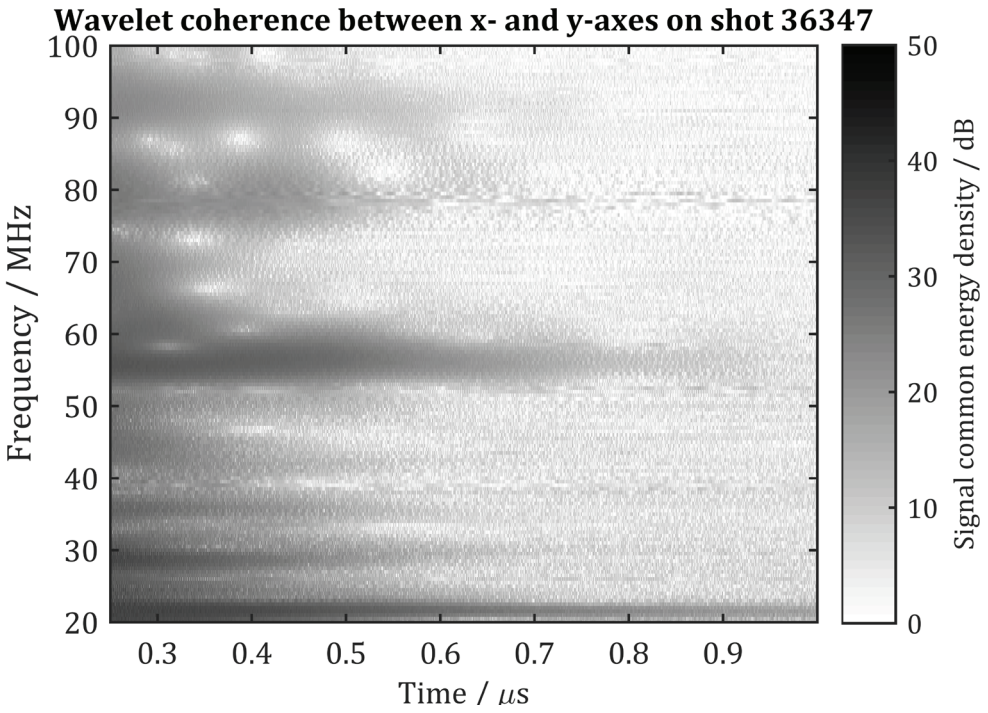

Figure 4.18. A wavelet coherency analysis of the same data as given in Figure 4.2.

4.5. SUMMARY OF THIS CHAPTER

I have reviewed the basic principles of three related signal analysis techniques, starting with Fourier analysis and showing how it can be extended to cover varying sinusoidal signals with the windowed Fourier analysis. I go further to talk about non-stationary signal analysis with the wavelet transform and in particular the ability of the wavelet coherency transform to take two signals and determine if they share common components, up to and including phase drifts (which may be quantified).

5. EXPERIMENTS

In this chapter I discuss four experiments. The principal experiments are two I undertook at the GEKKO facility, at the Institute of Laser Engineering, Osaka University. I produced laser-driven shocks in a nitrogen atmosphere, using a bdot probe to monitor the generation of magnetic fields. In the first experiment, wavelet examination of the magnetic field data suggests that, only when a background field is imposed, a right-handed propagating wave is excited. In the second GEKKO experiment, under slightly different conditions, no such waves were observed; an explanation of this is given in the next chapter.

The third experiment discussed was performed at Target Area West, on the Vulcan facility at Rutherford Appleton Laboratory. The experiment was intended to demonstrate the amplification of self-generated magnetic fields through plasma turbulence. That aspect is discussed in (Meinecke *et al.*, 2014). I look in particular at the electron spectrometry.

Finally the fourth experiment was done at the *Laboratoire d'Utilisation des Lasers Intense* (LULI), at the École Polytechnique in France. That experiment concerned the production of magnetic fields of particularly high magnitude using a capacitor-type laser target. See Santos *et al.* (2015). The fields generated were short-lived, and provided a useful platform for investigating the true bandwidth of the probe—in the sense of the fastest pulsed field it could detect, with reference to the same field examined by other diagnostics.

5.1. PRODUCTION OF SHOCK WAVES AT THE GEKKO FACILITY

I used the GEKKO laser facility at the Institute of Laser Engineering, Japan to drive shockwaves in low-pressure nitrogen and to study the effect of imposing an ambient magnetic field on the generated magnetic field configuration. In particular I wanted to see if it were possible to drive magnetic field waves into the unshocked material upstream of the shock front in a manner somewhat analogous to the Earth's bow shock or other astrophysical shock structure.

The experiment showed that the generated magnetic field was increased in magnitude by the presence of the background field. The experiment also showed that right-handed circularly polarized waves could be produced in the laser-laboratory.

5.1.1. The experiment design.

The experiment design is shown by schematic in Figure 5.1 below. 351 nm light illuminates a cylindrical carbon rod of diameter 500 μm, with laser focal spot 250 μm and pulse length of 500 ps. The driver energy was varied, with values of 480 J, 850 J or 1280 J, depending on the number of beams used during the illumination. This prompted the generation of a shockwave, expanding into the surrounding nitrogen. The nitrogen initial fill pressure was 1 mbar. A permanent magnet was present in some experiments to provide an ambient field on which whistler waves if excited could propagate. The rod surface is heated under the light flux, and impulsively expands, acting as a piston to drive a shock front into the nitrogen. The nitrogen is probably at least partly ionized by the initial laser flash. To characterize this shock front, time-resolved interferograms are captured at 15 ns and at 25 ns, and temporally streaked self-emission images are recorded between 25 ns and 50 ns.

To effect a parallel magnetic field in the region at and near the shock front, I placed a removable commercial neodymium magnet directly above the rod to produce a magnetic field directed along the rod's extended axis. I used a Hall probe to measure the field strength of the magnetic and confirm it is indeed dipolar, or at least decaying with cubic distance along the axis. A plot of the measured magnetic field values and the fitted

curve (to a dipolar field, on the z-axis with the form $B(z) = \mu_0 m/2\pi z^3$) is given in Figure 5.2.

For each laser energy value, one shot was taken with the permanent magnet in place, and one with it removed, so that a 'null' comparison could be made. I obtained six measurements: three with the field in place and three without. The bdot probe was positioned directly below the rod so that the imposed field is approximately parallel at its position, coincident with the z-axis. The probe is not sensitive to static fields, but only detects changes in the magnetic field.

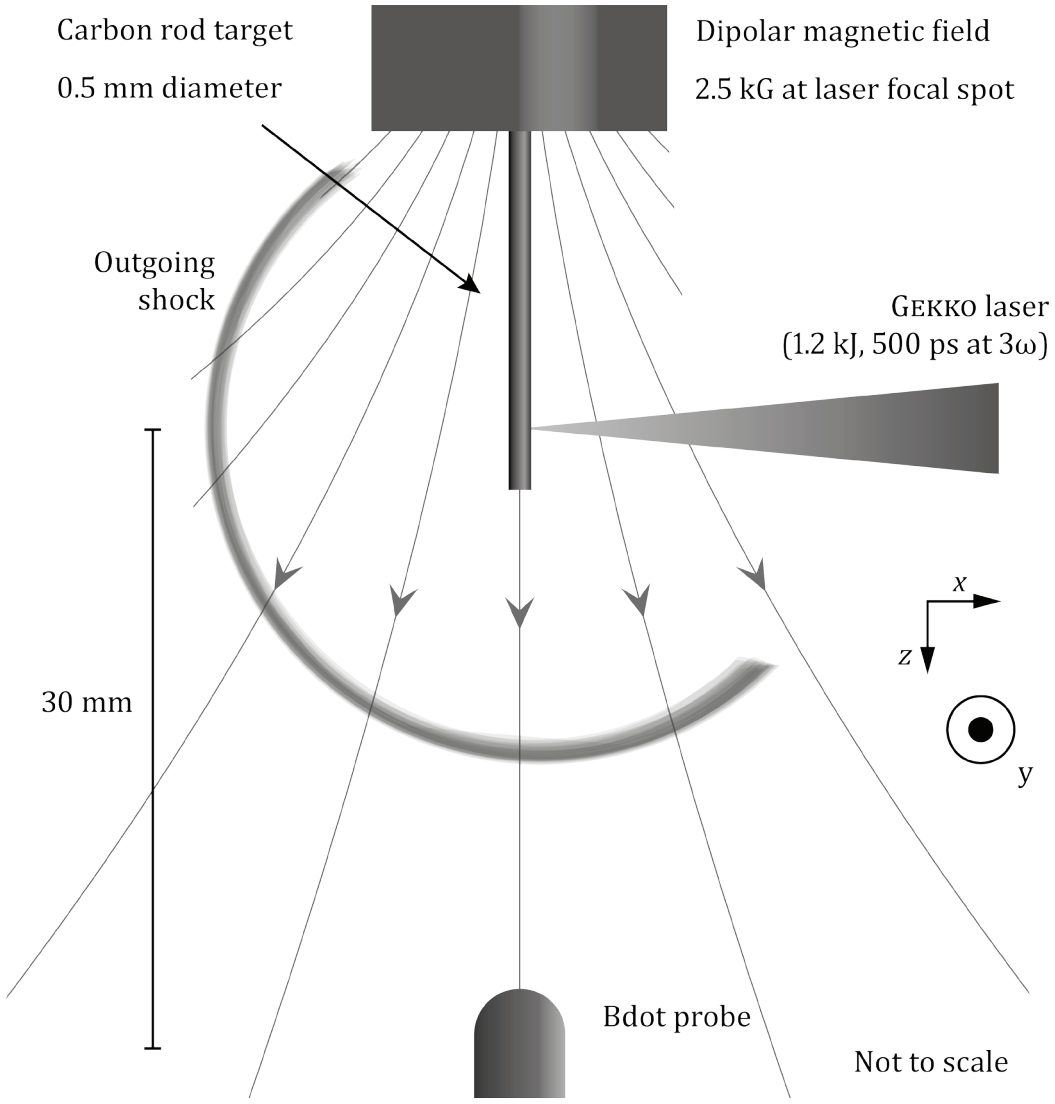

Figure 5.1. A schematic of the experiment performed at the GEKKO facility in 2012.

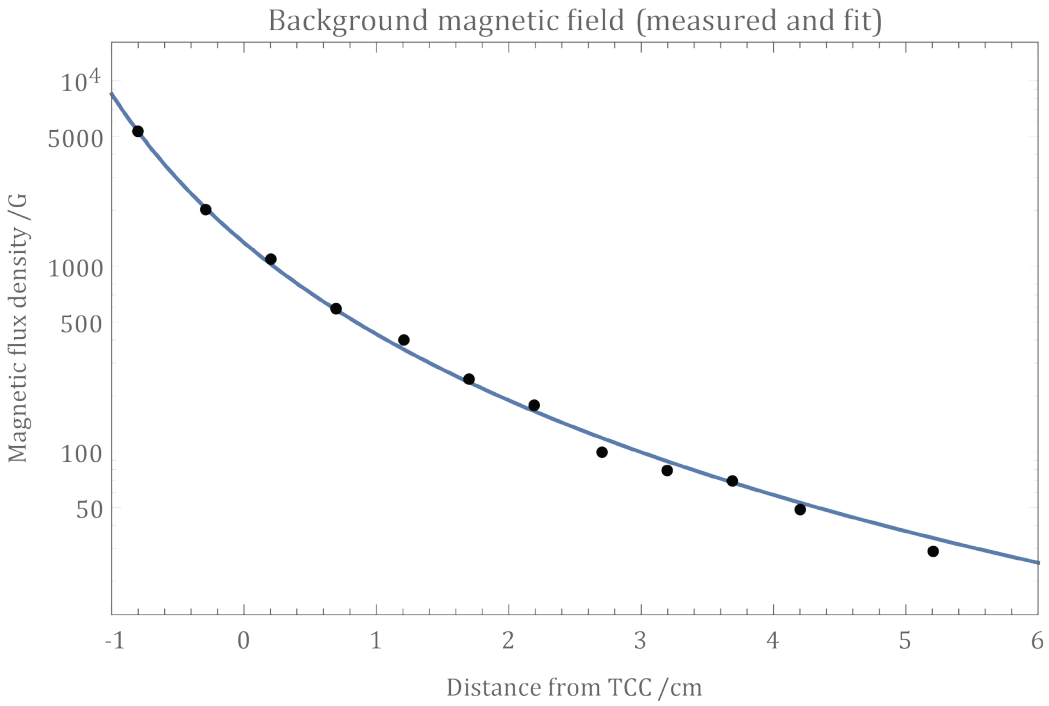

Figure 5.2. The magnetic field strength of the permanent magnet, with distance from the target chamber centre along the dipole axis of the magnet. The magnet surface is at -0.8 cm.

5.1.2. Interferometry.

The raw interferometric images from low energy (480 J) shots are presented in Figure 5.3. The magnetic field is not observed to have any effect on the shock propagation in any shot. The driving energy in both cases was 480 J (± 6 J) of 321 nm light, from two shots; the left panes show the state of the target prior to the laser firing; the right panes show the state of the plasma 15 ns after firing. The laser fires from the right side of the page. The presence of the magnetic field in the lower two images is expected to make no difference to the shock generation or propagation. A shock front is faintly visible in each case as a slight ridge in the interferometry fringes.

The fringe patterns can be readily discerned by the human eye, but for a numerical analysis the fringe geometry must be understood by the computer. The presence of anomalous, individual bright pixels is a bar to this, as is the variable brightness and contrast across the image—because typical computational analyses consider the absolute

value of the pixel brightness whereas the human vision processing is sensitive to contextual contrast. (The variable brightness arises because the laser is not uniformly bright on the imaging chip.) I apply a despeckle filter over each image to remove errant individually bright pixels. I also run a local thresholding tool over the images, which converts the image into a binary, black-or-white image. That is to say, a pixel is made totally black if the pixel brightness is below a certain threshold, and totally white if above. In the local thresholding model, the local contrast (within say 30 pixels) determines the requisite threshold brightness for choosing if a pixel is considered 'black' or 'white'. Neither of these processes alters the inherent information contained in the image, which is the fringe geometry, but rather makes the information more amenable to computational interpretation. In Figure 5.4 I show the effect of this first part of the interpretation process.

Subsequently the image is passed through a two-dimensional Fourier transform, and the highest frequency components—corresponding to the uneven fringe edges and the remaining speckle—are zeroed out with a mask. A reverse transform gives a clean fringe pattern, whose values are modulo 2π. Finally, the fringe pattern is 'unwound', by which I mean, the cyclical white-dark-white fringes are converted to a linear, monotonically increasing phase component from top to bottom. This entire process is applied to both the reference and the data image; the reference phase map may then be subtracted from the data map to give the effective phase change arising because of the plasma. The technique in this paragraph follows from Gregory (2007).

Finally I implement (3.25) in MATLAB, a convenient software package for numerical data analysis, to obtain an estimate of the electron density in the cylindrical assumption. I present the density profiles from all six shots at the two different times (15 ns and 25 ns) below.

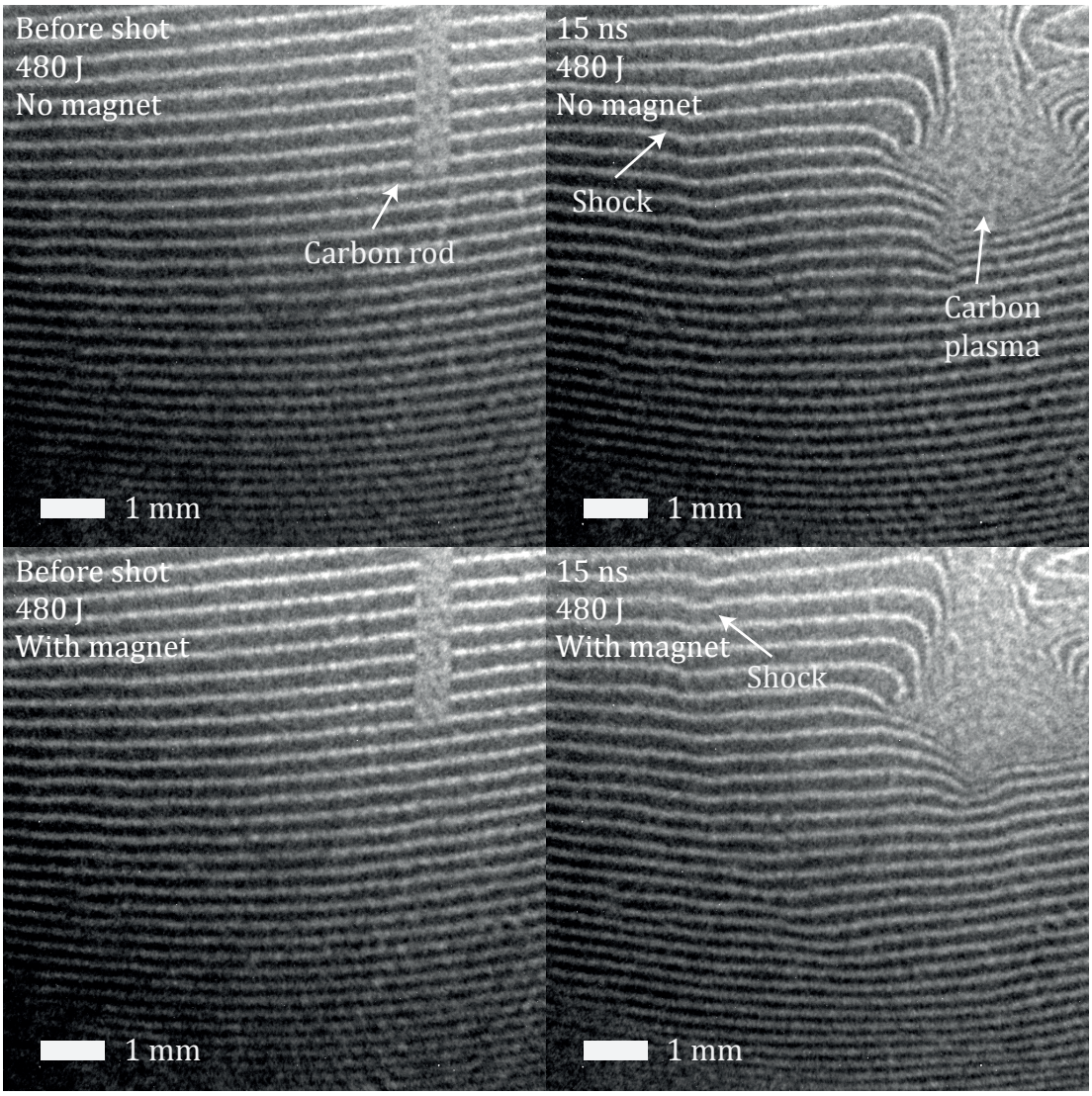

Figure 5.3. Interferometry pictures captured at 15 ns in the GEKKO 2012 experiment.

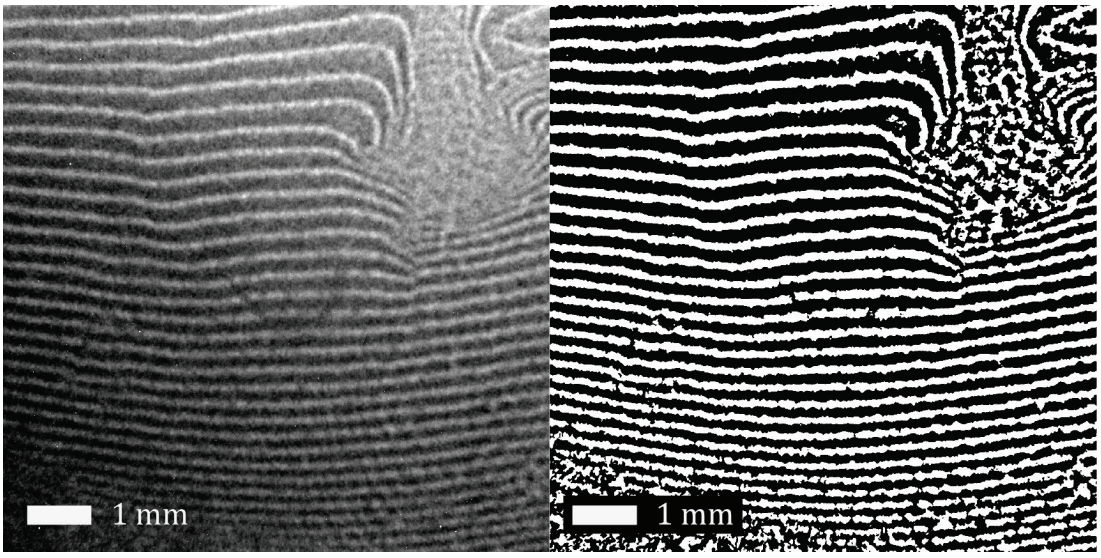

Figure 5.4. The effect of the pre-processing on the interferometry images. The raw image on the left is the same as in the upper-right pane of Figure 5.3; on the right is the same image after applying a despeckle filter and a local threshold tool.

5.1.3. Interferograms and shadowgraphy show the appearance of a shock in the nitrogen.

Interferograms were consistent with a shock wave expanding into the surrounding medium. See Figure 5.5 and Figure 5.6: in each, a graph of the density is presented. The laser strikes from the left onto (0 cm, 0 cm). The lineouts, shown below in each figure, are along the 0 cm horizontal chord, averaged over the nearest ten vertical pixels. Figure 5.6 shows the better data, but probably Figure 5.5 is more representative of the typical data: in both figures the images show a spike in the density at (0 cm, 0 cm) where the carbon rod stood prior to the laser ablation. This is likely to be a dense cloud of carbon plasma. At about 0.50 cm in Figure 5.5 and 0.65 cm in Figure 5.6 there is an arc of high density. I infer this to be a shock wave. The lineouts assist in the interpretation of the position of this shock, as well as the properties on either side, but also the lineouts highlight that the whole picture must be taken as a two-dimensional slice to reduce the impact of noise. A summary of the analysis from the interferometry data is given in Table 3 on page 109.

The effect of the magnetic field on the motion of the plasma can be quantified, within the ideal MHD assumption, by the value of the plasma beta. For the ram pressure the beta is

$$\beta_{\mathrm{ram}} = \frac{\rho v^2}{p_{\mathrm{mag}}} \approx 8\pi \frac{m_i n_i v^2}{B^2} \sim 10^3. \tag{5.1}$$

(The intermediate quantities are in CGS units.) As the shock slows down, β_{ram} drops to around 10, but this still indicates the ram pressure dominates. Therefore the fact that the imposition of the magnetic field is not observed to affect the shock morphology is unsurprising.

One important caveat is that the interferometry analysis is taken from the back side of the rod between 15 ns and 25 ns and therefore the shock properties at this time and position are only a proxy for the shock below the rod, later in its evolution; the values extracted here are used to constrain a simulation later. This approach follows from Gregori *et al.* (2012).

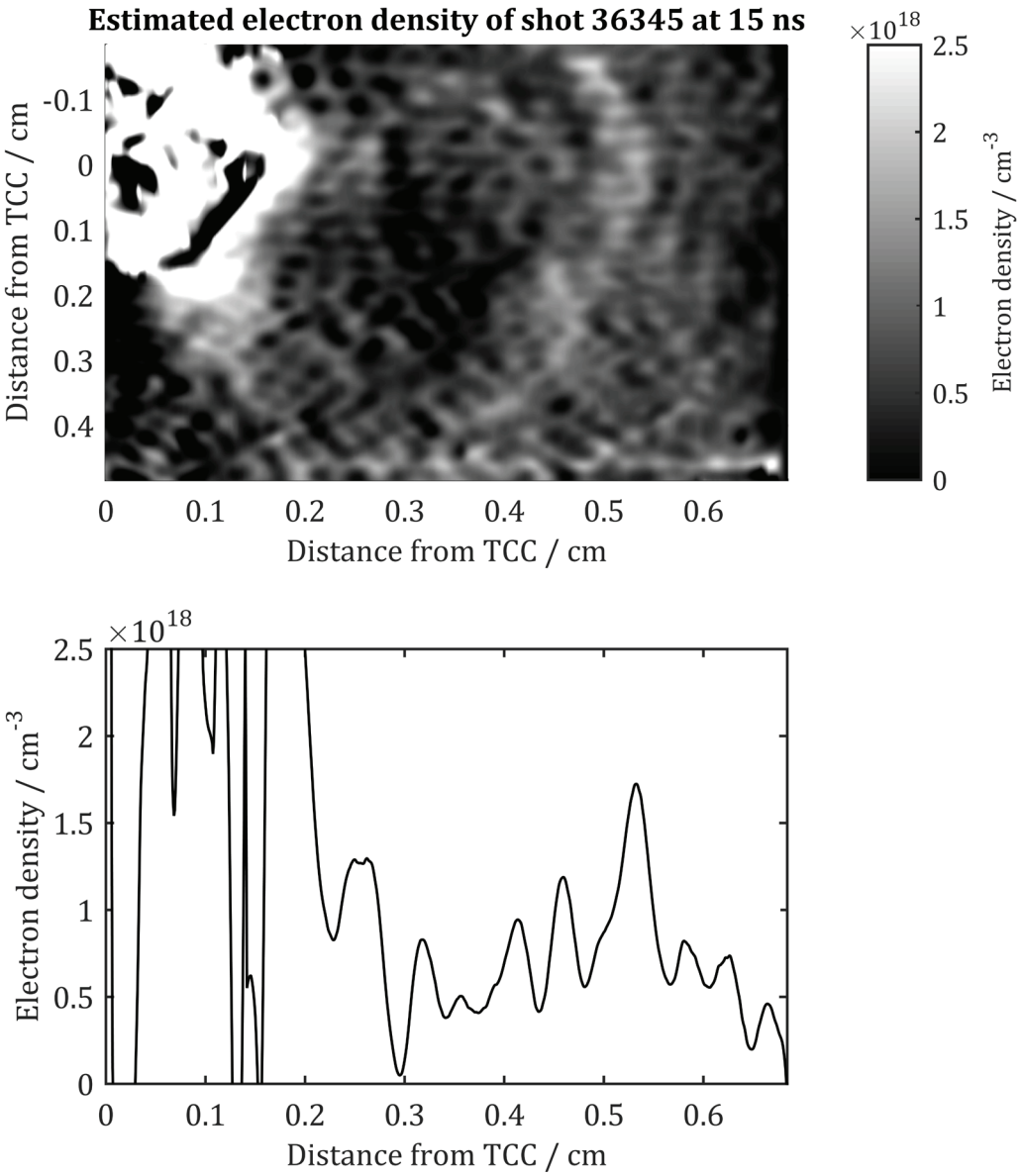

Figure 5.5. The estimated electron density at 15 ns, as computed from an interferogram. The laser energy was 480 J.

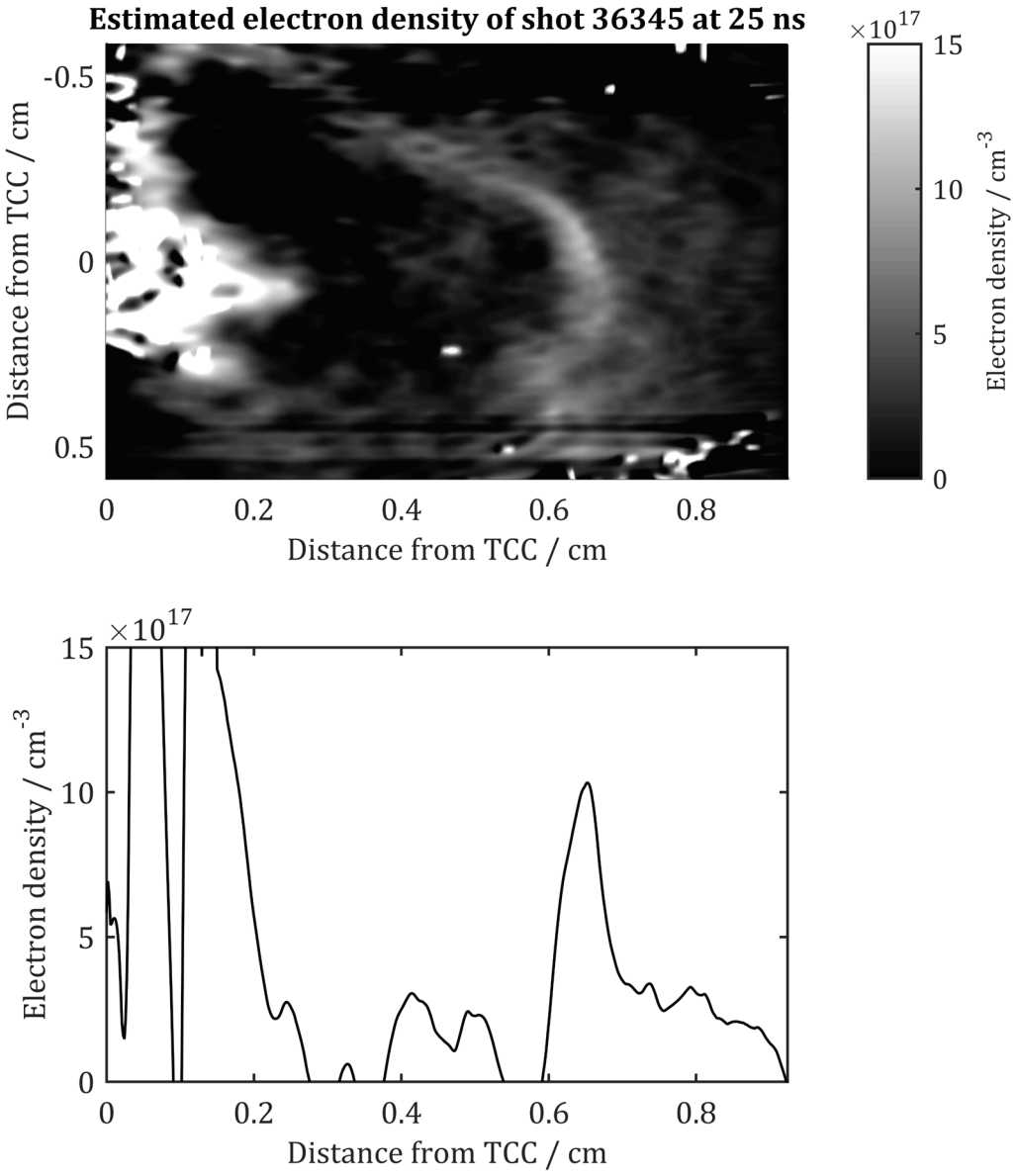

Figure 5.6. The estimated electron density at 25 ns, as computed from an interferogram.

The lineout is shown along the 0 cm horizontal chord, directly behind the laser strike position, averaged over the nearest ten vertical pixels.

Table 3. Estimates of shock position and electron density change in the GEKKO 2012 experiment from interferometric measurements, and inferences of shock speed.

	480 J ± 5 J		**840 J ± 15 J**		**1.28 kJ ± 15 J**	
With applied magnetic field?	**No**	**Yes**	**No**	**Yes**	**No**	**Yes**
At 15 ns						
Shock progress / cm	0.49	0.48	0.55	0.52	0.61	0.61
Sedov–Taylor quantity (est.) / cm $ns^{-2/5}$	0.17	0.16	0.19	0.18	0.21	0.21
Sedov–Taylor speed (est.) / μm ns^{-1}	130	130	150	140	160	160
Pre-shock electron density / 10^{18} cm^{-3}	0.6	0.5	0.7	0.5	0.6	0.6
Peak electron density / 10^{18} cm^{-3}	1.7	1.6	1.7	1.8	2.0	2.1
Compression ratio	2.8	3.2	2.4	3.6	3.3	3.5
At 25 ns						
Shock progress / cm	0.60	0.60	0.67	0.71	0.81	0.81
Sedov–Taylor quantity (est.) / cm $ns^{-2/5}$	0.17	0.17	0.18	0.20	0.22	0.22
Sedov–Taylor speed (est.) / μm ns^{-1}	96	96	110	110	130	130
Pre-shock electron density / 10^{18} cm^{-3}	0.4	0.5	0.3	0.4	–	0.5
Peak electron density / 10^{18} cm^{-3}	0.92	1.0	0.82	1.2	–	1.5
Compression ratio	2.3	2.0	2.7	3.0	–	3.0

Values are quoted to two significant figures, except the pre-shock density, which is difficult to estimate. For the meaning of the Sedov–Taylor quantity and speed, see section 2.1.3 on page 24. In one case the data were insufficient for the density reconstruction.

5.1.4. Optical streaked self-emission.

Streaked interferometry (Figure 5.7) shows an outgoing disturbance in the electron density. The streaked interferometry shows a horizontal slice at fixed position, and then the time proceeds down the image. (Actually the horizontal slice in the streak camera image represents a vertical slice through on the images above; the image is rotated before it reaches the camera.) The colours are reversed. The fringes are visible as vertical lines in the centre of the image. The laser flash is at the top right; then the image is dark until the probe laser illuminates the system and the shutter opens, where upon a diagonal density disruption in the fringes is visible. If the fringes were sufficiently well resolved, it would be possible to obtain an estimate of the density function with time, but regrettably they are insufficiently clear for such a task.

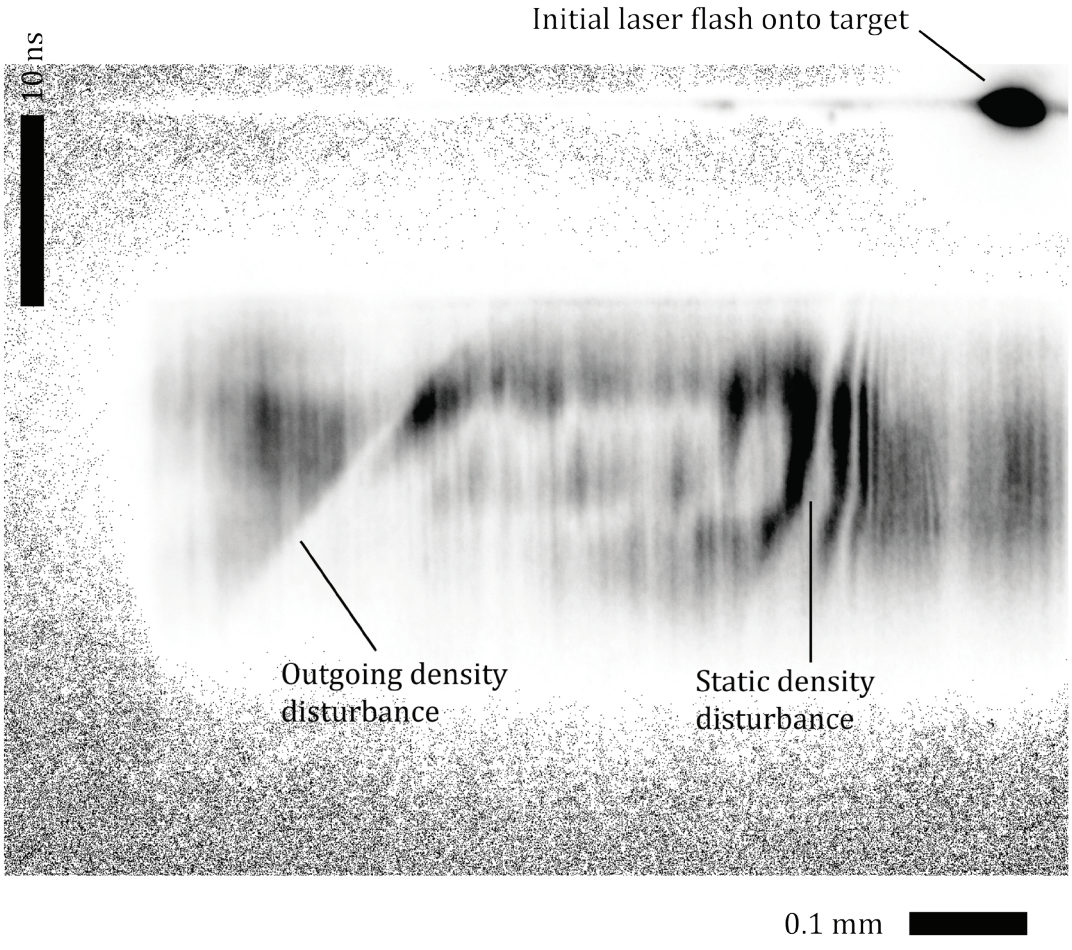

Figure 5.7. Streaked interferometry image, reversed colour: evidence of an outgoing feature is visible.

5.1.5. Bdot probe measurements.

Figure 5.8 and Figure 5.9 both present the raw signal (the voltage) recorded by the bdot probe; that is to say, this is the signal prior to any filtering or analysis. The axes have the meaning given in Figure 5.1, and the zero on the time axis is the laser-matter interaction time. In both cases the z signal is on average flat, but in Figure 5.8 there is much less noise than in Figure 5.9, where the data are overwhelmed for the first 200 ns or so with noise. The other channels, x and y show different behaviour; in both cases there is a rise and fall of the voltage over about 1 μs, but in the case of Figure 5.9 this is much more pronounced with an early peak at about 400 ns. The x and y axes appear roughly correlated in both graphs with the z axis behaving separately. In the case of both figures, if there is any high frequency behaviour it is largely occluded by the noise.

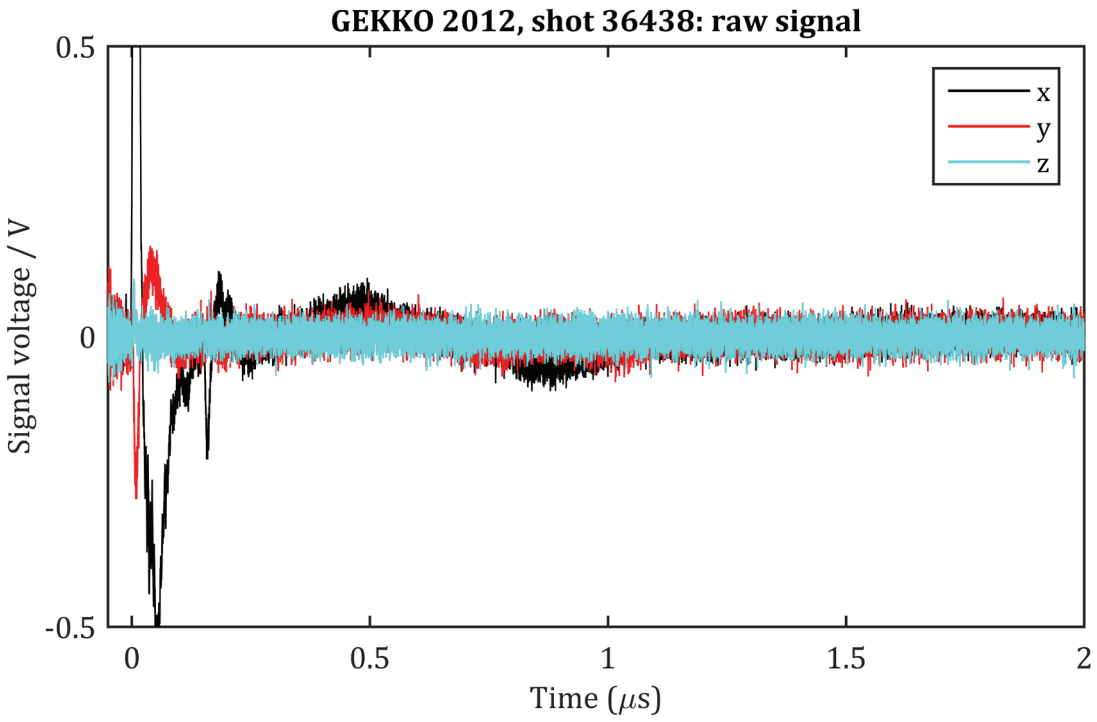

Figure 5.8. Raw data from the bdot probe (no imposed field, 1.3 kJ driver).

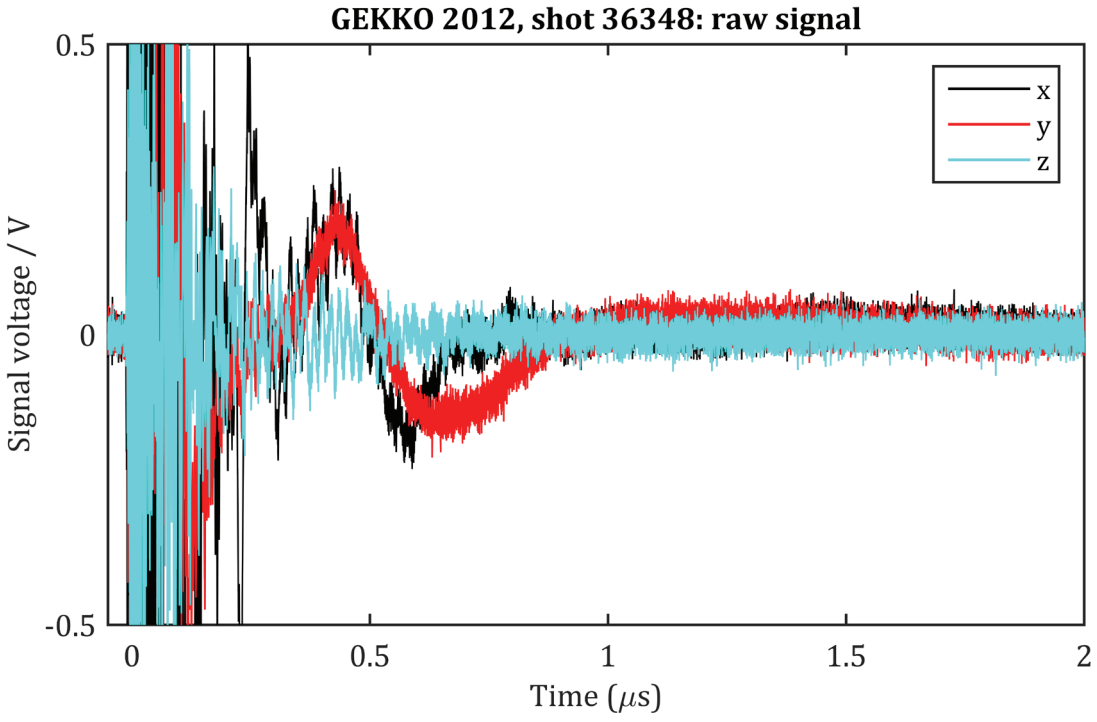

Figure 5.9. Raw data from the bdot probe (with imposed field, 1.3 kJ driver).

5.1.6. Wavelet coherency analyses of the bdot probe observations.

Description of method as applied to this dataset.

The coherency analysis of the bdot probe data is presented in Figure 5.10; the coherency estimate is taken between the two axes orthogonal to the shock travel direction (and, where imposed, the background magnetic field direction). This means the data are collected on the x- and y-axes of the probe as defined in Figure 5.1.

The description that follows on is given in reference to Figure 5.10 on page 116. I shall begin with a summary explaining the means by which the data were processed, then how each graph was made, and finally what I believe the physical implication to be.

To produce each graph, I process the data recorded on two orthogonal bdot probe coils under the method explicated in Part 3.1, in particular under equation (3.9) to give the **B** field as a function of time, projected into the x and y directions (each of which is orthogonal to the shock-travel direction at the probe: see Figure 5.1 on page 101). The vertical component (the z-axis, which is the shock travel direction) is disregarded. Then, I apply the signal analysis techniques I discussed in Part 4.4 to give a set of three wavelet coherency graphs. In the left column, the data presented were taken with no magnetic field imposed; and on the right, the background dipolar background field was in place.

The design of graphs.

Figure 5.10 on page 116 shows data taken with a laser energy of 1.2 kJ. It is at this energy that the distinction between the case with no imposed field (left column) and the case with the imposed field (right column) was most clear. In each graph, the vertical scale represents the angular frequency of the detected signal, and the horizontal scale shows the evolution of time since the laser pulse was fired.

The graphs in the uppermost row, that is, subfigures (a) and (b), show the cross wavelet coherency, as defined in section 4.4.7, in modulus. The bright colours depict regions of high common power between the two axes of the bdot probe. The power is measured on a log scale, shown in decibels, relative to the noise floor.

The graphs in the middle row [subfigures (c) and (d)] show the phase lag between the signals recorded on the two orthogonal axes, ranging from $-\pi$ to $+\pi$. In order that the graph not be too overwhelming, I have suppressed regions where the signal power on either coil falls below what I estimate to be the detection threshold for the bdot probe at the relevant frequency. Those areas are shown faded on the graph.

In the final, lowermost row [subfigures (e) and (f)], I present the same data as in subfigures (c) and (d), except that now I only highlight regions where the phase lag between the two signals is at $-\pi/2$, within a tolerance of $\pm\pi/6$.

The features that are visible on the signal power graphs (a) and (b); a description thereof.

In both plots (a) and (b), there is evidence of a bright pulse at early time ($t < 0.1\,\mu s$). The pulse is relatively wideband in both subfigures, although brighter in graph (b). In (a), there is also a kind of echo of the early noise occurring at about 0.1 μs. If this feature is present in (b), it is overwhelmed by another signal, which occurs very brightly from 0.0 μs until about 0.2 μs. In (b) there is also a clear band, extended from early time until about 1.0 μs, occurring in a narrow band approximately between 50–70 MHz, with power concentrated at 60 MHz. This feature is completely missing in figure (a). The peak power in this band is of order 40 dB, gradually falling away into noise.

Subfigure (b) also shows the presence of some 'spikes' that periodically extend off the tail upwards. From analysis with wavelets of narrower frequency discrimination, I believe these are artefacts of the wavelet transform, where the 60 MHz band has significantly higher power than the local average and is 'leaking' upwards.

The phase differences between orthogonal magnetic field measurements, shown in subfigures (c) and (d).

To determine the nature of this common coherence, let us now look at the phase lag between the two orthogonal bdot axes in the case of both experiments. Subfigure (c) again shows the case with no magnetic field; the low-magnitude data close to the noise floor have been suppressed. In general it is difficult to discern much in the way of a pattern, although the early spike has some consistent phase lag.

A similar story applies in subfigure (d), but it is clearer that the band described of high power in (b) has a consistent phase throughout, suggesting that it is not merely a region of white noise but was generated by some physical process. The lag is approximately $\pi/2$ for much of the band, suggesting that the fronts here are right-hand circularly polarized in the bdot probe's frame.

Features of $\pi/2$ phase lag as highlighted in graphs (e) and (f).

In figures (e) and (f) I have suppressed all points from (c) and (d) by fading, except those displaying lag of $-\pi/2 \pm \pi/6$. Subfigure (e) is now largely empty, although there is common power in this phase lag at times before 0.1 μs. In subfigure (f), however, there is a clear sequence of three right-hand polarized bursts at about 60 MHz, with a bandwidth of perhaps 20 MHz. The bursts fade before 1 μs.

5.1.7. Summary of the 2012 GEKKO experiment.

I produced shocks in nitrogen with a driver at multiple energies. I characterized the shock through optical diagnostics at early times. The imposition of a weak background magnetic field did not affect the shock propagation but it did affect the generated magnetic field configuration. There is evidence of a right-hand polarized mode at about 60 MHz in only the field-imposed case.

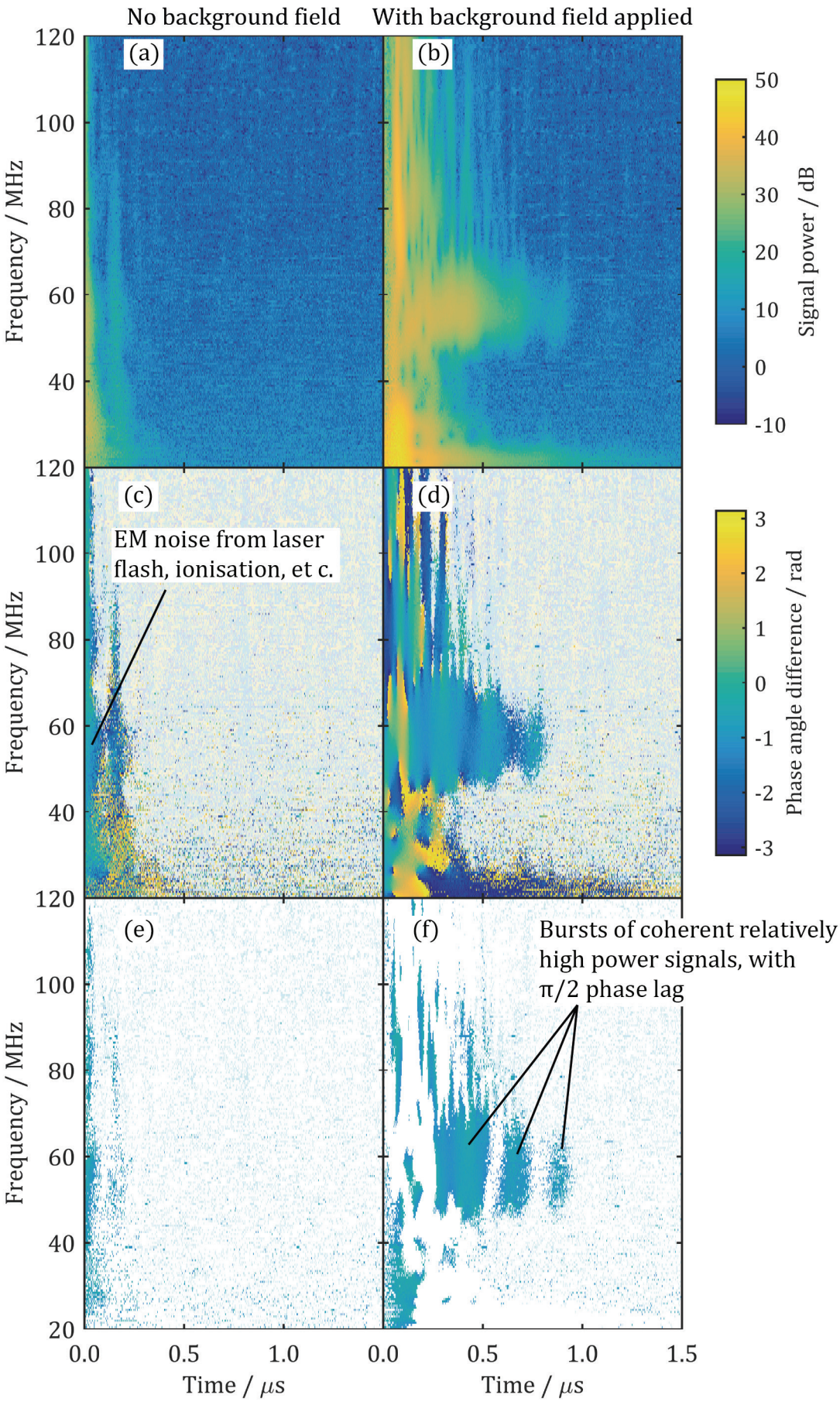

Figure 5.10. The coherency analysis of the bdot probe data taken at 1.3 kJ.

5.2. SECOND EXPERIMENT AT THE GEKKO FACILITY (2014)

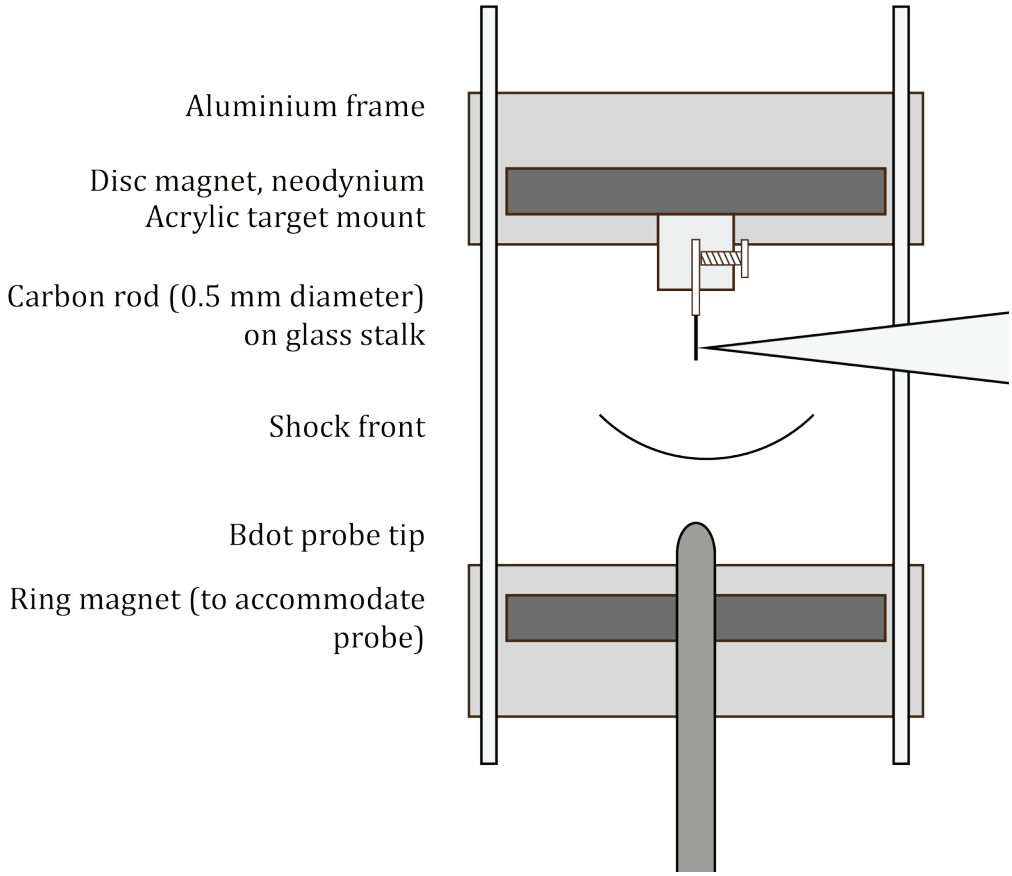

Figure 5.11. A schematic of the experiment performed at the GEKKO facility in 2014.

A source of uncertainty in the first experiment at the GEKKO facility was the non-uniformity of the imposed magnetic field, both in terms of magnitude as the shock progressed, and the degree of curvature. It seemed to me that the variance in the field was a confounding variable that could be readily eliminated (see Figure 5.2 on page 102). Therefore, I designed a Helmholtz-like array consisting of a pair of disc magnets surrounding the target, intended to produce a region of straight field lines. The lower magnet has a 1 cm diameter hole drilled through it to accommodate the passage of a bdot probe. In this experiment I used only one driver energy value, 360±20 J, requiring three driver beams in the cone per shot: using only three beams from the twelve-beam array enabled me to take more shots without waiting for amplifier cooling. During the experiment, I varied the gas pressure and the distance between the bdot probe and the

target. The shock parameters were observed with optical interferometry and shadowgraphy; framed self-emission showed the disintegration of the carbon target.

5.2.1. The design of the 2014 experiment.

I designed a target assembly in which the magnetic field would be uniform and relatively strong, compared to the previous experiment—in which the field had been dipolar, weakening as the shock progressed and also diverging spatially. The assembly consisted of two neodymium-boron-iron magnets in a Helmholtz configuration; modified by the introduction of a small hole in one of the magnets to accommodate the bdot probe. A schematic of the design is presented in Figure 5.11 above. The field was measured to be 5000 G with a Hall probe at several points along the rod axis within 3 cm of the target-laser interaction point. The GEKKO laser irradiated a carbon rod with 360 J of 321 nm light, prompting the generation of a shockwave into the surrounding nitrogen. The nitrogen pressure, before the laser fired, was varied between 1.3 mbar and 6.6 mbar.

Side-on optical interferometry (of the Nomarski design) and shadowgraphy was available from a probe beam passing through the target orthogonally to the principle driver cone (*i.e.*, into the page in Figure 5.11). That common probe line also supplied the self-emission diagnostics (with appropriate filters to exclude the laser light): the full diagnostic set up is shown in Figure 5.12.

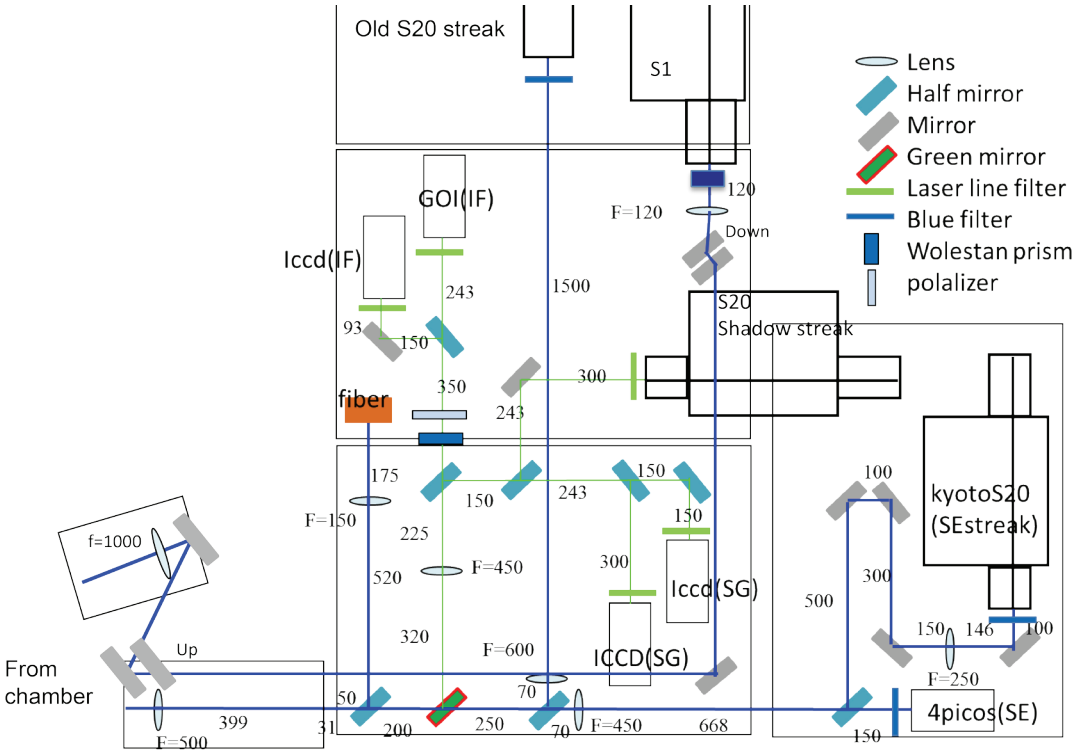

Figure 5.12. The diagnostics set up for the 2012 and 2014 experiments at the GEKKO facility. (T Morita, private communication.)

5.2.2. Optical emission images.

Using a framing camera I obtained time-resolved self-emission images, showing the disintegration of the carbon rod and an outgoing arc: see Figure 5.13. These images are time-resolved pictures of the radiation emitted by the plasma, without backlighting. The exposure time in each case is 0.25 ns. The framing camera consists of a number of independent CCDs each supplied from a common optical line; the camera thereby enables one to capture multiple time-resolved images of the same shot. At 5 ns, multiple images appear of a white-hot target, but this is likely due to internal reflections of the same image. By 20 ns the ghost reflections have vanished. At about 25 or 30 ns a clearly distinguished glowing front is visible moving away from the target. Figure 5.14 shows the position of this outgoing arc. The results suggest it is, between 25 ns and 50 ns, approximately a Sedov–Taylor shock.

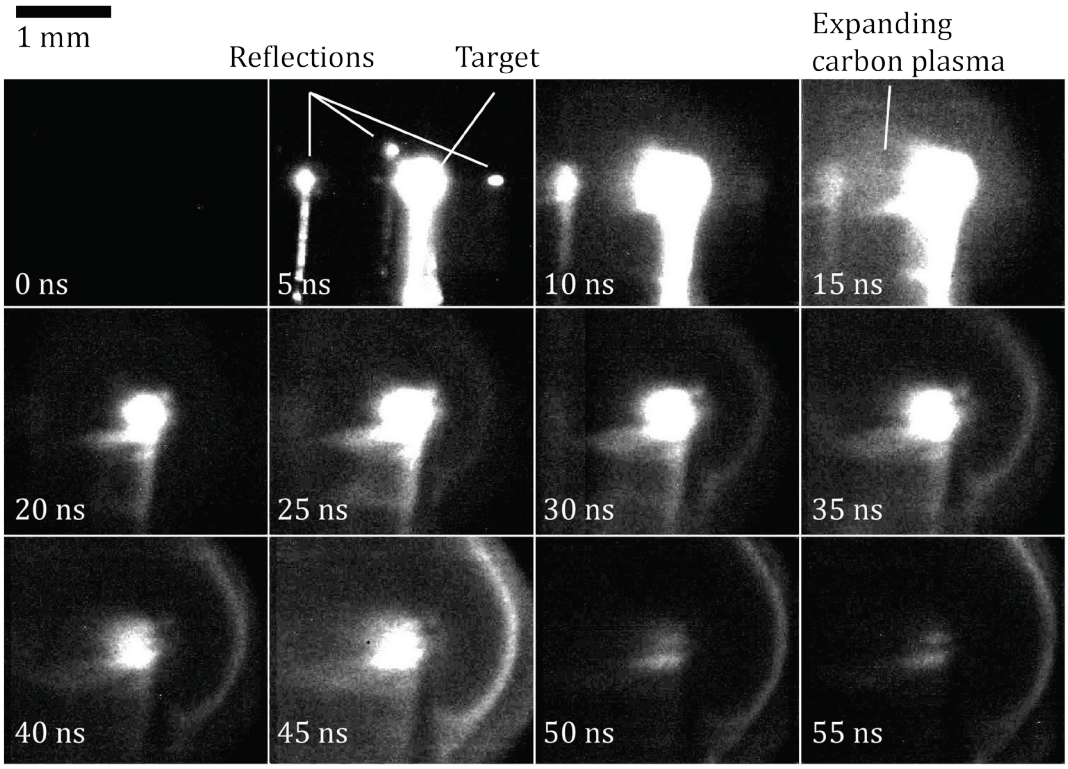

Figure 5.13. A series of self-emission images captured of a shock front evolving from a carbon plasma and expanding into the surrounding nitrogen medium.

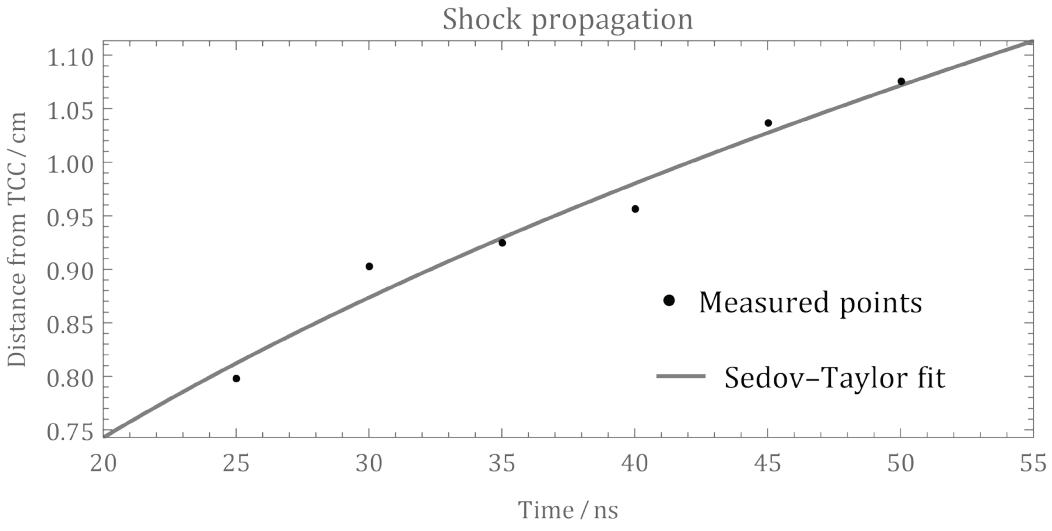

Figure 5.14. The horizontal position of the outgoing arc, with a Sedov–Taylor curve fitted.

5.2.3. Interferometry through optical probing.

At 15 ns and 25 ns, interferograms are also captured. An example of such an interferogram is presented in Figure 5.15. As in the 2012 experiment, the interferograms are interpreted to provide electron density information at two time points, which is later used to constrain simulations. The results are found to be in line with the 2012 experiment at the same energy and fill pressure values.

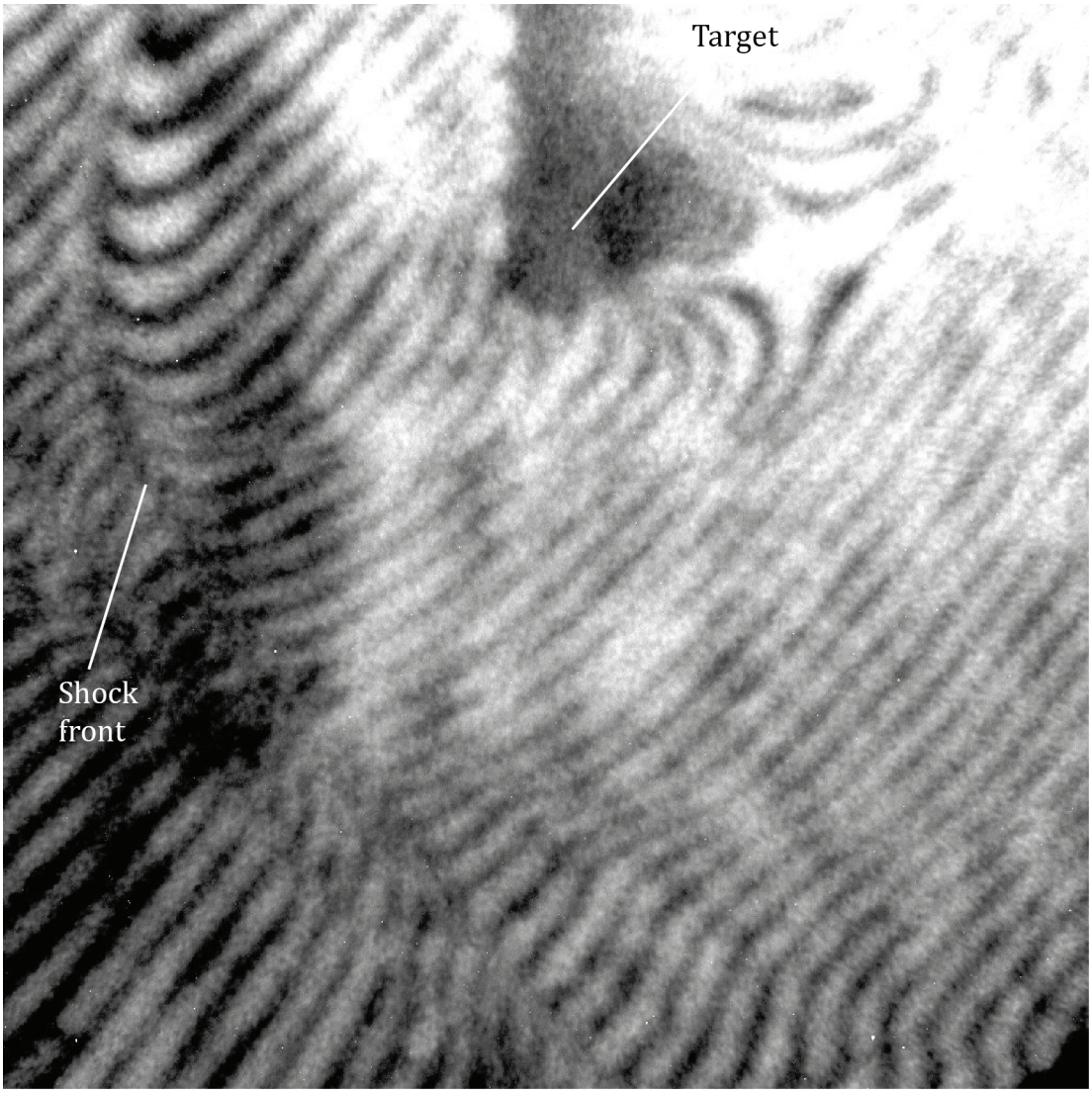

Figure 5.15. An interferogram showing the emergence of a shock front propagating into the surrounding nitrogen media.

5.2.4. The magnetic field signals recorded by the bdot probe.

The bdot probe recorded signals for all shots. Two examples are given: see Figure 5.16 and Figure 5.17. Figure 5.16 is at 25 mm distance and shows a slightly weaker field, peaking at about 30 gauss, whereas the other figure has a peak at about 40 gauss, and reaches its peak sooner. This is consistent with a Biermann battery mechanism driving the field generation in or just behind the shock front.

In Figure 5.18 on page 124 I show the coherency analysis from two datasets equivalent but for the presence of an imposed straight field. This time there is no evidence of a narrowband signal.

5.2.5. Summary of the 2014 experiment

I produced and characterized shock waves at the GEKKO facility. I used a Helmholtz array to impose a consistent 5000 gauss field on the target for some shots. The bdot probe indicated the generation of magnetic field up to about 40 gauss.

However, there was no evidence of right-hand polarized waves as we saw in the 2012 experiment. This was also the case when no imposed field was in place. The reason for the difference in results between the two experiments will be investigated in Part 6.3 on page 146.

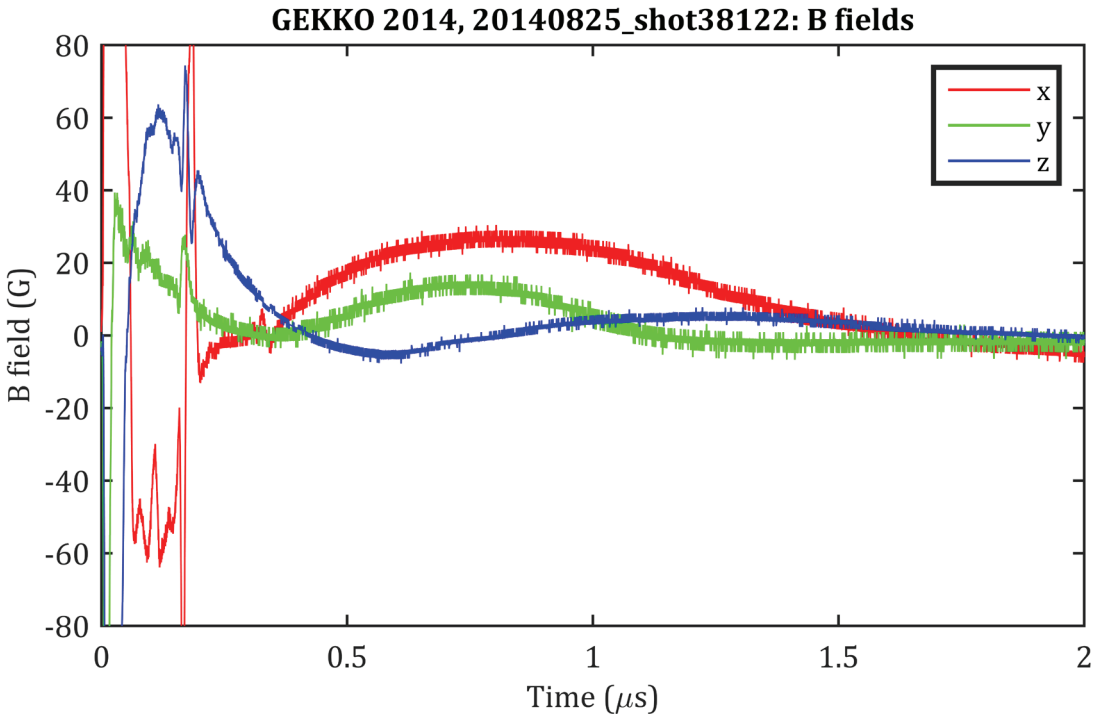

Figure 5.16. Magnetic field measurements from bdot probe (with imposed field, 360 J driver, 1 mbar back pressure, probe at 25 mm distance).

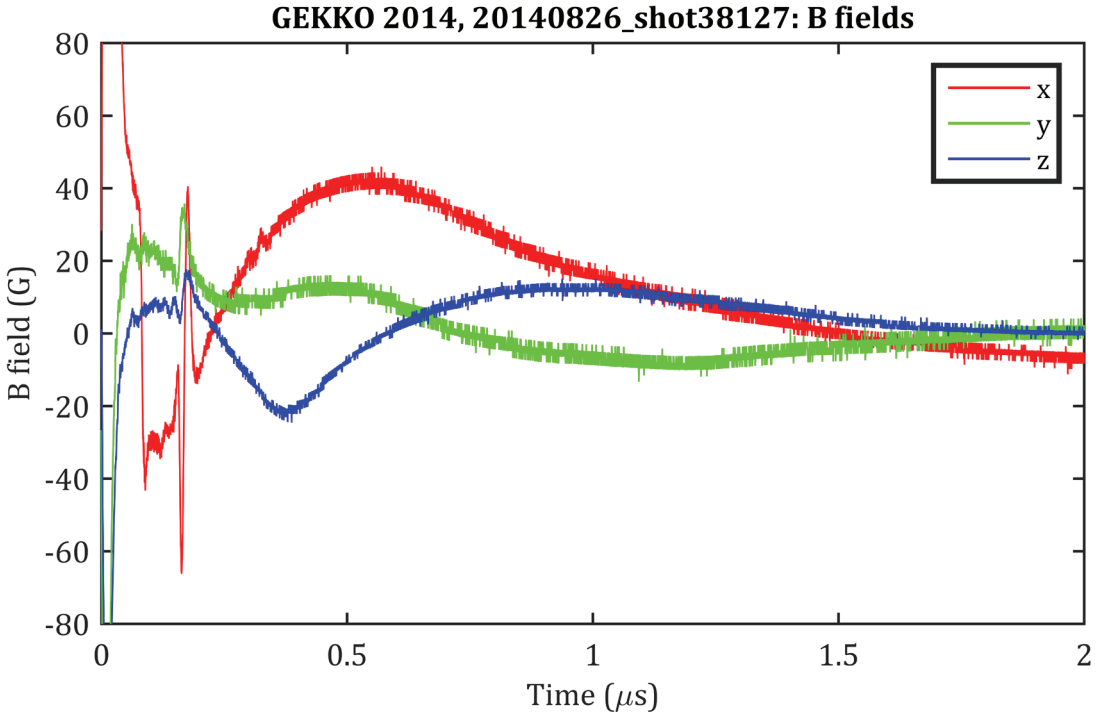

Figure 5.17. Magnetic field measurements from bdot probe (with imposed field, 360 J driver, 1 mbar back pressure, probe at 20 mm distance).

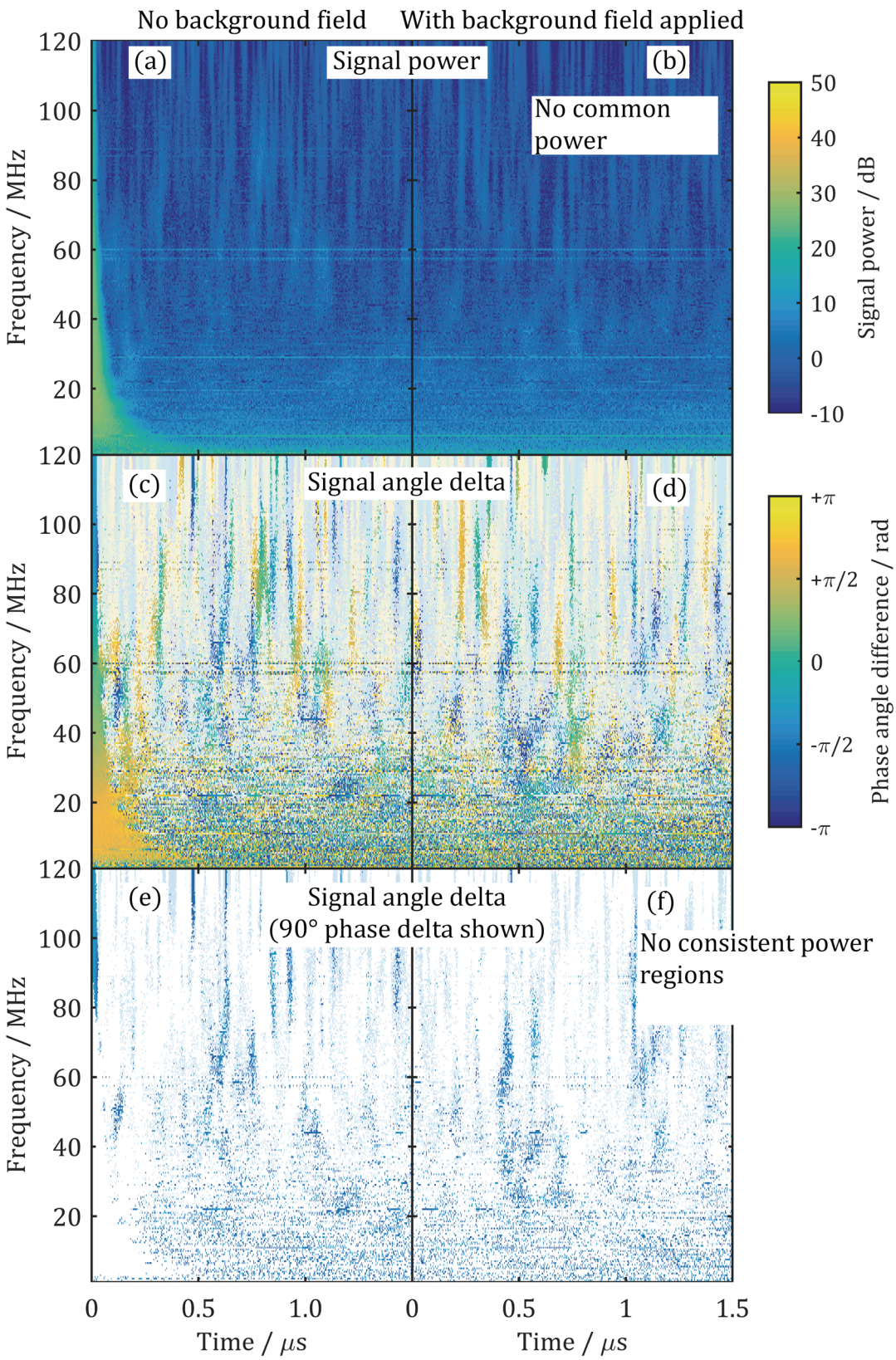

Figure 5.18. The coherency analysis of the bdot probe data from the 2014 experiment.

5.3. SPECTROMETRY OF ELECTRONS

This experiment was principally conceived to develop our study of magnetic field amplification through turbulent plasma flows; that element is discussed by Meinecke *et al.* (2014). The component I discuss here was an attempt to detect any electrons accelerated by the process of diffusive shock acceleration. However, such an ambition was not likely to succeed given the plasma conditions (Reville *et al.*, 2013). Instead, I used the data produced to look at the electron energy spectrum produced during the experiment.

5.3.1. Design of the experiment.

The experiment was conducted in Target Area West in May 2012 at the Vulcan laser facility in Oxfordshire, United Kingdom. A target, usually a single carbon rod, is heated by the illumination of up to three long pulse beams from the Vulcan laser. The heater beams were arranged at a ninety-degree angle to the detector line of sight. On some shots, two targets were used, with the second target heated from the opposite side; but the spectrometer was not adjusted. Here, however, I look only at the high-energy electrons produced. For the detail of the electron spectrometer's operation, see Part 3.3 and in particular Figure 3.10 on page 59.

We used a great variety of target configurations: sixty-six shots with single 'slab' targets; fifty-eight shots with double targets; sixty-three single 500 μm diameter carbon rod targets, of which thirty-one included a grid intended to perturb the outbound shock front; and in all but a minority of cases there was some level of gas fill.

5.3.2. Example image plates.

An example of a scanned image plate, after it is converted to PSL values, is given in Figure 5.19. The dark regions represent higher PSL values. The area between the magnets is isolated, averaged and then the value is plotted as a function of distance along the image plate. The image has been converted to PSL (photostimulated luminescence) values by proprietary software supplied with the image plate scanner; the black areas indicate the deposition of charge (or x-rays) and the white areas represent its absence.

The outline of the magnets is marked in black dashed lines. The region between the magnets, from which the energy spectrum shall be estimated, is shown in white dashed lines.

In Figure 5.20 I show the relevant part of the image plate zoomed in. The colour scale is different from the previous figure. There is a band of dark corresponding to a higher electron density. The average value of the PSL count is taken as a function of distance and presented in Figure 5.22.

Two examples, both from carbon rod targets, are presented in Figure 5.21 (no gas) and Figure 5.22 (1 mbar argon). The shots without gas appear to be a lot 'messier', with lower values in general. The shots taken with a background gas fill have a higher PSL count in general—suggesting a greater number of heated electrons—and they follow a smooth curve with a peak at 0.5 cm. This suggests the presence of a gas fill greatly increases the number of heated electrons.

In Figure 5.23 and Figure 5.24 I have applied (3.30) to obtain the electron count with energy. The presence of an energy 'cut off' at 40–50 keV is reproduced in all data; there is, if one moves from right to left, a precipitous decline in electron count at this energy value. The predicted 'minimum energy' from the calculation discussed in section 3.3.2 is 36 keV, suggesting that the approximation is not very reliable. Probably the effects of fringe fields around the yoke, which were previously neglected, are responsible for this deviation.

Integrating over the energy in the gas-filled case gives a total electron count of about 10^8 electrons; these are collected by a detector through a slit of 0.2 cm^2 area placed 30 cm distant from the target. If the electron profile is uniform over that area, it suggests approximately 10^{11} electrons were emitted with energies in excess of $\sim$ 50 keV and below 200 keV.

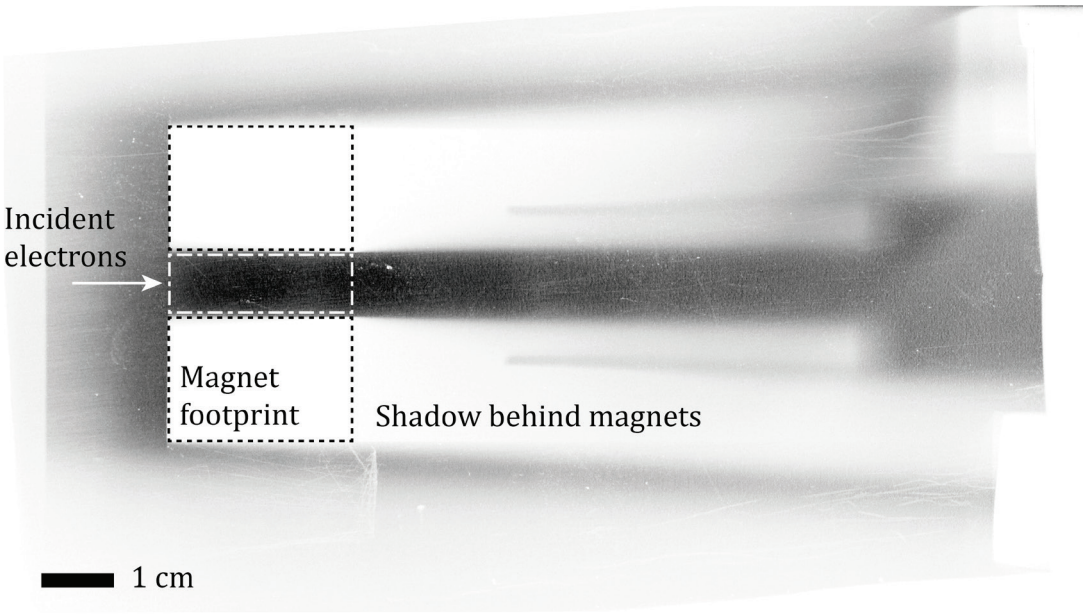

Figure 5.19. A false colour scan of an imaging plate, after exposure during the experiment.

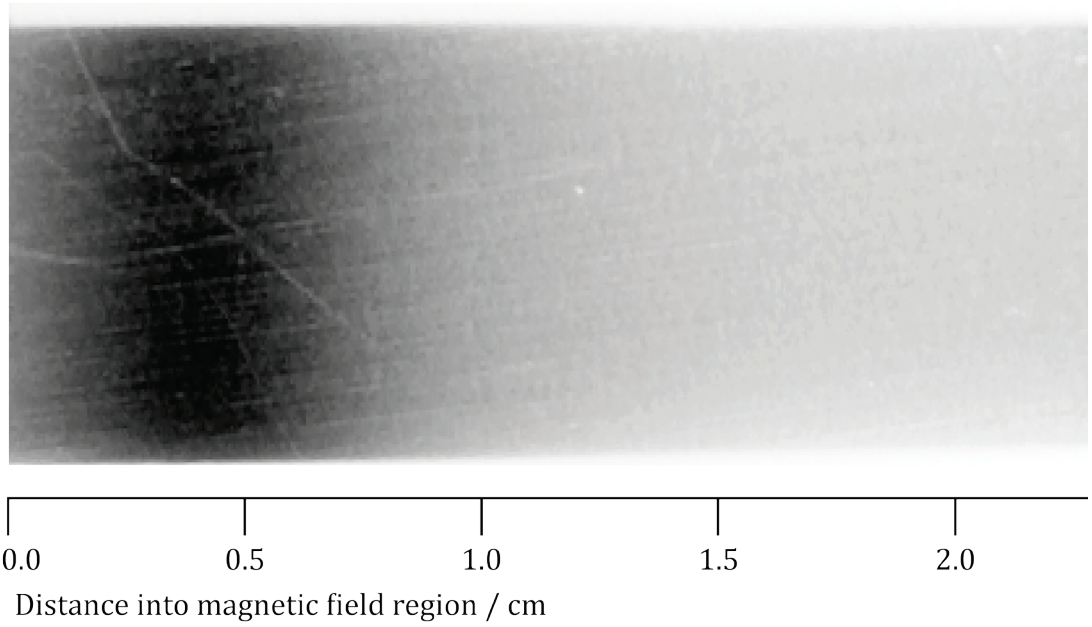

Figure 5.20. The PSL level in the magnetic field region (darker corresponds to higher electron density).

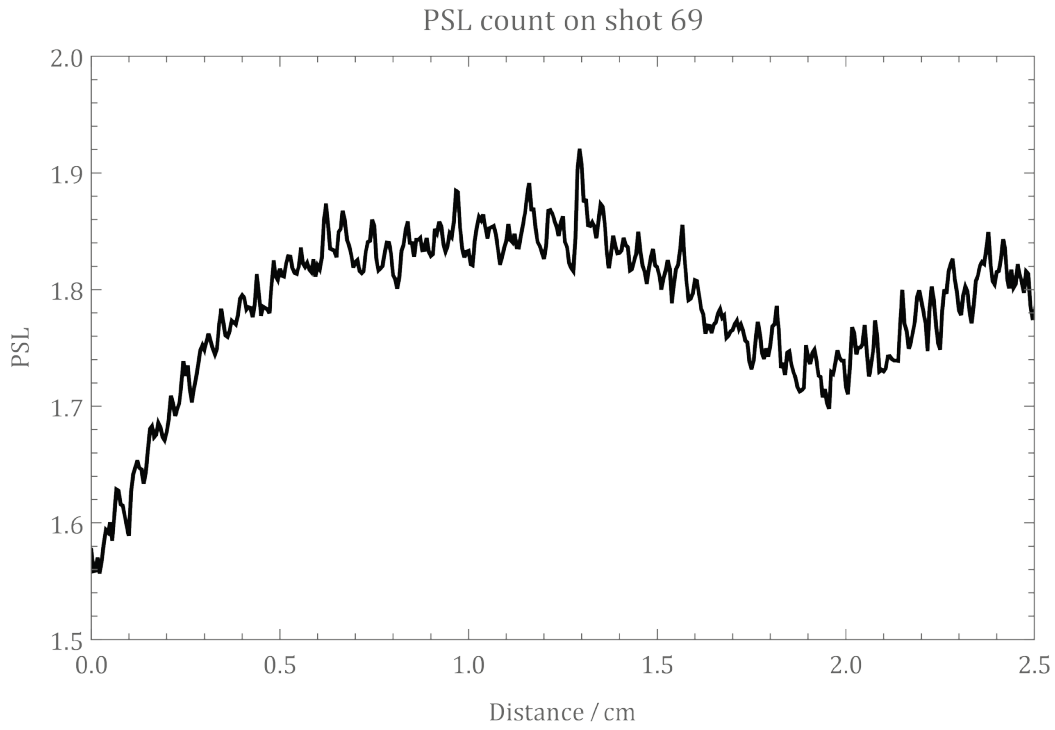

Figure 5.21. Lineout from an image plate. This shot had no background gas fill.

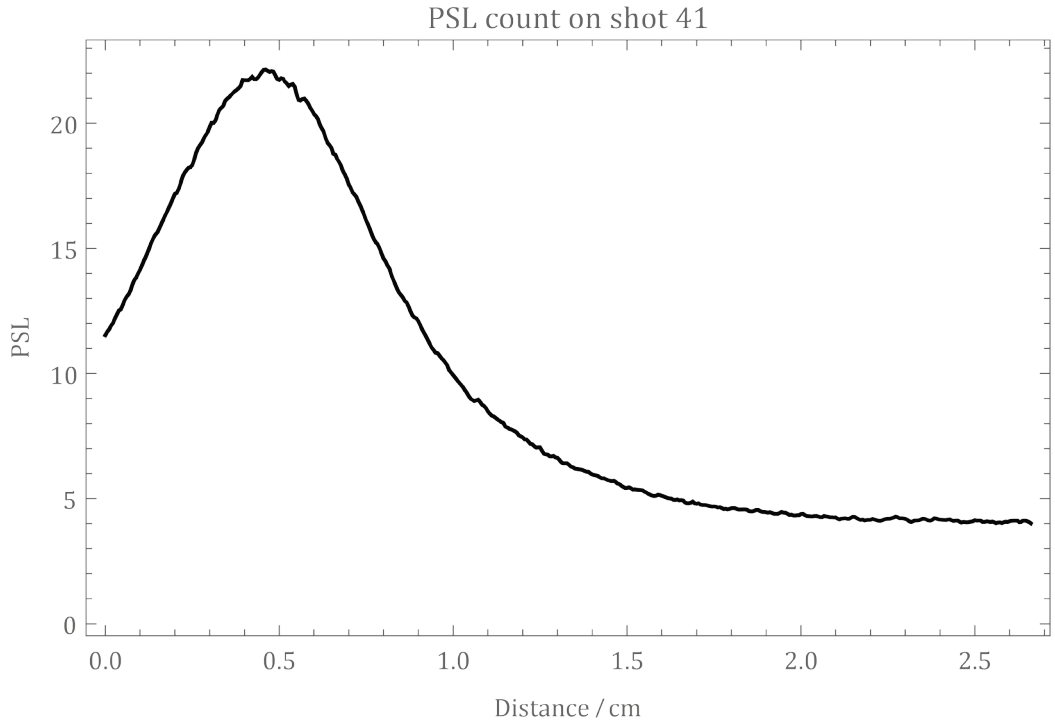

Figure 5.22. Lineout from an image plate. This shot was taken in the presence of 1 mbar of argon gas.

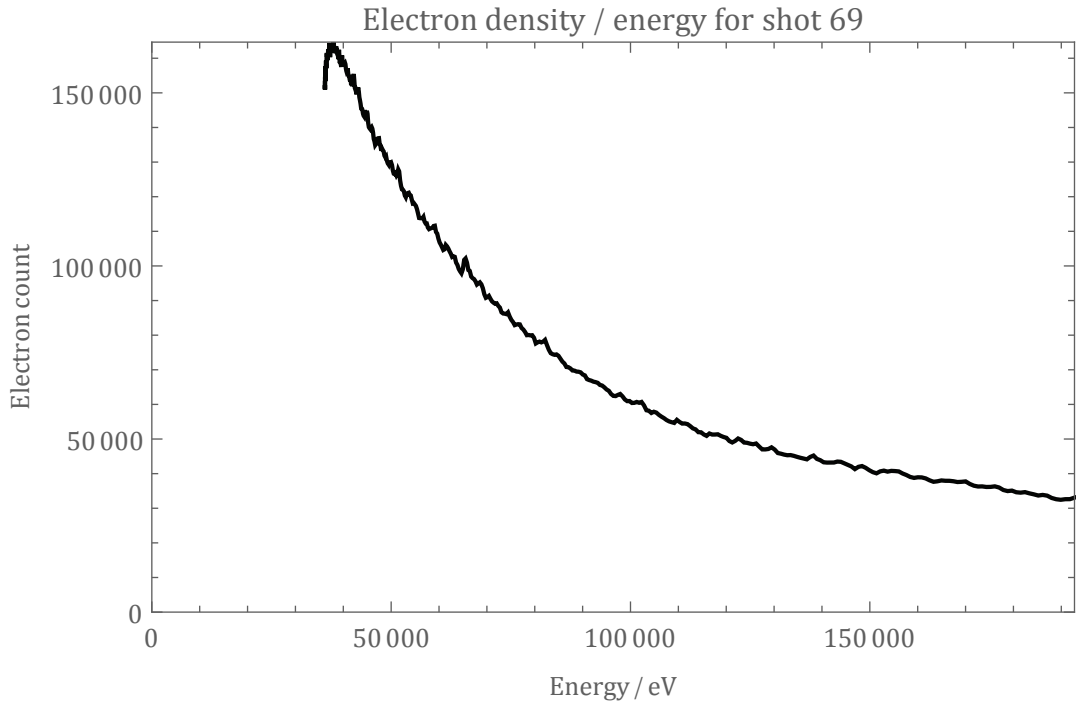

Figure 5.23. Conversion to charge line density per energy. This shot had no background gas fill.

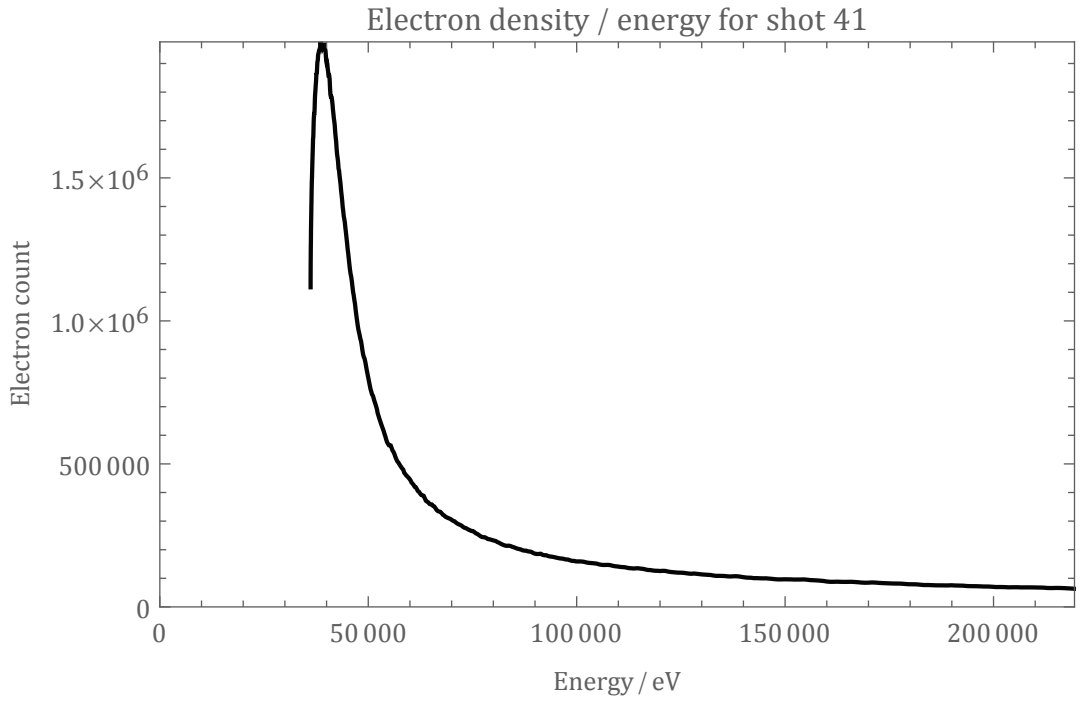

Figure 5.24. Conversion to charge line density per energy. This shot was taken in the presence of 1 mbar of argon gas.

5.3.3. The results in summary.

There is a clear difference between shots that have a gas fill and those which do not; since the free electron count is higher at the measured energy values when the gas is present, it suggests that the damping effect of the gas is not particularly important but rather the gas acts as a source of charged electrons. However the limitations of the diagnostic, in particular the energy detection range and the time-integrative nature, and the probable presence of fringe fields compromising the accuracy of the count, do not allow a reliable interpretation of the data that can be made useful for the experiment at times following the laser-matter interaction.

5.4. LASER-DRIVEN COILS

This experiment was undertaken at the LULI facility, École Polytechnique, France in May 2014. Essentially, a high power laser drives electrons from one of a pair of parallel discs to the other, establishing a high potential difference between the two surfaces. A return current then flows, to neutralize this charge accumulation, through a wire connecting the two plates; and this wire is arranged in a single loop. A high **B** field arises through the axis of the wire loop, of the order of a few hundred tesla, persisting for a few nanoseconds.

The growth and decay of a field on this time scale, was at the limit of the probe's theoretical temporal response. Therefore, the experiment allowed me to test the bandwidth of the bdot probes by reference to ultra-fast bdot probes supplied by *le Commissariat à l'énergie atomique et aux énergies alternatives* ('the CEA').

5.4.1. The motivation for the experiment.

The generation of magnetic fields approaching 1 kT is of interest to numerous communities, including not only high field physics in abstract (Portugall *et al.*, 2013) but also applications such as suppression of electron heat conduction in the inertial confinement fusion scheme (Chang *et al.*, 2011), in the validation of nuclear modelling (Schielke *et al.*, 2003), in probing the mechanism of superconductors (Hunte *et al.*,

2008), and in laboratory astrophysics studies (Courtois *et al.*, 2004). However, reaching fields in excess of 300 T is beyond the range of conventional capacitor-driven electromagnets (Herlach, 2002), and other methods, such as driving flux compression with chemical or even nuclear explosives (Neuber & Dickens, 2004), have obvious practical shortcomings.

Therefore, producing a stable, long-lived (10s ns) magnetic field through a compact, laser-driven device has clear advantages to many communities, in particular lab astrophysics. However, previous experiments using the capacitor-coil target design (I describe the design below) have failed to characterize the field geometry well, making estimations of the maximal field strength uncertain (Fujioka *et al.*, 2013). Therefore, in this experiment we intended to measure the field in several places, though several diagnostics, to constrain better our model of the field.

I implemented a three-axis bdot probe on this experiment to complement several other diagnostics (CEA probes, Faraday rotation, proton deflectometry). Here my intention is not to concentrate on the other diagnostics and the experiment as a whole, but rather to examine the temporal response of the bdot probe to a field whose rise time is on the order of nanoseconds.

5.4.2. The target design and the driver parameters.

The target consists of two parallel metallic discs, conjoined with a metal wire arranged in a small loop. A high power long pulse laser system delivered 500 J (±25 J) of 526 nm light onto the target over 500 ps, reaching an estimated focal intensity of 3×10^{17} W cm^{-2}. The laser is brought to focus on the rear disc's front surface, passing through a hole in the forward disc. The laser-plasma interaction on the target surface drives a population of hot electrons from the rear disc and onto the front disc, establishing an electric potential gradient between the two discs. In (i), the rear disc is illuminated through the hole of the front disc. In (ii), the laser plasma interaction has driven a collection of electrons onto the front target, creating a charge imbalance. This charge separation creates a strong electric field between the plates. In (iii), the charge imbalance has driven a return current through the wire loop, creating a magnetic field.

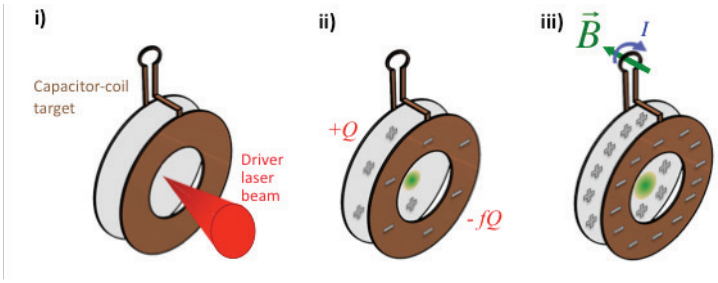

Figure 5.25. The target design and evolution of the LULI experiment in 2014. From Santos *et al.* (2015).

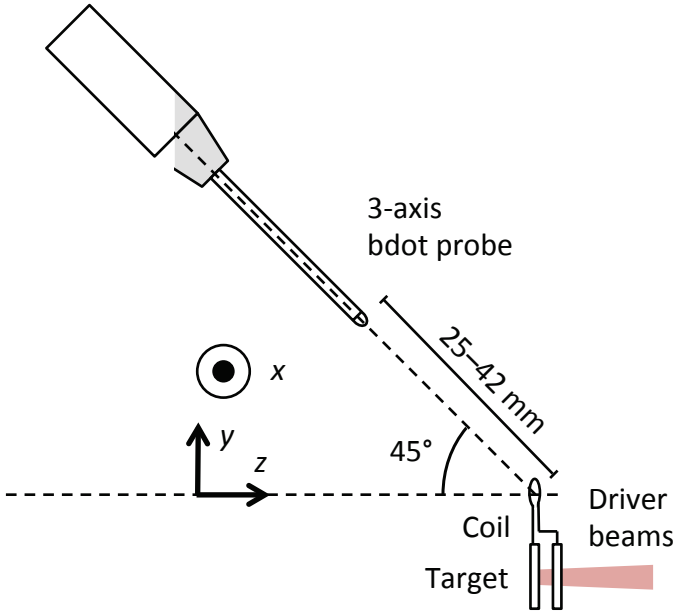

Figure 5.26. The position of the bdot probe (not to scale).

5.4.3. Magnetic field measurements from the bdot probe.

The probe is positioned at either 42 mm or 25 mm from the coil centre (see Figure 5.26). From previous experiments of this nature (Daido *et al.*, 1986; Fujioka *et al.*, 2013) we expect the field lifetime to be on the order of 10 ns or less. The multi-axis probe records a peak in the magnetic field along the coil axis as expected, with a full-width at half-maximum (FWHM) size of 10 ns. Data from other measurements suggest a lifetime of about 5 ns (full width at half maximum), so from this we might conclude that the probe is reaching the bandwidth limit of the probe (see Figure 5.27).

5.4.4. Summary of results.

The data from the bdot probes in this experiment were compared against data collected from the other probes provided by the CEA. Faraday measurements were collected on a streak camera but were not available at the time of writing. It is found that the CEA probes, which have a bandwidth exceeding 2.5 GHz, detected the field life time of about 5 ns in contrast with our measurement of about 10 ns FWHM. It was necessary to apply a high pass, first order Butterworth filter with cut off frequency of 8 kHz to the dataset before processing. The value of the cut off frequency was found by an interpolation process. Assuming that the data from the CEA probes are correctly interpreted, this suggests our bdot probes have a response function preventing resolution below about 10 ns.

We also compared the detected, peak magnetic field at the bdot probe with the magnetic fields recorded by other detectors. A three-dimensional magnetostatic model of the target was constructed, which, given a specified flow of electrical current through the target and wire loop, simulates the magnetic field that results. A copy of the model was produced for each diagnostic; the only difference being that the magnitude of the electrical current through the wire loop was adjusted in each case such that the field it produced matched the measured field at the detector position. The magnetostatic model was designed and implemented by Mathieu Bailly-Grandvaux of the University of Bordeaux.

By this process I compared the data from the bdot probe with the data recorded by other probes placed in other positions. I found that with an appropriate high pass filter of $\sim$ 8 kHz, the match with the alternative probe was good.

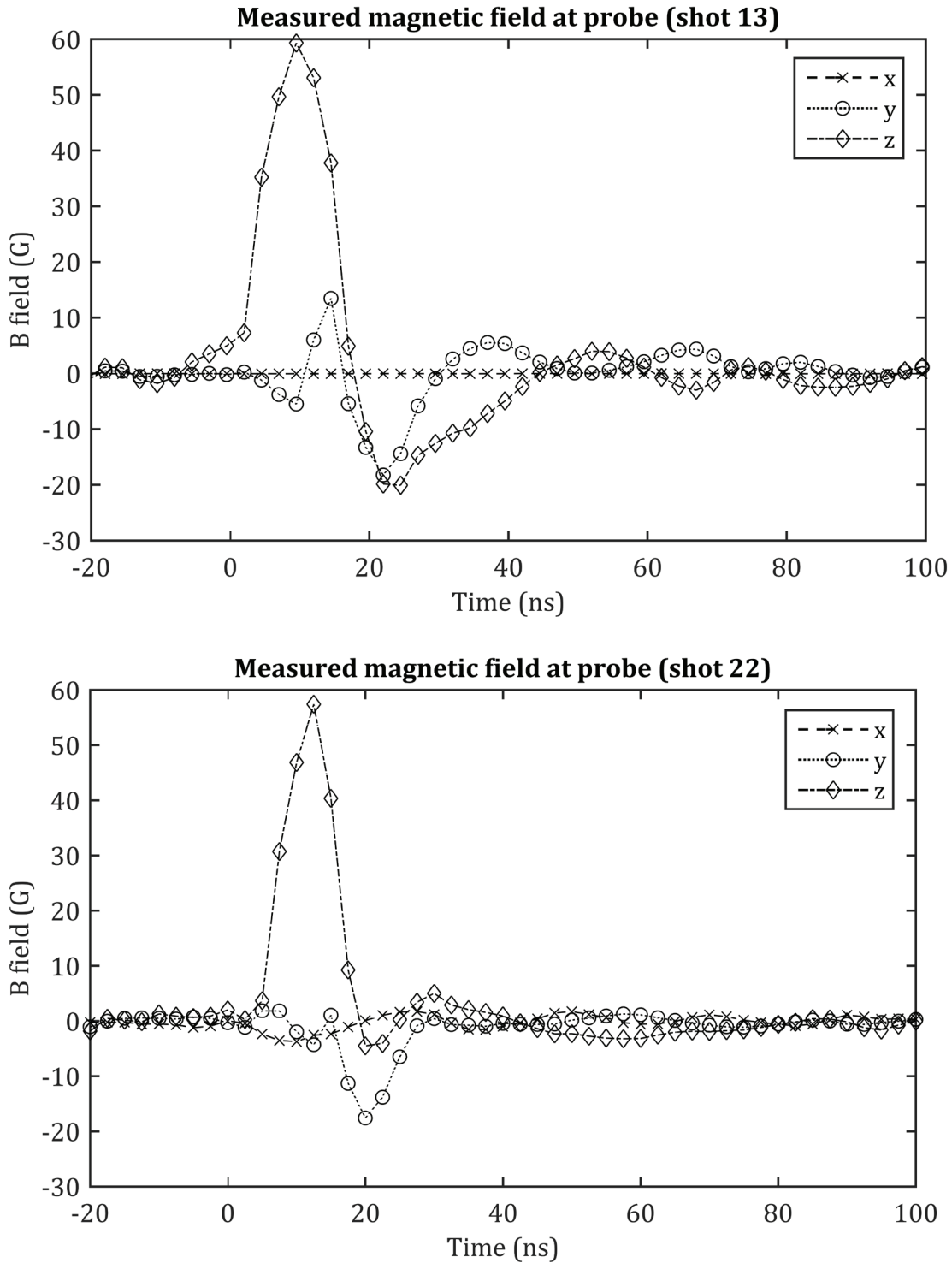

Figure 5.27. The magnetic field, computed from induction probe measurements, at a distance of 42 mm from the coil centre, resolved in three directions. These two shots were taken under the same experiment parameters.

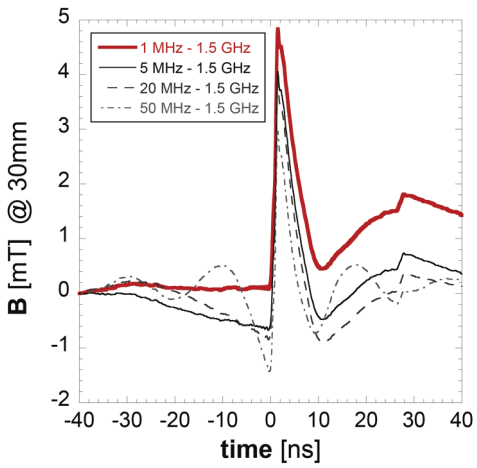

Figure 5.28. Magnetic field data of Figure 5.27 but collected from an alternative probe. From Santos *et al.* (2015). The different lines show the effect of different filters.

5.5. A SUMMARY OF THE EXPERIMENTS CHAPTER

At the GEKKO facility, I produced laser-driven shocks in a nitrogen atmosphere, using a bdot probe to monitor the generation of magnetic fields. In the first experiment, wavelet examination of the magnetic field data suggests that, only when a background field is imposed, a right-handed wave is excited. In the second GEKKO experiment, under slightly different conditions, no such feature was observed.

The third experiment, utilizing electron spectrometry, revealed the number of free electrons in the range of 50–200 keV increases when a background gas of 1 mbar density is present instead of a vacuum, but the limitations of the diagnostic precluded further interpretation.

The fourth experiment, on the production of magnetic fields of particularly high magnitude using a capacitor-type laser target, demonstrated the bdot probe could respond to high frequency events (up to 100 MHz).

6. Discussion

6.1. Shock waves at the Gekko facility

6.1.1. One dimensional hydro-radiative simulations.

I model the GEKKO experiment on a spherically symmetric grid by using the `Helios` software package to obtain estimates for the evolution of the system as a whole and for the plasma parameters outside the observation times. `Helios` is a one-dimensional radiation-magnetohydrodynamics code commonly used on experiments of this nature. From an initial condition and specification of materials the software package solves the equations of radiation-magnetohydrodynamics on a Lagrangian grid. (MacFarlane *et al.*, 2006.)

The simulation begins with laser incident on a carbon region in a low-density nitrogen atmosphere. `Helios` simulates the interaction of the laser light, the absorption of energy and the ionization dynamics including in the nitrogen gas, the resulting disassembly of the rod and the expansion of a shock into the surrounding atmosphere. Ions and electrons are treated as two fluids, and radiation exchange is modelled, but magnetohydrodynamic effects are not included in the simulations. To tune the parameters of the model I adjust the energy supplied to the system in the model until the initial expansion front of the shock simulated in Helios matches the experimental observations in the measured position. This happens at about 3% energy in line with previous work (Gregori *et al.*, 2012). This is consistent over the laser energy range used in the experiments. It is important to say that I do not use any information gleaned from the bdot probe measurements to tune the `Helios` simulations.

The Flash centre at the University of Chicago has also modelled the disassembly of the carbon rod under similar conditions (Tzeferacos *et al.*, 2012) in two dimensions. The

authors find that the shock produced is asymmetric because the laser driver breaks the symmetry. `Helios` cannot capture this behaviour because it is a purely one-dimensional code. By 100 ns, this represents a 0.08 cm difference in shock position of the front compared with rear side of the target. This discrepancy is not captured by the one-dimensional simulations I use.

The purpose of this modelling is to obtain estimates of plasma parameters as a function of radius that are difficult to measure: in particular the temperatures and densities of the electron and ion components and the mean charge state of the ions. From these quantities parameters such as the electron and ion plasma frequencies may be calculated (Huba, 2009).

In Figure 6.1, I include a plot of the shock position as estimated by `Helios`, together with a Sedov–Taylor fit to those position estimates. The fit is made on points 100 ns to 200 ns; it diverges after this, suggesting that the simpler Sedov–Taylor model is not including important physics, such as the relevance of losses.

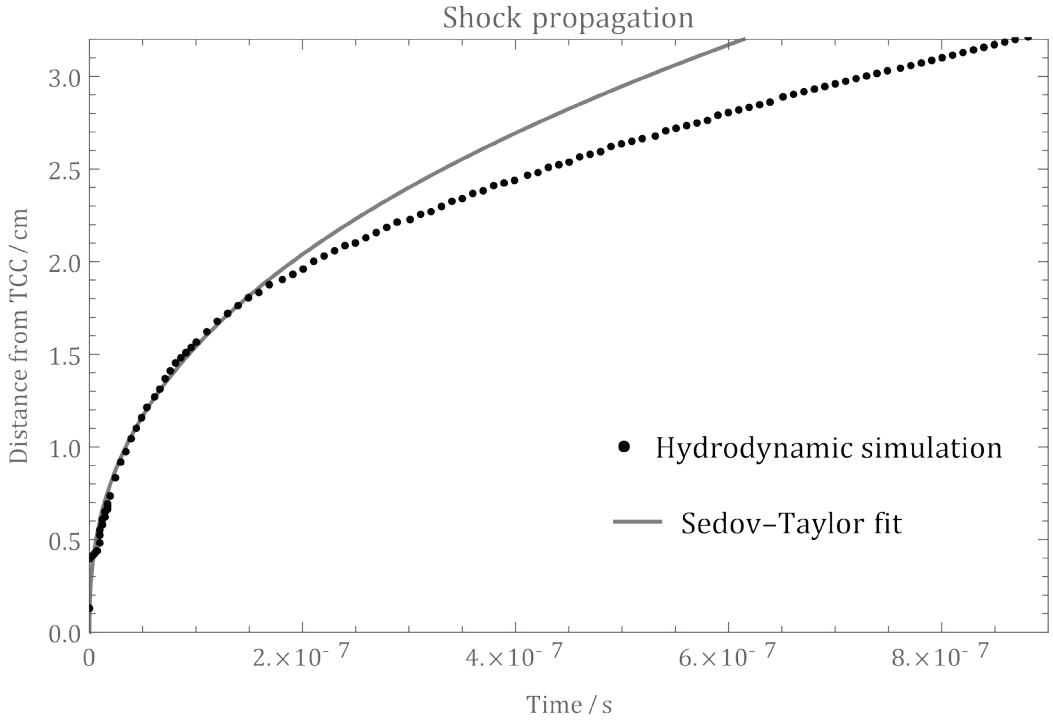

Figure 6.1. The hydrodynamic simulation against a best-fit Sedov–Taylor curve on data between 100 ns and 200 ns, at 1.3 kJ.

6.1.2. On the validity of the hydrodynamic simulations.

`Helios` is a one-dimensional package and it therefore cannot include many effects such as flow turbulence and shock asphericity that arise in multi-dimensional systems. Asphericity in the shock can lead to the spontaneous generation of magnetic fields through the Biermann battery effect (Gregori *et al.*, 2012); and such fields lie off the z-axis (rather they occur in the local tangent plane of the shock), which would disturb the validity of modelling of the situation as consisting of only parallel field lines. (The fields would lie off the z-axis because they occur with $d\boldsymbol{B}/dt \propto \boldsymbol{\nabla} T_e \wedge \boldsymbol{\nabla} n_e$, and, on the z-axis, the density gradient lies along z.) Moreover, turbulence in the flow both amplifies and further distorts the spatial geometry of the field lines (Meinecke *et al.*, 2014). Therefore, at least behind the shock, the magnetic field lines are not straight and parallel as assumed in the later analysis. To date I have not addressed these concerns in the work.

While the `Helios` code treats the electron and ion fluids separately, it assumes they are co-moving and each at a Maxwell temperature. This fluid assumption is a little at odds with the later modelling I do of the shock front with the inclusion of the downstream electron flow; which is allowed to move separately, still as a fluid, from the bulk electron fluid.

The final concern is that ionization dynamics are only approximated. As I discussed in section 2.1.5, we can expect a degree of ionization of the atmosphere at early time because of prompt electrons released during the laser-matter interaction. However, although `Helios` does include inverse-bremsstrahlung effects, the effect is only used for local heating and the 'long range' transport of hot electrons—as particles rather than as a fluidic component—is not included in the fluid model. Helios instead allows all layers of gas to absorb the laser light directly and in that manner become partially ionized.

However, one-dimensional simulations have the advantage of being fast to run and being relatively easy to interpret. They may be readily compared with analytical models, such as the Sedov–Taylor shock wave.

6.2. UPSTREAM-PROPAGATING WHISTLER WAVES

6.2.1. Analysis from theory.

I apply the analysis presented in section 2.3.4 on page 34, using the parameters estimated by simulation (as constrained by interferometry and other measurements) in part 6.1. First the shock position as a function of time is detected by the peak in ion density jump. This position is slightly ahead of the temperature peak. Then the data either side of the shock are passed to a mathematical function representing the local dispersion relation, adapted from Gary (1985) as expressed in (2.5).

$$\omega^2 - k^2c^2 + k^2c^2 \sum_j S_j^{\pm}(\mathbf{k}, \omega) = 0. \tag{6.1}$$

The $S_j^{\pm}$ are the dimensionless conductivities of the individual components. Let the subscript 'e' refer to the upstream, unshocked electron component. Then

$$S_e^{\pm}(\mathbf{k}, \omega) = \frac{\omega_{pe}^2}{k^2c^2}\left(\zeta_e Z(\zeta_e^{\pm})\right); \tag{6.2}$$

Z has the meaning given in (2.36) and

$$\zeta_e = \frac{\omega}{\sqrt{2}kv_{Th,e}}$$

$$\zeta_e^{\pm} = \frac{\omega \pm \omega_{ce}}{\sqrt{2}kv_{Th,e}}$$

The quantities ω_{pe}, ω_{ce} and $v_{Th,e}$ are evaluated in the relevant position upstream of the shock directly from the `Helios` data, for instance three electron mean free paths ahead of the front (but this position can be varied). The ion component is evaluated in the same position.

The electron beam component (subscript 'b') arising from downstream is similar but the quantities

$$\zeta_b = \frac{1}{\sqrt{2}kv_{Th,b}}(\omega - \mathbf{k}\cdot\mathbf{v}_{0b}) \text{ and,}$$

$$\zeta_b^{\pm} = \frac{1}{\sqrt{2}kv_{Th,b}}(\omega - \mathbf{k}\cdot\mathbf{v}_{0b} \pm \omega_{ce}),$$

are evaluated in the downstream, shocked region; except $\mathbf{v}_{0b}$, which is the difference

between the fluid velocity in the shock region and the fluid velocity in the unshocked layer under consideration in (6.2).

The choice of depth in front of the shock is important because the deeper into the unshocked medium, the more that collisions will deplete the density of the warm electron beam component arising from downstream. The warm beam's density is computed based on the distance from the sampling position and the local electron mean free path. However, the shock front is not modelled as a zero-width region in `Helios`, but as an extended transition region with a ramp of finite gradient. Too close or inside the front and there is no longer a cold 'unshocked' background inside which the 'beam' may propagate.

(6.1) is numerically solved (as earlier discussed in section 2.3.4) to give a prediction of the growth or damping rates of each frequency component in the given layer of plasma at the particular time. Together with some assumption of the spectral distribution of the local noise, this gives an estimation of the emission profile at a particular time at a particular place; for instance, see Figure 6.2. In the figure, the solid line shows the computed dispersion function, that is, the wave frequency for a given wave number. The imaginary component is shown with either a dotted line for positive growth rate, or a dashed line where it is damped. A solid vertical line shows the wave number where the wave is most unstable to growth; in this particular configuration it occurs at 39.5 cm^{-1}. This corresponds to a frequency of 64.5 MHz. The horizontal line shows the observed right-handed waves, as found in our wavelet analysis (Figure 5.10 on page 116), which were centred on 60 MHz. The correspondence between the prediction and the observation is readily seen.

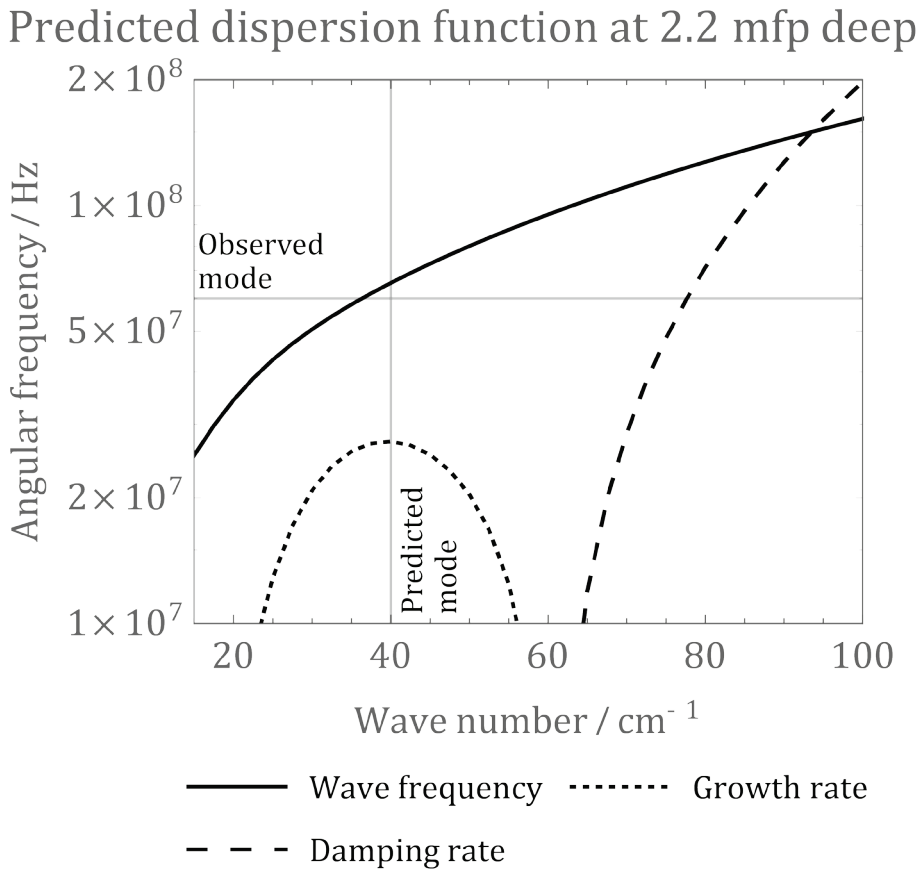

Figure 6.2. Predicted dispersion function 2.2 electron m.f.p.s ahead of the shock, at 75 ns in the 1.3 kJ experiment. The observed mode at 60 MHz is also noted.

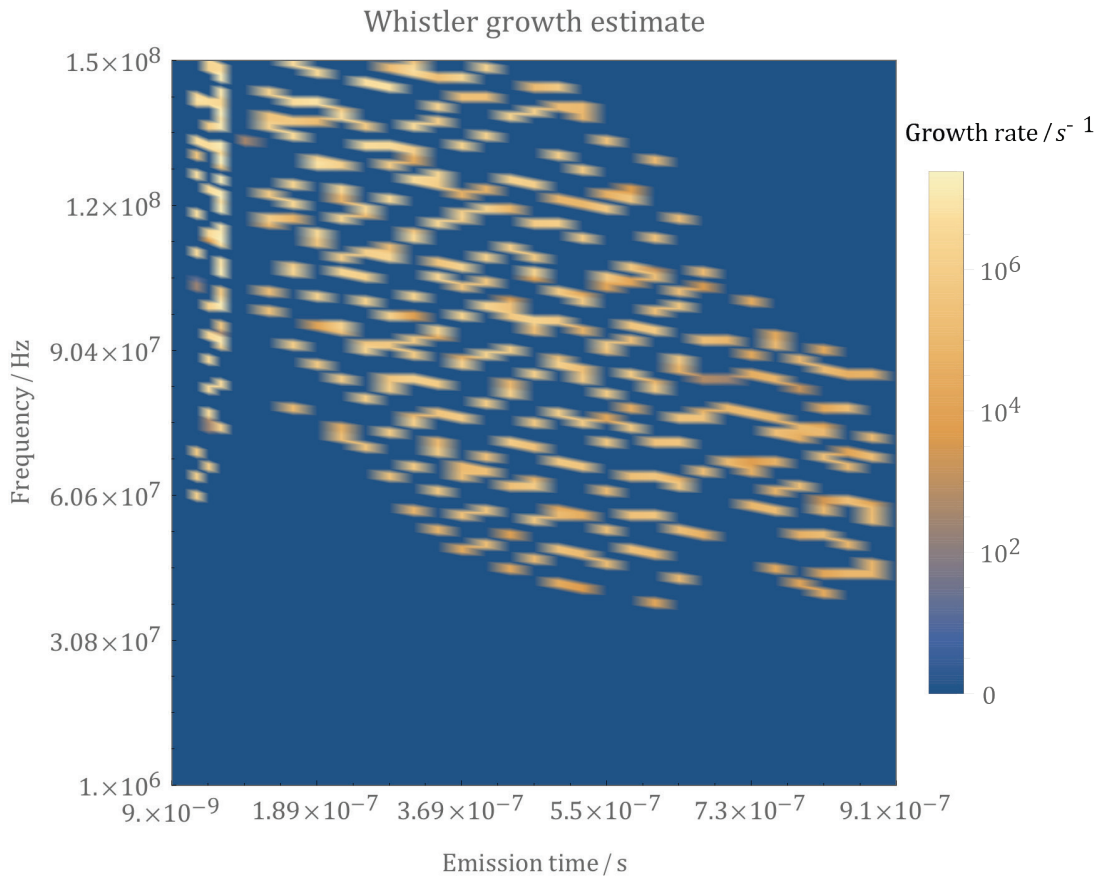

Figure 6.3. The computed growth chart for the GEKKO 2012 experiment, showing the expected growth rates of any whistler disturbance ahead of the shock, in the 1.3 kJ case.

Further a section of layers in front of the shock can be integrated to give a comprehensive emission prediction near the shock, with the passage of time. This is actually a prediction of the growth rate of background fluctuations into waves. The emission estimation is given in Figure 6.5. This shows how the shock is predicted to excite whistler modes in the layers upstream of the shock, as time evolves. At early time there is a bright, wideband flash; and subsequently after about 10^{-7} seconds there is a gently narrowing band of emission, moving downward in frequency space and settling between around 60–90 MHz. The growth rate peaks at about 10^{7} s^{-1}, which is perhaps not very large for the experimental time frame.

6.2.2. Emission to observation mapping

The emission estimation however is not the same as what we would expect to observe with a probe, because the various components emitted must travel through the plasma, and each has a different phase speed. Therefore I pass the emission graph through a function that calculates the appropriate phase delay from the emission given the time, position, and phase speed of each point on the emission graph to give a plot of the arrival time by component. The phase speed is $v_{ph} = \omega/k$, and the distance over which the component is to travel is approximated as the probe distance from TCC less the shock position. The shock position is estimated by `Helios`. Such a graph looks as in Figure 6.4, and it is a key result. The graph suggests no emission from the shock front arrives until about 300 ns after the shock is produced; at which point a wide band appears at once. By 700 ns, the emitted fronts have narrowed to be between 40 and 80 MHz in bandwidth. The agreement with Figure 5.10 on page 116 is striking.

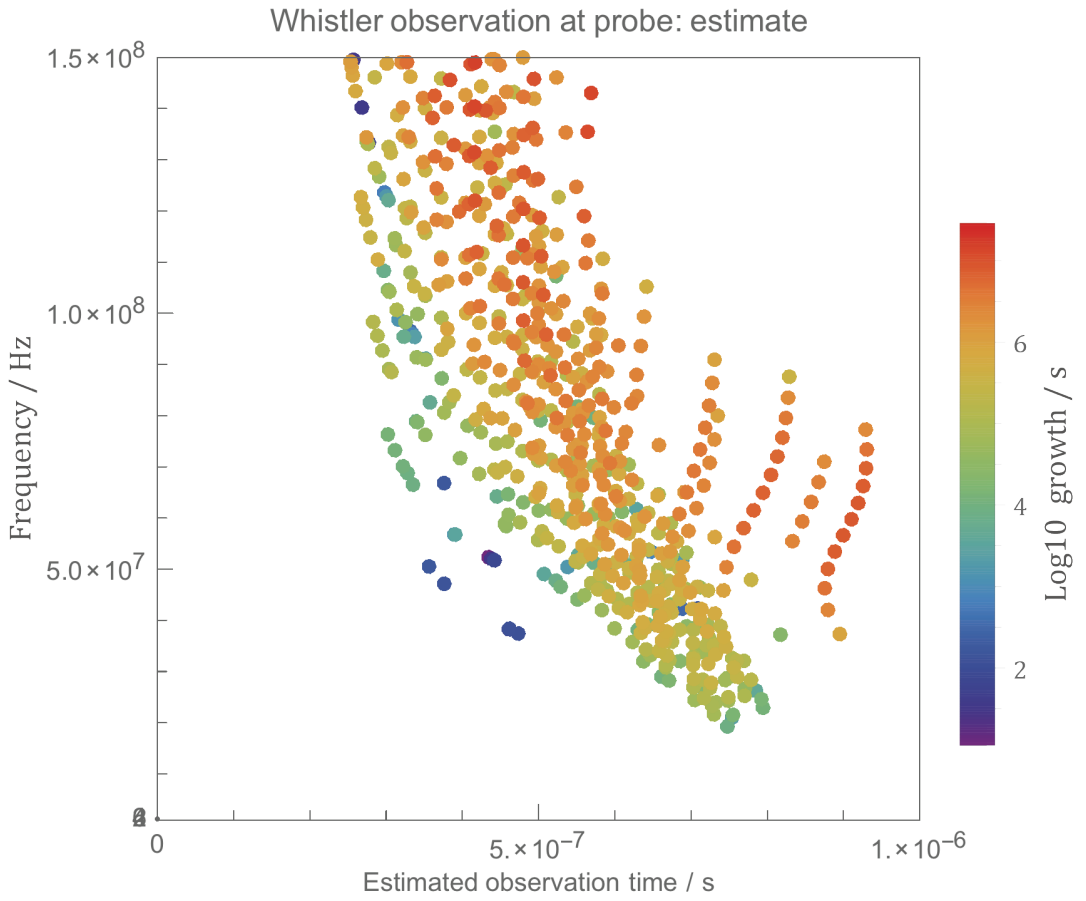

Figure 6.4. The predicted signal at the bdot probe, based on the above calculations, in the GEKKO 12 experiment. This is a key result.

6.2.3. Concord of the observation and prediction.

Comparing Figure 6.4 (the prediction of wavelet excitation from theory and measured experimental parameters) and Figure 5.10 on page 116 (the observations made with the bdot probe), the agreement between the observation and the prediction is good, in terms of the expected frequency range emitted (around 60 MHz). The prediction data have not been tuned by the bdot observations.

The observed signal power in the experiment is somewhat higher than predicted, because a growth rate of 10^7 s^{-1} is only a few e-folds for a front that escapes the shock layer quickly enough to reach the probe.

The bursting behaviour observed in Figure 5.10 is seen in the prediction as well, at around 800 ns, but that is probably because of the low temporal density of the prediction dataset rather than an explanation of the measured result.

The close concord of the observation and prediction here suggest that the proposed excitation mechanism is valid; and that upstream waves are indeed emitted from the shock front in the laboratory system. It opens this up as a platform to study the behaviour of these waves.

6.2.4. Application to the bow shock; and validity of the scaling relations.

Some dimensionless numbers are given in Table 4, together with their estimated values in the laboratory and in the experiment. I should underscore that the importance is the reciprocal of the number, so for instance while clearly $15 \neq 10^{14}$, it might not be an unreasonable approximation to say that $0.07 \approx 0$ in the context of laboratory astrophysics, particularly given the error bars on some quantities such as temperature. However, the difference in the Biermann number [as defined by Cross *et al.* (2014), a measure of the importance of the Biermann battery effect] suggests the result is not a true scaling of the system.

The disturbance in the magnetic field lines by the creation of off-parallel magnetic field lines changes the character of the shock from being 'parallel' to being 'quasi-parallel'.

This is actually more in keeping with the electron foreshock in the bow shock, which exists in a region where ions are unable to propagate far upstream because of the field geometry bending away from parallel. However, in the laboratory system ions are principally constrained by collisions. I have not evaluated the effect of off-parallel magnetic field components in the whistler excitation model, but this could be a refinement made in future work.

Table 4. Some dimensionless numbers expressing the relevancy of the experiment to the bow shock.

Quantity	**Definition**	**Meaning**	**Upstream bow shock**	**Lab. expt.**
Reynolds number	$\mathrm{Re} = \frac{x_0 v_0}{\nu}$	Inertial forces *vs.* viscous forces	10^6	10^4
Magnetic Reynolds number	$\mathrm{Re_m} = \frac{x_0 v_0}{\eta}$	Advection *vs.* magnetic diffusion	10^{14}	15
Péclet number (heat)	$\mathrm{Pe} = \frac{x_0 v_0}{\kappa}$	Heat convection *vs.* heat conduction	10^9	70
Biermann number	$\mathrm{Bi} = \frac{\mathrm{e}(1+\mathrm{Z})\sqrt{\rho_0} x_0}{m}$	Magnetic field advection *vs.* field generation	10^4	10^{-1}

Definitions from Huba (2009) and Cross *et al.* (2014). Estimated values of bow shock from Balogh and Treumann (2013); lab. values cross-checked with Gregori *et al.* (2012).

6.3. THE NON-DETECTION OF UPSTREAM WAVES IN THE SECOND GEKKO EXPERIMENT

In the 2014 experiment at the GEKKO facility I did not observe any waves of the type probably detected in the 2012 experiment. Examining the plasma variables with the dispersion function (6.1) suggests that the high magnetic field was to blame: the experiment was designed before the effect was understood. The changed field strength pushes the system out of the parameter space region where a whistler wave would be expected to be excited: see Figure 6.5. There is a region of weak damping up to a wave number of 10 cm^{-1}, but aside from that the prediction is that the plasma in this layer is approximately transparent to whistler waves with neither growth nor damping.

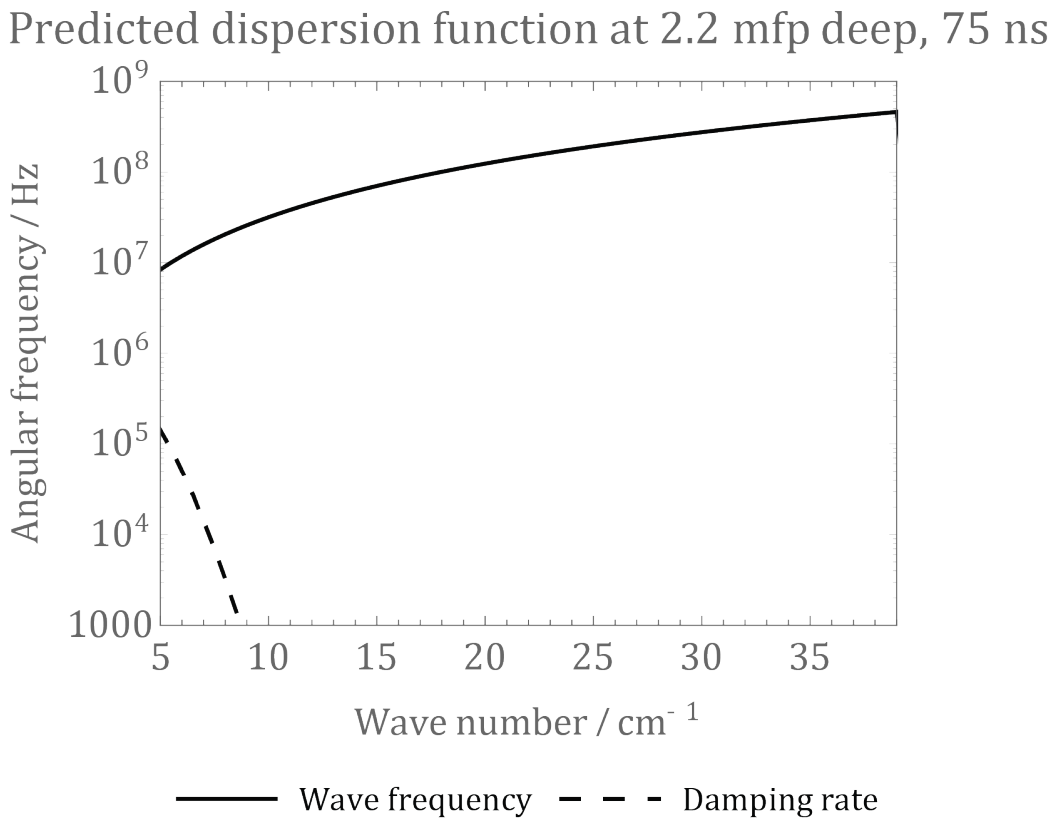

Figure 6.5. Predicted dispersion function for the 2014 experiment, 2.2 electron m.f.p.s ahead of the shock, at 75 ns, 450 J driver energy.

Figure 6.5 shows the dispersion curve of the plasma at one particular time instant in one particular slice ahead of the shock, but actually it is indicative of the curve over the entire experiment. In Figure 6.6, the predicted growth of right-handed whistler modes, in the plasma up to ten m.f.p.s upstream of the shock is shown. The chart shows the instability to growth in colour, as a function of time since the laser flash horizontally and as a function of frequency vertically. The graph does not show any growth terms higher than about 10^{-6} s^{-1}; no emission is predicted.

However, the dispersion relation here does not act to damp whistler waves either. If the waves detected in the 2012 experiment were created somewhere outside the shock, such as at the laser-matter interaction point, they would be free in the 2014 experiment to propagate through the shocked region and would be detected by the probe. Although not conclusive, the null result in this case does not undermine the hypothesis that the shock is the origin of the detected waves.

6.4. SUMMARY OF THE DISCUSSION

I have presented a mechanism by which the data shown in Parts 5.1 and 5.2 can be consistently explained: shock-heated electrons diffuse a little way upstream, putting the plasma there into a situation unstable to whistler emission. The frequencies predicted by the dispersion relation for a magnetized plasma, as discussed in section 2.3.4, are those detected by the bdot probe. This suggests a right-handed whistler wave is being launched by the shock front, propagating upstream against the flow, to arrive at the probe. To the author's knowledge, if this hypothesis is borne out, it would be the first time such an observation has been made in a laboratory.

There are some limitations to the approach discussed here. For one, the data provided by the `Helios` software package, which underlie the dispersion curve analyses, are likely to be inaccurate so far as the ionization dynamics are concerned. For another, the shock's asphericity and the full magnetic field structure should be properly incorporated into the wave-launch model. Further work, including a wider and more dedicated portfolio of experiment diagnostics, modelling with a two-dimensional code, and a design intended to approach the correct dimensionless numbers, could address this.

With such improvements, it would be possible to design experiments to access particular configurations in the electron foreshock, or to validate codes making upstream wave predictions.

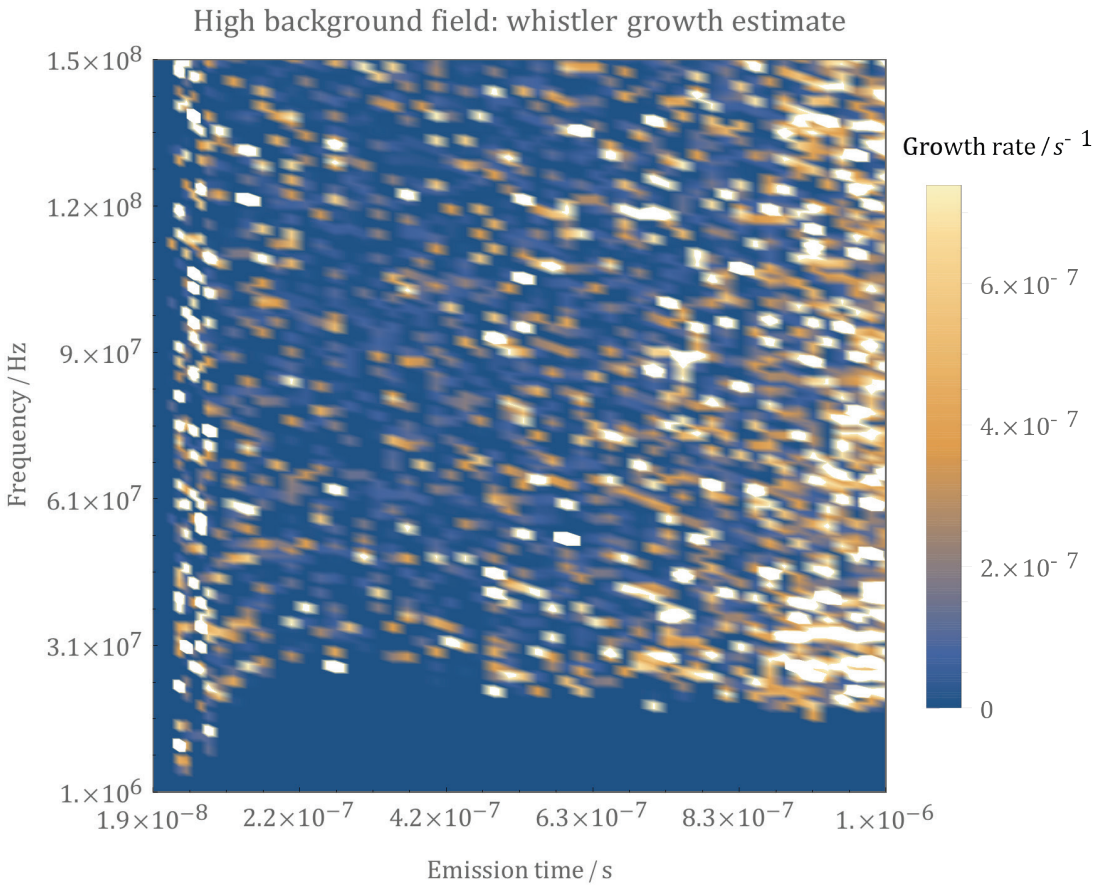

Figure 6.6. The computed growth chart, showing the expected growth rates of any whistler disturbance ahead of the shock. The chart essentially predicts zero growth (the growth rate is below 10^{-6} s^{-1}).

7. Conclusions

In this thesis I have presented and examined the hypothesis that the waves detected during a laser-laboratory experiment are upstream waves, launched by a laser-produced shock front propagating into the nitrogen atmosphere. From optical observations of the laser experiment, I tune a one-dimensional hydrodynamic simulation that provides sufficient data to construct the whistler dispersion function in the region immediately ahead of the shock. I find that one particular frequency range is unstable to whistler emission. The range narrows as the shock evolves with time, culminating in a predicted right-hand circularly polarized emission band between 50 and 90 MHz at 1 μs.

Magnetic field observations made by the bdot probe in the experiment, analysed by a wavelet process, independently shows right-handed bursted magnetic waves of 60±10 MHz, detected at the probe between about 300 ns to about 1 μs. In order to compare the predicted emissions, which are computed in a layer moving just ahead of the shock, with the experimental magnetic field observations, which are made at a fixed position 3 cm from the laser-matter interaction point, I compute the expected distribution of whistler waves arriving at the 3 cm position, based on their flight time evaluated for each frequency component. This simulated observation prediction agrees well with the waves actually observed by the bdot probe, in terms of the frequency range and timing of such waves.

To the author's knowledge, this is the first time a laboratory platform has been successfully used to produce, detect and characterize upstream waves. In particular, by using similarity scaling, the waves appear to be analogous to the poorly understood 'lion roars' or whistler bursts, which occur in the Earth's bow shock probably as a result of field-aligned electron beams. Even though the very low Biermann number in my experiment, as well as the very high collisionality, mean it is difficult to compare the

experiment directly to processes occurring in the bow shock, the usefulness of a new platform to study bow shock foreshock waves should not be underestimated. In particular I am able to study the macroscopic, average properties of these waves, which cannot be done with instruments on satellites.

I discuss also a second experiment, where the plasma properties and magnetic field geometry differed from the first experiment. This experiment did not show any upstream behaviour, but application of earlier predictive methods only predicts damping and no growth terms here. Therefore the hypothesis is not undermined by the null result.

Laboratory astrophysics continues to expand into new domains. This thesis represents a new avenue for the laboratory astrophysics, looking not just at large scale behaviour but also at the "microstructure" or finer details such as upstream waves. With time on the National Ignition Facility assigned for the study of collisionless shocks, upstream waves generated by other mechanisms may soon be available for direct laboratory study.

Appendix. A proof of the Fourier uncertainty theorem.

The following is adapted from Merryfield (2005), but generalized to signals of non-zero mean.

The Fourier uncertainty theorem.

Let $f \in \mathbf{L^2}$ and suppose f is normalized (*i.e.*, $\|f\| = 1$). For every Fourier transform pair f and $\tilde{f}$,

$$\sigma_t \sigma_\omega \geq \frac{1}{2}. \tag{A.1}$$

Proof.

Define a function $g(t) = e^{-im_\omega t} f(t)$, where the quantity m_ω has the meaning given in (4.15) for the function f. Then $|g(t)| = \left|e^{-im_\omega t}\right| |f(t)| = |f(t)|$. Since $\|f\| = 1$ we have by the definition of the norm (Definition 4 in Part 4.1) that

$$1 = \int_{-\infty}^{+\infty} |f(t)|^2 \, dt = \int_{-\infty}^{+\infty} |g(t)|^2 \, dt. \tag{A.2}$$

Exploiting that for any g, $|g(t)|^2 = g(t)g^*(t)$ (the asterisk denoting the complex conjugate),

$$1 = \int_{-\infty}^{+\infty} 1 \times g(t)g^*(t) \, dt, \tag{A.3}$$

The expression may be integrated by parts, with the subtlety that we take $\int 1 \, dt = (t - m_t)$; since this integral is conducted over the entire real line, the offset by a fixed constant makes no difference, and we obtain

$$1 = [(t - m_t)g(t)g^*(t)]\Big|_{-\infty}^{+\infty} - \int_{-\infty}^{+\infty} (t - m_t)\{g(t)g'^*(t) + g'(t)g^*(t)\}\,dt \tag{A.4}$$

The first term on the right hand side vanishes: since $\|g\| = 1$, to satisfy this $|g(t)|^2$ must go to zero quickly for sufficiently large $|t|$. The second term is more involved. Consider two general complex functions x and y; the identity

$$\Re(xy^* + x^*y) = 2\Re(xy^*) = 2\Re(x^*y) \tag{A.5}$$

may be readily verified. Turning back to (A.4), observe that the left hand side is entirely real-valued so the result of the integral on the right must be real also; applying the identity (A.5) under the integral sign to (A.4) gives

$$1 = -2\Re \int_{-\infty}^{+\infty} (t - m_t)\{g(t)g'^*(t)\}\,dt. \tag{A.6}$$

For any $z \in \mathbb{C}$, $\Re(z) \leq |z|$, therefore,

$$1 \leq 2\left|\int_{-\infty}^{+\infty} (t - m_t)\{g(t)g'^*(t)\}\,dt\right|; \tag{A.7}$$

and we may apply the Cauchy–Schwarz inequality (4.5) to split the multiplication under the integral into a product of two integrals;

$$1 \leq 2\left(\int_{-\infty}^{+\infty} |(t - m_t)g(t)|^2\,dt\right)^{\frac{1}{2}}\left(\int_{-\infty}^{+\infty} |g'^*(t)|^2\,dt\right)^{\frac{1}{2}}. \tag{A.8}$$

Reviewing the first integral on the right,

$$\begin{aligned}\int_{-\infty}^{+\infty} |(t - m_t)g(t)|^2\,dt &= \int_{-\infty}^{+\infty} (t - m_t)^2|g(t)|^2\,dt \\ &= \int_{-\infty}^{+\infty} (t - m_t)^2|f(t)|^2\,dt \\ &= \sigma_t^2.\end{aligned} \tag{A.9}$$

For the second integral, we require Parseval's theorem (4.6). This 'preservation of size' under the Fourier transform is fundamentally why inequality (A.1) exists. Applying the theorem, we find

$$\begin{aligned}\int_{-\infty}^{+\infty} |g'^*(t)|^2\,dt &= \int_{-\infty}^{+\infty} |i\omega\tilde{g}(\omega)|^2\,d\omega \\ &= \int_{-\infty}^{+\infty} \omega^2|\tilde{g}(\omega)|^2\,d\omega.\end{aligned} \tag{A.10}$$

Finally writing g back in terms of f,

$$\begin{aligned}\tilde{g}(\xi) &= \int_{-\infty}^{+\infty} g(x)e^{-i\xi x}\,dx \\ &= \int_{-\infty}^{+\infty} f(x)e^{-im_\omega x}e^{-i\xi x}\,dx \\ &= \int_{-\infty}^{+\infty} f(x)e^{-i(\xi+m_\omega)x}\,dx \\ &= \tilde{f}(m_\omega+\xi). \end{aligned} \tag{A.11}$$

Gathering these expressions and inserting them into (A.8),

$$1 \leq 2\sigma_t \left(\int_{-\infty}^{+\infty} \omega^2 \left|\tilde{f}(m_\omega+\omega)\right|^2 d\omega\right)^{\frac{1}{2}}. \tag{A.12}$$

Under a change of the integration variable ($\omega \to \omega - m_\omega$),

$$\begin{aligned} 1 &\leq 2\sigma_t \left(\int_{-\infty}^{+\infty} (\omega-m_\omega)^2 \left|\tilde{f}(\omega)\right|^2 d\omega\right)^{\frac{1}{2}} \\ &\leq 2\sigma_t\sigma_\omega\,, \end{aligned} \tag{A.13}$$

which suffices to prove result (A.1).

References

Baher, H. (1990). *Analog and digital signal processing*: Wiley.

Balogh, A., & Treumann, R. A. (2013). *Physics of collisionless shocks: space plasma shock waves* (Vol. 12): Springer Science & Business Media.

Benattar, R., Popovics, C., & Sigel, R. (1979). Polarized light interferometer for laser fusion studies. *Review of Scientific Instruments, 50*(12), 1583-1586.

Börner, M., Fils, J., Frank, A., Blažević, A., Hessling, T., Pelka, A., Schaumann, G., Schökel, A., Schumacher, D., Basko, M. M., Maruhn, J., Tauschwitz, A., & Roth, M. (2012). Development of a Nomarski-type multi-frame interferometer as a time and space resolving diagnostics for the free electron density of laser-generated plasma. *Review of Scientific Instruments, 83*(4), 043501.

Boyd, T. J. M., & Sanderson, J. J. (2003). *The physics of plasmas*. Cambridge, UK ; New York: Cambridge University Press.

Burgess, D. (1997). What do we really know about upstream waves? *Results of the Iastp Program, 20*(4-5), 673-682.

Burgess, D., & Scholer, M. (2013). Microphysics of Quasi-parallel Shocks in Collisionless Plasmas. *Space Science Reviews, 178*(2-4), 513-533.

Busold, S., Philipp, K., Otten, A., & Roth, M. (2014). Image plate characterization and absolute calibration to low kilo-electron-volt electrons. *Review of Scientific Instruments, 85*(11), 113306.

Chang, P. Y., Fiksel, G., Hohenberger, M., Knauer, J. P., Betti, R., Marshall, F. J., Meyerhofer, D. D., Séguin, F. H., & Petrasso, R. D. (2011). Fusion yield enhancement in magnetized laser-driven implosions. *Physical Review Letters, 107*(3), 035006.

Chen, H., Back, N. L., Bartal, T., Beg, F. N., Eder, D. C., Link, A. J., MacPhee, A. G., Ping, Y., Song , P. M., Throop, A., & Van Woerkom, L. (2008). Absolute

calibration of image plates for electrons at energy between 100 keV and 4 MeV. *Review of Scientific Instruments, 79*(3), 033301.

Collier, M. R., Siebeck, D. G., Cravens, T. E., Robertson, I. P., & Omidi, N. (2010). Astrophysics Noise: A Space Weather Signal. *Eos, Transactions, American Geophysical Union, 91*(24), 213-214.

Connor, J. W., & Taylor, J. B. (1977). Scaling laws for plasma confinement. *Nuclear Fusion, 17*(5), 1047.

Courtois, C., Grundy, R. A. D., Ash, A. D., Chambers, D. M., Woolsey, N. C., Dendy, R. O., & McClements, K. G. (2004). Experiment on collisionless plasma interaction with applications to supernova remnant physics. *Physics of Plasmas, 11*(7), 3386-3393.

Cross, J. E., Reville, B., & Gregori, G. (2014). Scaling of magneto-quantum-radiative hydrodynamic equations: from laser-produced plasmas to astrophysics. *Astrophysical Journal, 795*(1), 59.

Daido, H., Miki, F., Mima, K., Fujita, M., Sawai, K., Fujita, H., Kitagawa, Y., Nakai, S., & Yamanaka, C. (1986). Generation of a strong magnetic field by an intense CO_2 laser pulse. *Physical Review Letters, 56*(8), 846-849.

Daniels, J., Russell, C., Strangeway, R., Wei, H., & Zhang, T. (2012). Whistler mode bursts in the Venus ionosphere due to lightning: statistical properties using Venus Express magnetometer observations. *Journal of Geophysical Research: Planets, 117*(E4).

Dubinin, E. M., Maksimovic, M., Cornilleau-Wehrlin, N., Fontaine, D., Travnicek, P., Mangeney, A., Alexandrova, O., Sauer, K., Fraenz, M., Dandouras, I., Lucek, E., Fazakerley, A., Balogh, A., & Andre, M. (2007). Coherent whistler emissions in the magnetosphere – Cluster observations. *Annales Geophysicae, 25*(1), 303-315.

Escoubet, C. P., Schmidt, R., & Russell, C. (2012). *The Cluster and Phoenix Missions*: Springer Netherlands.

Everson, E. T., Pribyl, P., Constantin, C. G., Zylstra, A., Schaeffer, D., Kugland, N. L., & Niemann, C. (2009). Design, construction, and calibration of a three-axis, high-frequency magnetic probe (B-dot probe) as a diagnostic for exploding plasmas. *Review of Scientific Instruments, 80*(11).

Fiksel, G., Marshall, F. J., Mileham, C., & Stoeckl, C. (2012). Note: spatial resolution of Fuji BAS-TR and BAS-SR imaging plates. *Review of Scientific Instruments, 83*(8), 086103.

Fitzpatrick, R. (2011). *The Physics of Plasmas*: Lulu.com.

Fourier, J. B. J. (1822). *Théorie analytique de la chaleur*. Paris.

Fujioka, S., Zhang, Z., Ishihara, K., Shigemori, K., Hironaka, Y., Johzaki, T., Sunahara, A., Yamamoto, N., Nakashima, H., Watanabe, T., Shiraga, H., Nishimura, H., & Azechi, H. (2013). Kilotesla magnetic field due to a capacitor-coil target driven by high power laser. *Scientific Reports, 3*.

Gary, S. P. (1985). Electromagnetic electron-beam instabilities—hot, isotropic beams. *Journal of Geophysical Research: Space Physics, 90*(11), 815-822.

Gregori, G., Ravasio, A., Murphy, C. D., Schaar, K., Baird, A., Bell, A. R., Benuzzi-Mounaix, A., Bingham, R., Constantin, C., Drake, R. P., Edwards, M., Everson, E. T., Gregory, C. D., Kuramitsu, Y., Lau, W., Mithen, J., Niemann, C., Park, H. S., Remington, B. A., Reville, B., Robinson, A. P., Ryutov, D. D., Sakawa, Y., Yang, S., Woolsey, N. C., Koenig, M., & Miniati, F. (2012). Generation of scaled protogalactic seed magnetic fields in laser-produced shock waves. *Nature, 481*(7382), 480-483.

Gregory, C. D. (2007). *Astrophysical jet experiments with laser-produced plasmas.* (PhD), University of York, York.

Grinsted, A., Moore, J. C., & Jevrejeva, S. (2004). Application of the cross wavelet transform and wavelet coherence to geophysical time series. *Nonlinear Processes in Geophysics, 11*(5-6), 561-566.

Harilal, S. S., O'Shay, B., Tao, Y., & Tillack, M. S. (2006). Ambient gas effects on the dynamics of laser-produced tin plume expansion. *Journal of Applied Physics, 99*(8), 083303.

Herivel, J. (1975). *Joseph Fourier: the man and the physicist*. Oxford: Clarendon Press.

Herlach, F. (2002). Laboratory electromagnets—from Oersted to megagauss. *Physica B: Condensed Matter, 319*(1–4), 321-329.

Hobara, Y., Walker, S. N., Balikhin, M., Pokhotelov, O. A., Dunlop, M., Nilsson, H., & Rème, H. (2007). Characteristics of terrestrial foreshock ULF waves: Cluster observations. *Journal of Geophysical Research: Space Physics, 112*(A7).

Huba, J. (2009). *NRL Plasma Formulary 2009*.

Huddlestone, R. H., & Leonard, S. L. (1965). *Plasma diagnostic techniques*. New York: Academic Press.

Hunte, F., Jaroszynski, J., Gurevich, A., Larbalestier, D. C., Jin, R., Sefat, A. S., McGuire, M. A., Sales, B. C., Christen, D. K., & Mandrus, D. (2008). Two-band superconductivity in LaFeAsO0.89F0.11 at very high magnetic fields. *Nature, 453*(7197), 903-905.

Hutchinson, I. H. (2002). *Principles of plasma diagnostics* (2nd ed.). Cambridge: Cambridge University Press.

Issac, R. C., Varier, G. K., Gopinath, P., Harilal, S. S., Nampoori, V. P. N., & Vallabhan, C. P. G. (1998). Prompt electron emission and collisional ionization of ambient gas during pulsed laser ablation of silver. *Applied Physics A, 67*(5), 557-561.

Kangas, J., Kultima, J., Guglielmi, A., Potapov, A., & Hayashi, K. (2001). Impact of interplanetary shock on the ULF wave activity: a case study of the storm sudden commencement on September 22, 1999. *Earth, planets and space, 53*(12), 1177-1182.

Landau, L. D., & Lifshitz, E. M. (1987). *Fluid mechanics* (2nd ed.). Oxford, England; New York: Pergamon Press.

Li, L., Qu, L. S., & Liao, X. H. (2007). Haar wavelet for machine fault diagnosis. *Mechanical Systems and Signal Processing, 21*(4), 1773-1786.

Liddell, H. G., & Scott, R. (1890). *A Greek-English Lexicon*. Oxford: Clarendon Press.

MacFarlane, J. J., Golovkin, I. E., & Woodruff, P. R. (2006). HELIOS-CR—a 1-D radiation-magnetohydrodynamics code with inline atomic kinetics modeling. *Journal of Quantitative Spectroscopy & Radiative Transfer, 99*(1-3), 381-397.

Mallat, S. G. (1998). *A wavelet tour of signal processing*. San Diego: Academic Press.

Maraun, D., & Kurths, J. (2004). Cross wavelet analysis: significance testing and pitfalls. *Nonlinear Processes in Geophysics, 11*(4), 505-514.

Meinecke, J., Doyle, H. W., Miniati, F., Bell, A. R., Bingham, R., Crowston, R., Drake, R. P., Fatenejad, M., Koenig, M., Kuramitsu, Y., C. Kuranz, C., Lamb, D. Q., Lee, D., MacDonald, M. J., Murphy, C. D., Park, H. S., Pelka, A., Ravasio, A., Sakawa, Y., Schekochihin, A. A., Scopatz, A., Tzeferacos, P., Wan, W. C.,

Woolsey, N. C., Yurchak, R., Reville, B., & Gregori, G. (2014). Turbulent amplification of magnetic fields in laboratory laser-produced shock waves. *Nature Physics, 10*(7), 520-524.

Merryfield, K. (2005). Course notes for Fourier Analysis. http://web.csulb.edu/~kmerry/FourierAnalysis/

Meyers, S. D., Kelly, B. G., & O'Brien, J. J. (1993). An introduction to wavelet analysis in oceanography and meteorology: with application to the dispersion of Yanai waves. *Monthly Weather Review, 121*(10), 2858-2866.

Neuber, A., & Dickens, J. C. (2004). Magnetic flux compression generators. *Proceedings of the IEEE, 92*(7), 1205-1215.

Ovsyannikov, A. A. Z., M. F. (2000). *Plasma Diagnostics* (A. A. Z. Ovsyannikov, M. F. Ed.). Cambridge: Cambridge International Science Publishing.

Phillips, R. C., & Turner, E. B. (1965). Construction and calibration techniques of high frequency magnetic probes. *Review of Scientific Instruments, 36*(12), 1822-1825.

Portugall, O., Solane, P. Y., Plochocka, P., Maude, D. K., & Nicholas, R. J. (2013). Beyond 100 tesla: scientific experiments using single-turn coils. *Comptes Rendus Physique, 14*(1), 115-120.

Posner, A., Schwadron, N. A., McComas, D. J., Roelof, E. C., & Galvin, A. B. (2004). Suprathermal ions ahead of interplanetary shocks: new observations and critical instrumentation required for future space weather monitoring. *Space Weather, 2*(10).

Remington, B. A., Drake, R. P., Takabe, H., & Arnett, D. (2000). A review of astrophysics experiments on intense lasers. *Physics of Plasmas, 7*(5), 1641-1652.

Reville, B., Bell, A. R., & Gregori, G. (2013). Diffusive shock acceleration at laser-driven shocks: studying cosmic-ray accelerators in the laboratory. *New Journal of Physics, 15*.

Ryutov, D. D., Drake, R. P., & Remington, B. A. (2000). Criteria for scaled laboratory simulations of astrophysical MHD phenomena. *Astrophysical Journal Supplement Series, 127*(2), 465-468.

Santos, J. J., Bailly-Grandvaux, M., Giuffrida, L., Forestier-Colleoni, P., Fujioka, S., Zhang, Z., Korneev, P., Bouillaud, R., Dorard, S., Batani, D., Chevrot, M., Cross, J. E., Crowston, R., Dubois, J. L., Gazave, J., Gregori, G., d'Humières,

E., Hulin, S., Ishihara, K., Kojima, S., Loyez, E., Marquès, J. R., Morace, A., Nicolaï, P., Peyrusse, O., Poyé, A., Raffestin, D., Ribolzi, J., Roth, M., Schaumann, G., Serres, F., Tikhonchuk, V. T., Vacar, P., & Woolsey, N. (2015). Laser-driven platform for generation and characterization of strong quasi-static magnetic fields. *New Journal of Physics, 17*(8), 083051.

Schielke, S., Speidel, K. H., Kenn, O., Leske, J., Gemein, N., Offer, M., Sharon, Y. Y., Zamick, L., Gerber, J., & Maier-Komor, P. (2003). First measurement and shell model interpretation of the g factor of the 21+ state in self-conjugate radioactive 44-Ti. *Physics Letters B, 567*(3–4), 153-158.

Schwartz, S. J., Henley, E., Mitchell, J., & Krasnoselskikh, V. (2011). Electron temperature gradient scale at collisionless shocks. *Physical Review Letters, 107*(21), 215002.

Sedov, L. I. (1946). Propagation of strong shock waves. *Journal of Applied Mathematics and Mechanics, 10*, 241-250.

Selzer, L. A., Hnat, B., Osman, K. T., Nakariakov, V. M., Eastwood, J. P., & Burgess, D. (2014). Temperature anisotropy in the presence of ultra low frequency waves in the terrestrial foreshock. *Astrophysical Journal Letters, 788*(1), L5.

Smith, C. W., L'Heureux, J., Ness, N. F., Acuña, M. H., Burlaga, L. F., & Scheifele, J. (1998). The Ace Magnetic Fields Experiment. In C. T. Russell, R. A. Mewaldt, & T. T. Von Rosenvinge (Eds.), *The Advanced Composition Explorer Mission* (pp. 613-632): Springer Netherlands.

Spitkovsky, A. (2008). Particle acceleration in relativistic collisionless shocks: Fermi process at last? *The Astrophysical Journal Letters, 682*(1), L5.

Stone, E. C., Cummings, A. C., McDonald, F. B., Heikkila, B. C., Lal, N., & Webber, W. R. (2008). An asymmetric solar wind termination shock. *Nature, 454*(7200), 71-74.

Strangeway, R. (1997). Comment on "The 100 Hz electric fields observed on Pioneer Venus Orbiter and a case against the whistler hypothesis for them" by KD Cole and WR Hoegy. *Journal of Geophysical Research: Space Physics, 102*(A10), 22279-22281.

Strangeway, R. (2000). Whistler-mode propagation in the collisional ionosphere of Venus. *Advances in Space Research, 26*(10), 1613-1618.

Stremler, F. G. (1990). *Introduction to communication systems* (3rd ed.). Reading, Mass.: Addison-Wesley Pub. Co.

Taylor, G. (1950). The formation of a blast wave by a very intense explosion: 2. The atomic explosion of 1945. *Proceedings of the Royal Society of London A: Mathematical, Physical and Engineering Sciences, 201*(1065), 175-186.

Tokar, R. L., Gurnett, D. A., & Feldman, W. C. (1984). Whistler mode turbulence generated by electron beams in Earth's bow shock. *Journal of Geophysical Research: Space Physics, 89*(A1), 105-114.

Torrence, C., & Compo, G. P. (1998). A practical guide to wavelet analysis. *Bulletin of the American Meteorological Society, 79*(1), 61-78.

Treumann, R. (2009). Fundamentals of collisionless shocks for astrophysical application: 1. Non-relativistic shocks. *The Astronomy and Astrophysics Review, 17*(4), 409-535.

Tzeferacos, P., Fatenejad, M., Flocke, N., Gregori, G., Lamb, D. Q., Lee, D., Meinecke, J., Scopatz, A., & Weide, K. (2012). FLASH magnetohydrodynamic simulations of shock-generated magnetic field experiments. *High Energy Density Physics, 8*(4), 322-328.

Van Compernolle, B., An, X., Bortnik, J., Thorne, R. M., Pribyl, P., & Gekelman, W. (2015). Excitation of chirping whistler waves in a laboratory plasma. *Physical Review Letters, 114*(24), 245002.

Zhong, L., Shu, N., Atsushi, F., Yukio, H., Satoshi, O., Mamiko, N., Akito, S., Michiaki, M., Toshiyuki, S., Yoshihisa, I., Akira, N., & Hiroyuki, D. (2005). Electron energy spectrometer for laser-driven energetic electron generation. *Japanese Journal of Applied Physics, 44*(9R), 6796.